The HI super profiles of the THINGS galaxies

Roger IANJAMASIMANANA

Department of Astronomy
University of Cape Town
South Africa

Supervised by: Prof. W.J.G. de Blok
University of Cape Town, South Africa

A dissertation submitted in partial fulfillment of the requirements for the degree of M.Sc.

in

the Department of Astronomy, as part of the

National Astrophysics and Space Science Programme

UNIVERSITY OF CAPE TOWN

November 2010

Abstract

We use the HI velocity profiles of The HI Nearby Galaxy Survey (THINGS) galaxies to study the phase structure of the interstellar medium (ISM) and its relation to galaxy properties and morphology. To construct high signal-to-noise (S/N) profiles, we use a method analogous to the stacking method sometimes used in high redshift HI observations. We call these high S/N profiles "super profiles". By decomposing the super profiles into Gaussian components, we find broad and narrow componentss in all our analyzed galaxies. Following earlier results from the literature, we identify the narrow and broad components to the Cold Neutral Medium (CNM) and Warm Neutral Medium (WNM) phases of the interstellar medium (ISM), respectively. We derive radial super profiles of some of the THINGS galaxies and we find some correlation between profile shapes and location within the galaxies. We observe a radial decline in velocity dispersions in most of our sample galaxies. Moreover, we find that the narrow component dominates inside the optical radius r_{25}. The super profiles also tend to be broader and more asymmetric inside r_{25}. We also analyze the shapes of the super profiles in different star formation regions within a galaxy. We find that the super profiles tend to be broader and more asymmetric in active star formation regions. We also find that the narrow component tends to dominate in high star formation rate regions.

Acknowledgements

First of all, I would like to thank the Almighty God for giving me the ability to finish this thesis. This thesis would not have been completed without his will.

I am grateful to my thesis advisor, Professor Erwin de Blok, for providing guidance and direction for the successful realization of this thesis.

I also acknowledge useful suggestions from Dr. Fabian Walter. Moreover, I would like to thank Dr. Leroy Adam for giving us the star formation rate maps of the THINGS galaxies. All other people who contributed to the realization of this thesis are also gratefully acknowledged.

I am also grateful to Elisa Josiane RINDRAHARISAONA for helping me with python programming. She was never too busy when I needed help from her.

My sincere gratitude goes to the South African SKA Project for funding this thesis.

Finally, my most affectionate gratitude goes to my family members, especially my parents for their moral support and prayer.

Plagiarism Statement

I know the meaning of plagiarism and declare that all of the work in the document, save for that which is properly acknowledged, is my own.

Contents

List of Figures

List of Tables

1

INTRODUCTION

Understanding galaxy evolution has long been one of the most prominent science goals in Astronomy. Studying the gas content of galaxies is a crucial step towards achieving this goal, as gas play an important role in the various processes that occur in galaxies. With the advance of new instrumentation and observing techniques, we have obtained a more detailed picture of the distribution and motion of gas in galaxies, yielding a wealth of valuable information about the physics of star formation, the phase structure of the interstellar medium (ISM) and its energy sources as well as the overall dynamics and chemistry of the ISM. In the future, the improved sensitivity and resolution of new upcoming radio telescopes such as the Karoo Array Telescope (MeerKAT), the Australian SKA Pathfinder (ASKAP), The Aperture tile in focus (Apertif) focal plane array, which is being developed for the Westerbork Synthesis Radio Telescope (WSRT) and eventually the Square Kilometer Array (SKA) will enable more detailed analysis of the properties of gas in different galaxy environments and their relation to e.g. star formation.

The general picture of our current understanding of star formation can be summarized as follows. Stars form as a result of gravitational contraction of gas clouds. When these clouds become dense enough and reach the so-called Jeans mass, the clouds become unstable (Palla and Zinnecker, 1999). Gas pressure can then no longer counteract the gravitational force and the clouds eventually collapse under their own weight. The collapsing clouds tend to fragment into high density gravitationally bound clouds which eventually give birth to stars with different masses. As collapse proceeds, gravitational

potential energy is released, thereby increasing the internal kinetic energy of the clouds and the corresponding internal pressure. When the internal temperature becomes high enough, nuclear fusion starts to occur in the core. The start of the nuclear reaction marks the birth of stars and the newly born stars start their evolution through the main sequence phase.

The above picture seems like a simple scenario. However, there are lots of complex physics involved in star formation which we do not understand yet. Some of the most fundamental unsolved problems in star formation include the influence of environment on the efficiency of a gas cloud to form stars, the link between gas properties and star formation, the formation of massive stars, the role of different feedback mechanisms in triggering, suppressing or regulating star formation, as well as the necessary and sufficient conditions for star formation to occur.

Many proposals have been made regarding the physics of star formation. These include that of Schmidt (1959) and Kennicutt (1989, 1998a), which relate the gas density to star formation rate (SFR) surface density via a power law to the form $\Sigma_{\rm SFR} \sim (\Sigma_{\rm gas})^{\rm n}$, where $\Sigma_{\rm SFR}$ is the SFR per unit area and $\Sigma_{\rm gas}$ represents the gas surface density. The Toomre Q parameter (Toomre 1964) is also another famous example which describes the ability of a thin gaseous disk to collapse under gravity. The Toomre Q parameter is defined as,

$$\mathrm{Q(r)} = \frac{\sigma\ \kappa}{\pi\ \mathrm{G}\ \Sigma_{\rm g}}, \tag{1.1}$$

where σ is the gas velocity dispersion, κ the epicyclic frequency, G the gravitational constant and Σ_g the gas surface density. The epicyclic frequency κ given by

$$\kappa^2 \ \equiv\ \frac{2\mathrm{V}^2}{\mathrm{R}^2}\left(1\ +\ \frac{\mathrm{R}}{\mathrm{V}}\frac{\mathrm{dV}}{\mathrm{dR}}\right), \tag{1.2}$$

is derived from the galaxy rotation curve V(R), with V the gas rotation velocity and R the distance from the galaxy center. The velocity dispersion σ can be derived by fitting a model to the observed emission line profile of the gas (e.g. Gaussian) and measuring the corresponding width. If Q is less than unity or Σ_g exceeds the critical surface density $\Sigma_{\rm critical}$ given by,

$$\Sigma_{\rm critical}\ =\ \alpha\frac{\sigma\ \kappa}{\pi\ \mathrm{G}}, \tag{1.3}$$

the gas is unstable against collapse and star formation will occur (van der Hulst et al. 1993, Martin and Kennicut 2001, Schaye 2004, de Blok and Walter 2006).

Studies of nearby galaxies are crucial to address the above problems. Nearby galaxies span a wide range in Hubble types and properties (metallicity, surface brightness, star formation rate) and can be observed at high resolution and sensitivity. For nearby galaxies, it is possible to study the distribution of atomic gas and molecular gas at a scale of a few hundred parsecs or less, which is the scale of giant molecular clouds. These observations thus provide us with valuable information about the properties of the emitting gas, the structure of the ISM and the energetic phenomena that shape the overall dynamics and structure of the ISM. Thus nearby galaxies provide a unique opportunity to address key science regarding star formation and the ISM.

1.1 The interstellar medium

1.1.1 General overview

The interstellar medium (ISM) is the place to study galaxy evolution as this is where stars are born. This medium is composed of gas, dust, relativistic particles and magnetic fields that undergo a variety of physical and chemical processes depending on the local conditions of the medium. The gas component can either be neutral, ionized or molecular, depending on its temperature and density. Most of this gas is in the form of atomic (HI) and molecular (H_2) hydrogen, which can be probed via their emission and absorption lines. For example, the 21 cm emission line, emitted when the spin of the proton and electron of hydrogen atoms pass from the state of being parallel to anti-parallel, has been extensively used as a probe of the neutral ISM. The diatomic hydrogen molecule H_2, however, has no permanent electric dipole moment and therefore, is difficult to detect. Instead, carbon monoxide (CO) has usually been used to trace the abundance of H_2 in the ISM (Leroy et al., 2009).

The dust component forms a small fraction of the total mass of the ISM ($\sim$1%). It was first recognized by its ability to absorb most of the light emit-

ted by nearby young stars (Trumpler, 1930). Dust can be a strong emitter of infrared emission. In fact, UV photons emitted by young stars are absorbed by dust grains and reradiated in the infrared regime. This infrared emission has been used as a tracer of current star forming regions in a galaxy. Dust is particularly important in terms of H_2 formation (Savage and Mathis, 1979; Mathis, 1990). Not only does it protect H_2 molecules from being dissociated by stellar FUV photons, but it also acts as a catalyst (by absorbing the photons released during radiative association of hydrogen atoms) and accelerate H_2 formation.

Relativistic particles are ubiquitous in the ISM. They can be observed in the gamma-ray regime as they produce gamma rays while colliding with interstellar matter. They also emit synchrotron radiation as they interact with the interstellar magnetic field. Moreover, they provide pressure support to the ISM and contribute to the energy budget of the ISM.

Finally, interstellar magnetic fields have been recognized by linear polarization of radio synchrotron emission, Zeeman splitting of neutral hydrogen 21 cm line and of radio molecular lines (Tielens, 2005). Interstellar magnetic fields provide pressure and energy support to the ISM. Understanding the interrelationship of these different components is crucial in terms of galaxy evolution as it seems to regulate the star formation activity of a galaxy.

1.1.2 The multi-phase ISM

As has already been mentioned earlier, the interstellar gas can be in the molecular, ionized or neutral form. These different forms are balanced by the various cooling and heating processes in the ISM. The different sources of cooling and heating of the ISM are reviewed by Tielens (2005). In summary, the cooling of the gas in the ISM is dominated by cooling through various emission lines such as [CII] 158 μm , [OI] 63 μm, Ly α. The cooling rate of these different cooling lines depends on the temperature of the gas. At lower temperatures ($\leq$ 1000K), the dominant coolant is [CII] cooling. Above 6000 K, cooling by [OI] line emission dominates and at higher temperature ($\geq 10^4$ K), the cooling is mostly dominated by Ly α. The very cold molecular gas results from the cooling by molecular rotational transitions.

Gas is also being heated up by several energy sources such as UV pho-

tons, the cosmic background radiation, magnetic fields, turbulence and cosmic rays. The most dominant heating mechanism is the photoelectric effect caused by FUV photons (6 eV< hν <13.6 eV) from young massive stars (Bakes & Tielens, 1994). In fact, stellar UV photons are absorbed by small dust grains and large Polycyclic Aromatic Hydrocarbon (PAHs) molecules. In the process, energetic electrons are created with excess energy. These electrons can either be absorbed by the grains as they lose their excess energy via collisions within the grains or, if energetic enough, can escape the grains with excess kinetic energy. This kinetic energy is then converted to heat and will heat up the gas. This process can lead to the formation of the so-called Warm Ionized Medium (WIM), a region of ionized gas of temperature $\sim 10^4$ K.

Heating and cooling can also be caused by processes such as shock waves, gravitational collapse, Supernova explosions (SNe). The latter are important in the formation of the very hot gas in the ISM which is known as the Hot Ionized Medium (HIM), with typical temperature of 10^6 K. SNe are also the main mechanisms that can drive the ISM away from its equilibrium. Thus, the global structure of the ISM is strongly affected by these various heating and cooling mechanisms and detecting the different phases of the ISM in different environments will help us understand more about the physics and chemistry of the ISM and their relation to star formation and galaxy evolution in general.

1.1.3 The two phases of the neutral ISM

Theoretical explanations regarding the existence of a two-phase medium

In this section, we summarize earlier theoretical work which predicts the existence of different phases in the ISM. We will show why we expect different phases to coexist in pressure equilibrium. We will, however, mostly focus on the two-phase model of the neutral ISM as this is more directly linked to the topic of this thesis.

The realization that the ISM may exist in different phases followed from the pioneering work of Spitzer (1956). He was the first to hypothesize the existence of hot coronal gas surrounding the Galactic disk while trying to ex-

plain the number of gas clouds at high galactic latitude observed by Münch (Münch, 1961) as well as the equilibrium of spiral arms in the presence of a strong magnetic field. Spitzer assumed a mean temperature of 10^6 K for this gas. The presence of such gas was later confirmed by space observations made by the Copernicus satellite which first detected the O VI absorption line at 1031.92 Å and 1037.61 Å (Rogerson et al. 1973; Jenkins 1978a, 1978b; York 1977). Later theoretical work regarding the phase structure of the ISM followed from Spitzer's idea. In 1969, Field, Goldsmith and Habing (hereafter FGH) first developed the two-phase model of the ISM. Their model consists of two thermally stable gas phases; cool (T $\sim$ 100 K) dense clouds, which they labelled as phase H, are embedded in a warm (T $\sim 10^4$ K) diffuse intercloud medium (labelled as phase F). They also introduced a third phase G (T $\sim 5 \times 10^8$ K) which is thermally unstable. The three phases can coexist in pressure equilibrium. FGH demonstrated why we expect to see two thermally stable phases to coexist in pressure equilibrium. The principles behind this idea are illustrated in Tielens (2005) and are repeated here in a slightly more developed way for clarity.

For a gas of density ρ, temperature T, pressure P, cooling rate Λ and heating rate Γ, the generalized loss function, $\mathcal{L}$, which describes the thermal balance between cooling and heating, can be written as (Tielens 2005),

$$\mathcal{L}(\rho, \mathrm{T}) = \rho^2 \Lambda - \rho \Gamma \tag{1.4}$$

if we ignore non-thermal pressure sources such as magnetic fields. Thermal equilibrium is reached when $\mathcal{L}$=0. Cooling dominates if $\mathcal{L} > 0$ whereas heating will take over if $\mathcal{L} < 0$. We will now describe the thermal stability criterion for isobaric (pressure constant) perturbation. The condition for thermal instability is given by,

$$\left(\frac{\delta \mathcal{L}}{\delta \mathrm{T}}\right)_{\mathrm{P}} < 0. \tag{1.5}$$

If P is constant while ρ and T are perturbed ($\rho = \rho_o + \delta\rho$; $\mathrm{T} = \mathrm{T_o} + \delta\mathrm{T}$) then,

$$(\delta \mathcal{L})_{\mathrm{P}} = \left(\frac{\delta \mathcal{L}}{\delta \mathrm{T}}\right)_{\rho} \delta \mathrm{T} + \left(\frac{\delta \mathcal{L}}{\delta \rho}\right)_{\mathrm{T}} \delta \rho \tag{1.6}$$

$$\left(\frac{\delta \mathcal{L}}{\delta \mathrm{T}}\right)_{\mathrm{P}} = \left(\frac{\delta \mathcal{L}}{\delta \mathrm{T}}\right)_{\rho} + \left(\frac{\delta \rho}{\delta \mathrm{T}}\right)_{\mathrm{P}} \left(\frac{\delta \mathcal{L}}{\delta \rho}\right)_{\mathrm{T}} \tag{1.7}$$

For $\mathrm{P} = \rho\mathrm{T} = \text{constant} \Rightarrow \delta\ \mathrm{P} = 0$, therefore,

$$\rho\delta\mathrm{T} + \mathrm{T}\delta\rho = 0 \tag{1.8}$$

$$\left(\frac{\delta\rho}{\delta\mathrm{T}}\right)_{\mathrm{P}} = -\frac{\rho}{\mathrm{T}} \tag{1.9}$$

$$= -\frac{\rho_o}{\mathrm{T_o}} \tag{1.10}$$

where ρ_o and $\mathrm{T_o}$ are the density and temperature at equilibrium. Equation (1.7) then becomes,

$$\left(\frac{\delta\mathcal{L}}{\delta\mathrm{T}}\right)_{\mathrm{P}} = \left(\frac{\delta\mathcal{L}}{\delta\mathrm{T}}\right)_{\rho} - \frac{\rho_o}{\mathrm{T_o}}\left(\frac{\delta\mathcal{L}}{\delta\rho}\right)_{\mathrm{T}} \tag{1.11}$$

The condition for thermal instability is thus given by,

$$\left(\frac{\delta\mathcal{L}}{\delta\mathrm{T}}\right)_{\mathrm{P}} = \left(\frac{\delta\mathcal{L}}{\delta\mathrm{T}}\right)_{\rho} - \frac{\rho_o}{\mathrm{T_o}}\left(\frac{\delta\mathcal{L}}{\delta\rho}\right)_{\mathrm{T}} < 0 \tag{1.12}$$

In the FGH model, the heating is from low energy cosmic rays and the cooling is by collisions. In this case, the loss function is given by

$$\mathcal{L}(\rho, \mathrm{T}) = \rho^2\Lambda(\mathrm{T}) - \rho_{\mathrm{H}}\zeta_{\mathrm{CR}} \tag{1.13}$$

where ζ_{CR} is the cosmic ray ionization rate. Since ζ_{CR} is constant, therefore,

$$\left(\frac{\delta\mathcal{L}}{\delta\mathrm{T}}\right)_{\rho} = \rho^2\frac{\mathrm{d}\Lambda}{\mathrm{dT}} \tag{1.14}$$

$$\left(\frac{\delta\mathcal{L}}{\delta\rho}\right)_{\mathrm{T}} \equiv \rho\Lambda \tag{1.15}$$

Substituting those values into Equation (1.12), we have,

$$\rho^2\frac{\mathrm{d}\Lambda}{\mathrm{dT}} - \frac{\rho^2}{\mathrm{T}}\Lambda < 0 \tag{1.16}$$

$$\frac{\mathrm{d}\Lambda}{\mathrm{dT}} - \frac{\Lambda}{\mathrm{T}} < 0 \tag{1.17}$$

If we multiply both sides of Equation (1.17) by $\dfrac{\mathrm{dT}}{\Lambda}$ then it becomes,

$$\frac{\mathrm{d}\Lambda}{\Lambda} - \frac{\mathrm{dT}}{\mathrm{T}} < 0 \tag{1.18}$$

Integrating both sides of Equation (1.18) gives us

$$\ln\Lambda - \ln T < \text{constant}. \tag{1.19}$$

At equilibrium, $\Lambda_o - T_o$ = constant. So by substituting the value of the constant into Equation (1.19), we have,

$$\ln\Lambda - \ln\Lambda_o - \ln T + \ln T_o < 0 \tag{1.20}$$

By differentiating both sides of Equation (1.20) we get,

$$d\ln\Lambda - d\ln T < 0 \tag{1.21}$$

If we divide both sides of Equation (1.21) by dlnT, the equation for thermal instability can be expressed as,

$$\frac{d\ln\Lambda}{d\ln T} < 1 \tag{1.22}$$

The plot of log (Λ/T) = log(Γ/P) versus log(T) is shown in Figure 1.1 for pressure equilibrium and constant heating. As Figure 1.1 shows, there are four points of intersection between the equilibrium curve $\mathcal{L} = 0$ and the line of constant (Γ/P). This indicates that different phases can coexist in pressure equilibrium. Any points below the curve are dominated by cooling whereas those above the curve are dominated by heating. There are two points labelled "Clouds" and "Intercloud" in Figure 1.1. These represent thermally stable phases since $\left(\frac{\delta\mathcal{L}}{\delta T}\right)_P > 0$ in these points. These represent the CNM and the WNM phases of the ISM. The other two points of intersection in Figure 1.1 are thermally unstable since $\left(\frac{\delta\mathcal{L}}{\delta T}\right)_P < 0$ in these points. FGH described these phases as "transient phenomenon in nature" since their existence cannot be sustained long due to their thermal instability characteristics.

The FGH model successfully explained the existence of different phases of the ISM, however, later work showed the model to be incomplete (Dickey and Brinks 1993). The FGH model considered low energy cosmic ray flux as the source of heating, but did not include other important sources of heating such as photoelectric heating from small dust grains or large PAH molecules, UV and X-ray flux (Silk and Werner 1969; Watson 1972; Draine

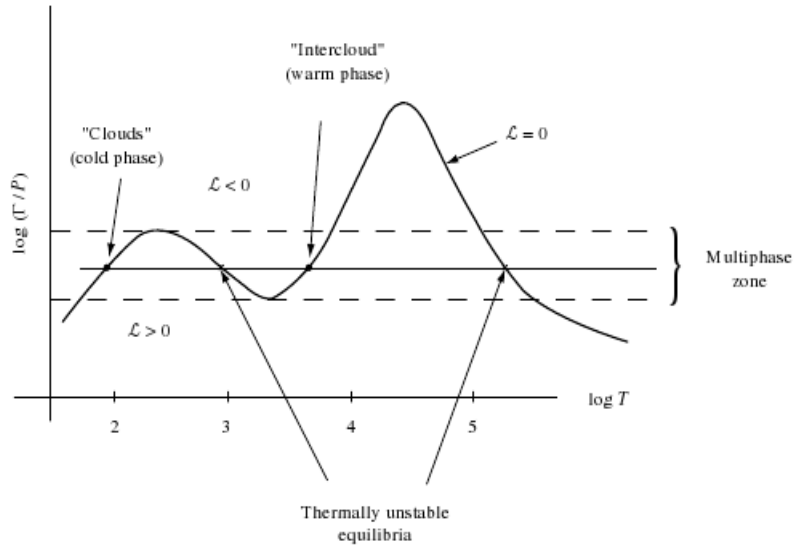

Figure 1.1: Figure taken from Tielens 2005 which illustrates the existence of multiple-phase in ISM and shows why we expect to see multiple phases to coexist in pressure equilibrium. The horizontal solid line is a line of constant pressure. The solid curve represents the thermal equilibrium curve $\mathcal{L} = 0$. Any points above this curve would be dominated by heating; whereas those below the curve would be dominated by cooling. There are four points of intersection between the line of constant pressure and the curve. Two of them are thermally stable whereas the others are thermally unstable.

1978; Weingartner and Draine 2001; Wolfire et al. 2003), Supernovae explosions (McKee and Ostriker, 1977; Spitzer, 1982) or Galactic differential rotation (Sellwood and Balbus, 1999). Moreover, the model did not include non-thermal pressure sources such as magnetic fields. A more modern treatment of the two-phase model is given by Wolfire et al. (2003).

Although much theoretical work has been done regarding the phase structure of the ISM, the model parameter values are still uncertain (Wolfire et al. 2003). This reflects the need of more observations to understand the properties of the gas itself to constrain model parameter values. The next section summarizes earlier observational evidence of the two phase medium (CNM/WNM).

Observational evidence

Here we summarize earlier observational evidence in support of the two-phase model mentioned above and some of the observed properties of the

two phases and their relation to star formation.

Observational evidence of the two phases of the neutral ISM comes from comparison of HI line emission and absorption. Early observations of HI emission and absorption lines showed that the former is always broader than the latter. Clark (1965) tried to explain this feature and suggested that this difference could be attributed to a temperature difference between two components of atomic hydrogen. He made a suggestion that the HI absorption could arise from a cold gas component with temperature around 100 K whereas the emission line might come from a component of warm gas with temperature as high as 10^4 K. Evidence in support of this idea came later from interferometric observations of HI emission and absorption lines (Radhakrishnan et al. 1972). The main argument from Radhakrishnan et al (1972) in support of the existence of a two-component model is that if the clouds responsible for the emission and absorption line were at the same temperature then we would expect them to have roughly the same width, since turbulence, if important, must broaden them at the same level. Radhakrishnan et al (1972) measured the spin temperature (the excitation temperature of the 21 cm hyperfine transition of hydrogen atoms, see, e.g., Purcell and Field , 1956; Field, 1959) of the two components. They found a spin temperature ranging from 20 to 200 K with a mean of 80 K for the absorbing gas and a lower limit of 150 to 750 K for the emitting gas. These two components are know widely known as the Cold Neutral Medium (CNM) and the Warm Neutral Medium components (WNM) of the ISM.

A more recent identification of the CNM and WNM was made by Braun (1997) in a sample of 11 nearby spiral galaxies. Braun (1997) analyzed the HI emission in these galaxies and found what he called a high brightness filamentary network (HBN) of HI emission which he associated with the CNM phase of the ISM and a diffuse low brightness emission which he identified with the WNM. The HBN dominates inside the optical radius r_{25} which accounts for 60-90 % of the total HI emission within r_{25} and then decreases abruptly at the edge of the optical disk where the diffuse component takes over. The narrow line width of the HBN allowed Braun (1997) to give a strong upper limit to the HBN temperature to be 300 K.

Other observational studies of the CNM and the WNM was made by Young and Lo (1996, 1997) and Young et al (2003) who analyzed the HI

velocity profiles of a sample of seven nearby dwarf galaxies. By fitting the HI velocity profiles in these galaxies with Gaussian components, they found a broad component with dispersion ranging from about 8 to 13 km s^{-1} and a much narrower component with a dispersion 3-5 km s^{-1}. They also found that the narrow component tends to be located at a higher column density and near star forming regions, whereas the broad component tends to be present in every line of sight. They associated these two components with the CNM and WNM phases of the ISM.

Similar studies were also made by de Blok and Walter (2006) for NGC 6822, a dwarf galaxy belonging to the Local Group. By decomposing the HI profiles of this galaxy into Gaussian components, they also found broad and narrow componentss with mean velocity dispersion $\sim$ 8 km s^{-1} and 4 km s^{-1}, respectively. de Blok and Walter (2006) also found that the narrow component tends to be located near star forming regions, whereas the broad component shows an ubiquitous distribution.

These kinds of studies are worth expanding to larger samples to see how the HI profiles are related to different properties of galaxies. Studies by Young and Lo (1996, 1997) and Young et al (2003), in a sample of seven dwarf galaxies, already showed that we do not expect to see the properties of the broad and narrow componentss, mentioned earlier, to be the same for different ISM environments. For example, unlike the other dwarf galaxies studied, they found no narrow component in LGS 3 even in high column density regions. They suggested that this lack of cool component in LGS 3 may be the reason for its low star formation rate. However, these conclusions were drawn from studies of a relatively small sample of galaxies, so more studies are needed to investigate how the CNM/WNM properties vary in different ISM environments. This requires studies of a significant sample of galaxies that covers a wide range in physical properties and morphology. This may give important clues towards understanding the relation between gas content of galaxies and their star formation potential.

Theoretical application of the two-phase ISM study

The identification of the CNM and WNM phases is important to constrain theoretical models regarding the phase structure of the ISM and its relation to star formation activity of a galaxy. This was emphasized by de

Blok and Walter (2006) in a paper on the star formation threshold in NGC 6822. By decomposing the line profiles of this galaxy into Gaussian components, they showed that among various star formation threshold models, the use of the velocity dispersion derived from the narrow component in the Toomre Q-criterion best predicts the location favorable for star formation in NGC 6822. They emphasized that, in a star forming multi-phase medium, the use of a velocity dispersion derived from a second-moment map (or intensity weighted velocity dispersion, see, e.g., Walter et al. 2008) may suffer from overestimates due to the non-Gaussianity (multi-component, double-peaked or asymmetric profiles) of the line profiles and therefore, not relevant for a star formation threshold analysis. The importance of CNM and WNM was also discussed by Wolfire et al (2003). They reported that the thermal pressure of HI can be reasonably determined if the galaxy ISM has two components (the CNM and WNM). Based on the assumption that the two phases are in equilibrium state, and from knowing the gas phase abundances, dust properties and intensity of the radiation field, they were able to estimate the range of pressure, as a function of radius (R$\leq$ 18 kpc), over which the two phases can coexist. They also estimated the average thermal pressure of HI in the Galaxy up to R $\simeq$ 18 kpc. Thus, if we can detect these CNM and WNM and if we happen to find that they (most likely the CNM) are associated with star formation, we can use their observed parameters such as velocity dispersion to constrain star formation laws. This study is particularly important for dwarf galaxies since it is often difficult to detect CO in these objects due to their low metal abundance. Therefore, if the CNM and WNM are linked to star formation, their properties can be useful alternatives to molecular gas properties to study the conditions for star formation in dwarf galaxies.

1.2 THINGS

The HI Nearby Galaxy Survey (THINGS; Walter et al. 2008) is a survey of 34 nearby dwarf and spiral galaxies observed with the Very Large Array (VLA) of the National Radio Observatory (NRAO) in the USA. The purpose of THINGS was to obtain high quality (high spectral and spatial resolution) maps of the neutral hydrogen distribution of these galaxies. The THINGS galaxies have distances between 2 Mpc and 15 Mpc, star formation rates of $\sim 10^{-3}$ to ~ 6 $M_\odot$ yr^{-1}, absolute luminosities of -11.5 to -21.7, total HI

masses of (0.01 to 14) $\times$ 10^9 $M_\odot$, and metallicities of 7.5 to 9.2 in units of [12+log(O/H)]. The THINGS galaxies thus span a wide range in physical properties and morphology, from low mass, metal poor galaxies to massive spiral galaxies. THINGS however did not include early type (E/SO) galaxies. THINGS also excluded edge-on systems to avoid projection effects. Moreover, to avoid the effect of missing short spacings and mosaicing, Local Group galaxies were also excluded from the THINGS sample. Using the VLA B, C and D arrays, the THINGS targets were observed at a spectral and spatial resolution of $\lesssim$ 5.2 km s^{-1} and $\sim 6''$, respectively. THINGS was primarily aimed at obtaining high resolution maps of the HI of a significantly large sample of galaxies in order to study the dark matter distribution, kinematics and processes leading to star formation. Most of the 34 galaxies had already been observed by the Spitzer Infrared Nearby Galaxies Survey (SINGS; Kennicut et al. 2003) and the Galaxy Evolution Explorer Nearby Galaxies Survey (GALEX NGS; Gil de Paz et al. 2007) thus enabling multiwavelength studies of these objects. The resolution of THINGS is well matched to that of the SINGS survey ($6''$ at 24μm). The THINGS data, which include data cubes and moment maps are available at `http://www.mpia.de/THINGS/Data.html`.

1.3 Aims of this thesis

The identification of the multi-phase ISM (e.g. Dickey and Brinks, 1993) has greatly contributed to our knowledge of the phase structure of the ISM. However, the lack of high resolution HI observations in a substantial sample of galaxies limits our knowledge on the properties of these two components. High resolution studies of the neutral atomic ISM in a large sample of galaxies will help us to better understand how the properties of these two components vary from galaxy to galaxy and how they relate to star formation activity of galaxies. The completion of THINGS enables us to study, at much higher resolution, the HI profiles of a significant sample of galaxies. This may give important clues towards understanding, e.g., the presence of different phases of the ISM and its influence on the properties of galaxies, the relation between gas content of galaxies and star formation and the different mechanisms that may regulate the star formation activity of a galaxy. This project will therefore focus on the study of the shapes of the THINGS HI profiles and relate these shapes to e.g., the phases of the interstellar medium, star formation activity and morphology of galaxies. We study all 34 sample galaxies to

investigate how different environments affect the shapes of the profiles and how these shapes tell us about the phase structure of the ISM and the star formation activity of galaxies.

1.4 Data

We use data (moment maps and data cubes) from THINGS to study the ISM properties of nearby dwarf and spiral galaxies and possible correlations to star formation. In addition, we use calibrated star formation rate (SFR) surface density, $\Sigma_{\rm SFR}$, maps derived by Leroy et al (2008) to identify different star formation regions in the THINGS sample. These maps were constructed by combining the GALEX FUV and the SINGS 24μm maps. FUV radiation is mainly from O and B type stars and probes unobscured star formation ($<$ 100 Myr). Radiation at 24μm is mainly from small dust grains following absorption of UV photons from nearby stars and probes recent star formation ($\sim$10 Myr). The combination of these two maps thus traces both obscured and unobscured star formation. Using FUV-to-SFR calibration by Salim et al. (2007) and following Calzetti et al. (2007), Leroy and collaborators derived the following linear combination of FUV and 24μm intensity to estimate $\Sigma_{\rm SFR}$,

$$\Sigma_{\rm SFR} \; = \; (8.1 \; \times \; 10^{-2} \; {\rm I_{FUV}} \; + \; 3.2^{+1.2}_{-0.7} \; \times \; 10^{-3} \; {\rm I_{24}}) \; \cos {\rm i}$$

where $\Sigma_{\rm SFR}$ is in units of $M_\odot$ kpc^{-2} yr^{-1}. The intensity of the FUV ($I_{\rm FUV}$) and 24μm (I_{24}) are in units of MJy ster^{-1}. The cos i term is to account for the effect of inclination. The resolution adopted by Leroy et al. (2008) for the $\Sigma_{\rm SFR}$ maps ($\sim 5''$) is well-matched to that of the THINGS HI data.

1.5 Outline of the current thesis

In Chapter 2, we describe the principles of our method for obtaining high signal-to-noise (S/N) profiles. Section 2.2 describes the decomposition of the profiles. In Chapter 3 we discuss various possible systematic effects that may affect the shapes of the profiles. We also make subsamples based on the shapes of the profiles and define our clean sample. In Chapter 4, we check the reliability of the shapes of the profiles of the clean sample. Chapter 5 deals with possible correlations between the shapes of the profiles and properties of

galaxies. We discuss our results in Chapter 6. Summary and future prospects are given in Chapter 7.

2

THE THINGS SUPER PROFILES

2.1 A brief introduction on HI data cubes and velocity profiles

Atomic neutral hydrogen (HI) can be observed through its 21-cm hyperfine line emission. When observing this gas, it is common practice to view the data in a three dimensional data cube having two spatial axes (right ascension, declination) and one velocity or frequency axis. A one-dimensional slice along the velocity axis at a particular right ascension (RA) and declination (DEC) is called *a spectral line profile* or *velocity profile*. A velocity profile thus carries information about the velocity distribution of the gas at one position. In this thesis, we are particularly interested in measuring the width of this profile, which gives us an estimate of the velocity dispersion or the random motions of the HI gas. We adopt the standard THINGS pixel size.

2.2 Constructing high S/N profiles

Individual HI velocity profiles in typical HI observations generally have a medium ($\simeq$10) to low ($\simeq$5) Signal-to-Noise ratio (S/N). In the THINGS observations, fitting all individual profiles in a data cube separately can lead to inaccurate results due to the noise. Therefore, to construct high S/N profiles, we use a method analogous to the *stacking* method sometimes used in high-redshift HI observations. This is done by summing each individual

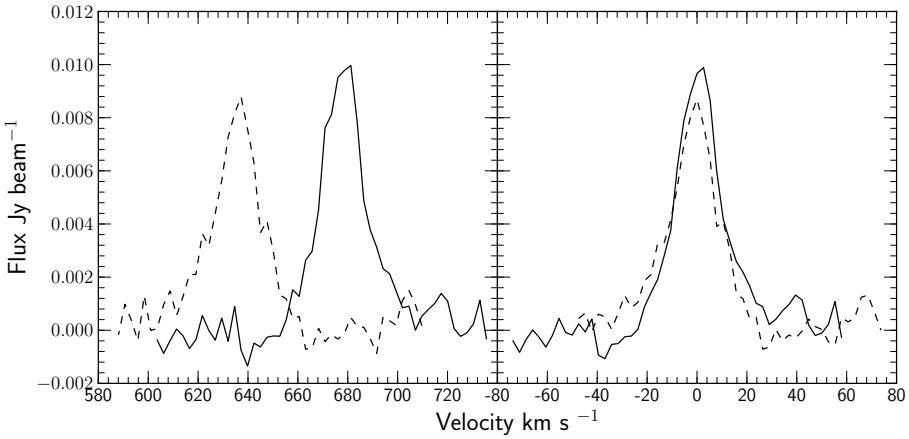

Figure 2.1: Examples of individual line profiles, extracted at different positions in a galaxy, before (right panel) and after (left panel) shifting. Note the difference in velocity of the two example profiles before the shifting. After the shifting, the profiles are aligned at the same reference velocity.

profile in a data cube after shifting them to a common central velocity. This is done by removing the line of sight component of the rotation velocity of the peak of the profile. To illustrate the method, Figure 2.1 (*upper panel*) shows examples of individual HI velocity profiles extracted at different positions from the natural-weighted data cube of NGC 628. One can see that different profiles have different velocities. Therefore, the profiles cannot be summed as they are, but need to be shifted in velocity to the same reference velocity.

We use the task SHUFFLE in the Groningen Image Processing System (GIPSY) to shift the individual profiles in a data cube to a common reference velocity. SHUFFLE uses a velocity field to define the amount by which a profile in the corresponding data cube needs to be shifted in order to end up at the same reference velocity. The output from SHUFFLE is a data cube that contains individual profiles aligned at a common central velocity.

When applying this method, we only use profiles whose peak flux exceeds the 3σ rms noise level in the data cubes. We have used Gauss Hermite h_3 polynomials velocity fields to construct the *shuffled* data cubes. The advantages of using such velocity fields are described by de Blok et al. (2008). We sum several different subsets of the shuffled profiles (as defined by e.g.

location within the galaxies) to produce what we call *super profiles*. These are high S/N profiles, which due to their increased S/N allow us to more reliably explore the presence of the cold and warm neutral components of the ISM.

We show in Figure 2.2 the super profiles of each THINGS galaxy, which are typically a sum of thousands of individual spectra (see Table 2.1). The error bars (as defined in Section 2.3) are smaller than the size of the symbols and are not visible in the plots. The super profiles are generally characterized by broader wings and narrower peaks than a pure Gaussian profile. Moreover, most of the super profiles are quite symmetrical except for a few galaxies. These features are similar to what was found for the individual profiles of seven nearby dwarf galaxies studied by Young and Lo (1996, 1997) and Young et al. (2003) but here the profiles are seen at much higher S/N. The negative wings in some super profiles (NGC 5457 and NGC 2403) are artifacts of observations, caused by missing low spacings and deconvolution.

2.3 Profile fitting and decomposition

Here we analyze the super profiles derived from summing all profiles, whose peak flux exceeds the 3 σ rms noise level, of each galaxy in the THINGS sample. Following de Blok and Walter (2006), we fit the super profiles of the THINGS galaxies both with one Gaussian and two Gaussian components using the GIPSY task XGAUPROF. All parameters (dispersion, mean, area, amplitude, constant background term) in both kinds of fits are left free. The linear and quadratic background terms are fixed to zero value. The uncertainties in the data points of each super profiles are defined as follows. In each individual profile, data points have an uncertainty equal to the noise in the profile. If we then create super profiles, that is if at a certain velocity V we combine N profiles, then the noise in the profile must be multiplied by $\sqrt{\mathrm{N}}$ if we define the super profiles by adding, which is the case here. The uncertainty in each velocity point of the super profiles is then defined as the noise level in one channel map multiplied by the square root of the number of stacked profiles at the corresponding velocity. The inverse of the square of these uncertainties are then used as the weighting factors in our double and single Gaussian fitting. Note that we correct for the presence of a neg-

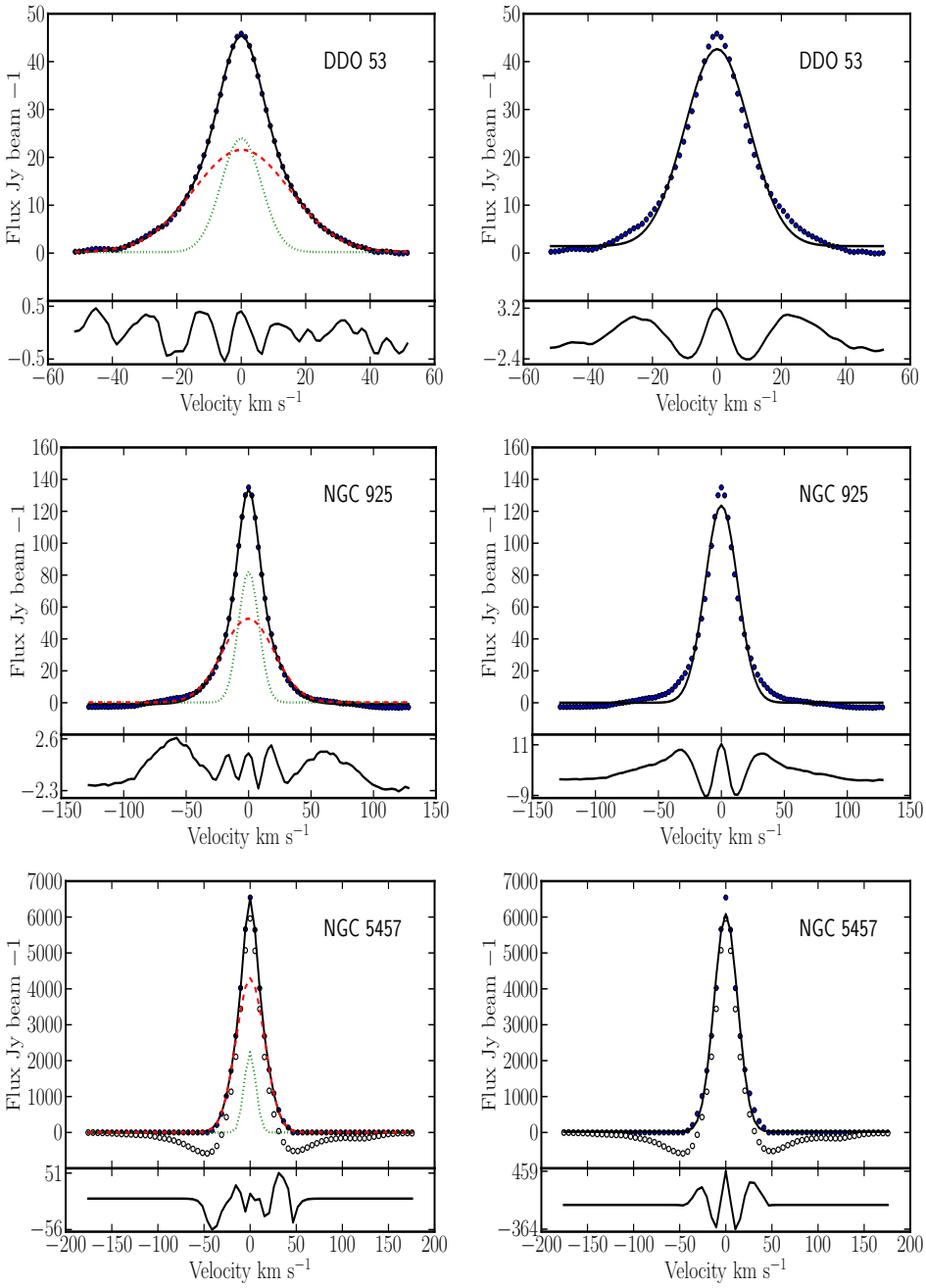

Figure 2.2: Examples of super profiles for the THINGS galaxies. The left panels show super profiles fitted with double Gaussian components whereas the right panels show super profiles fitted with a single Gaussian component. The bottom panels show the residuals from the fits. The filled circles indicate the data points. The solid black lines represent the results from the single and double Gaussian fitting. The dashed and the dotted lines represent the narrow and broad components required in the double Gaussian fitting. Note the negative wings in the super profile of NGC 5457 caused by missing low spacings and deconvolution. We correct for the presence of this negative bowl by fitting and removing a baseline prior to Gaussian fitting. For this galaxy, the open circles represent the data before the correction and the filled circles represent the data after the correction. The errors on the data points are smaller than the size of the symbols.

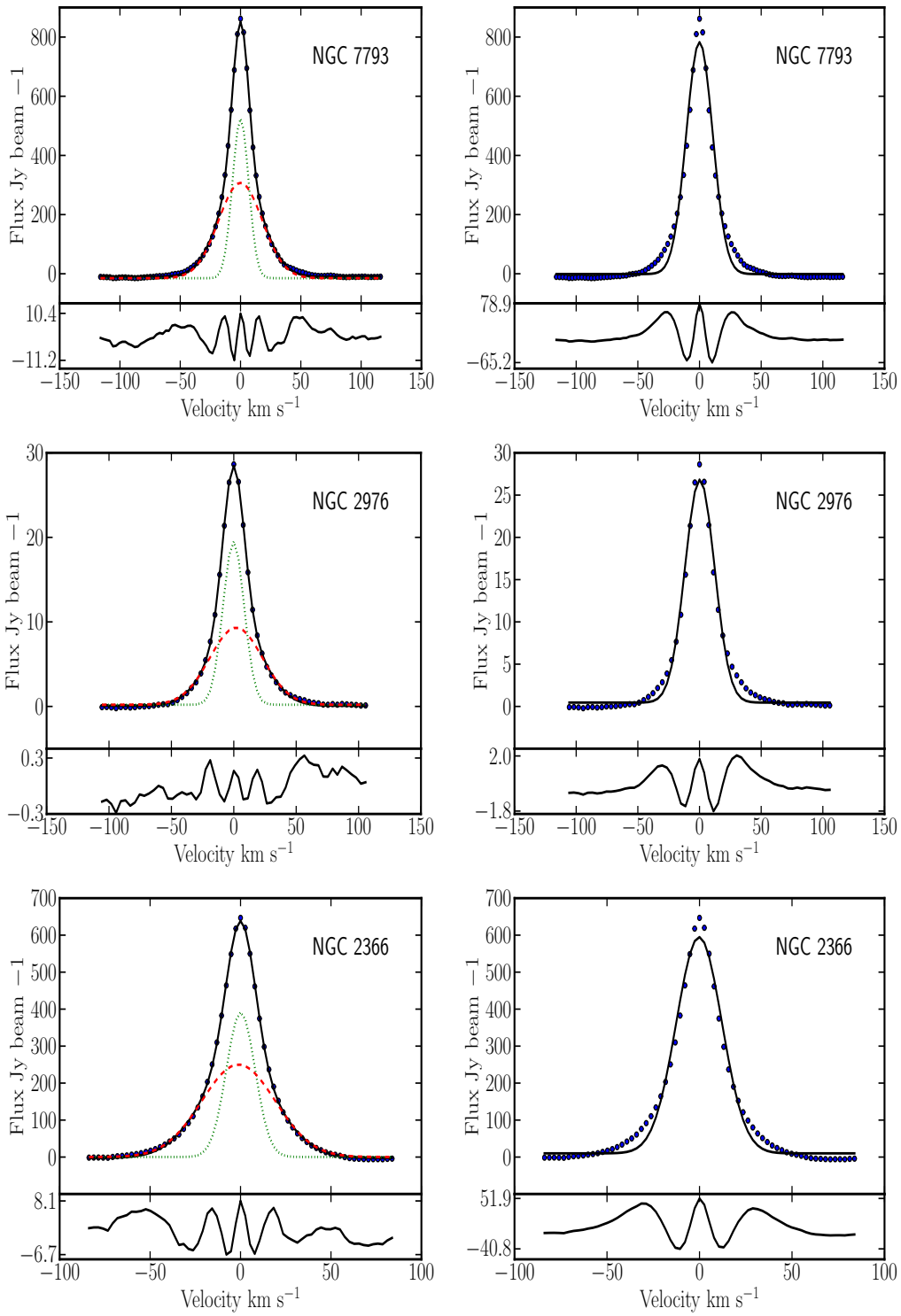

Figure 2.2 (Continued)

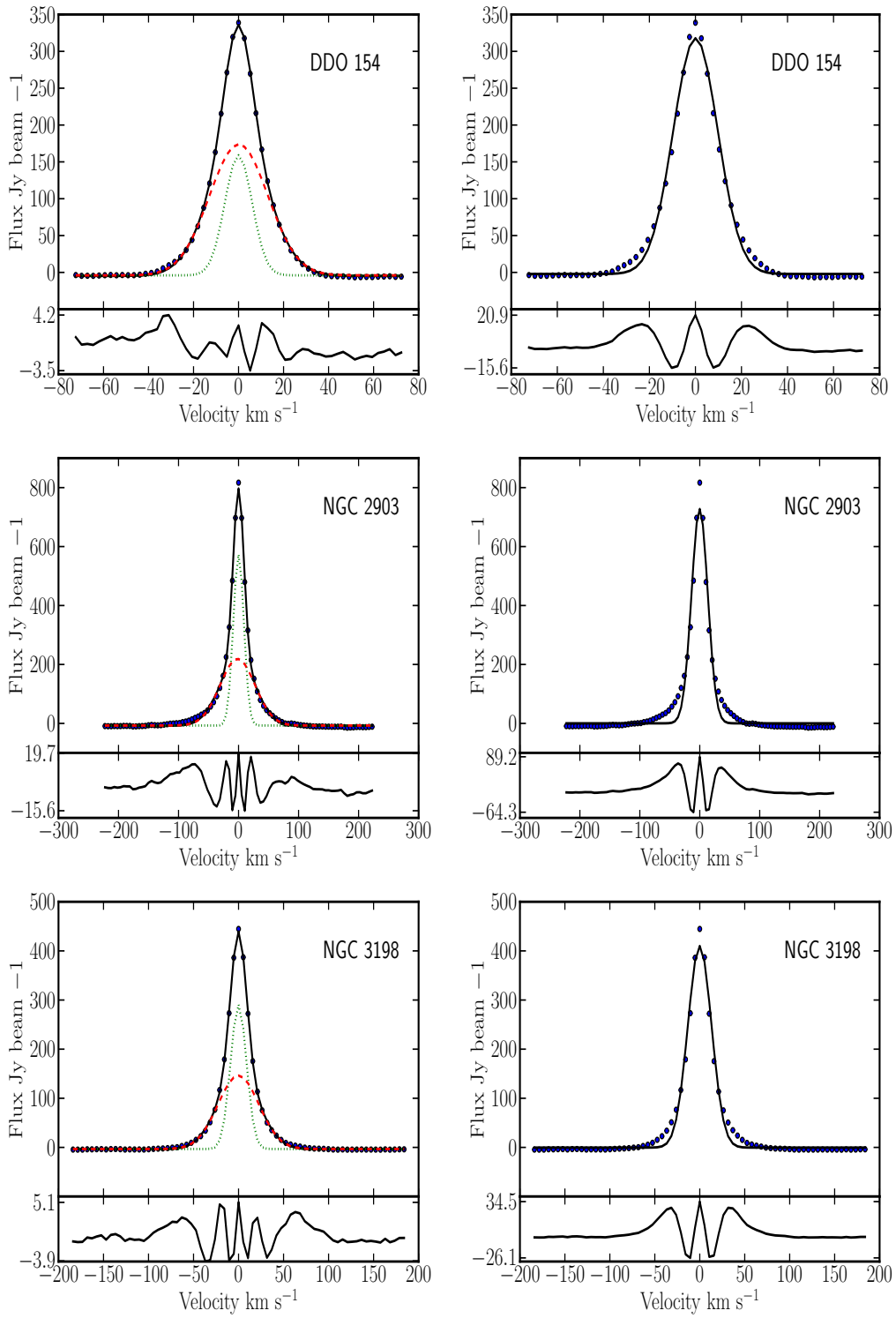

Figure 2.2 (Continued)

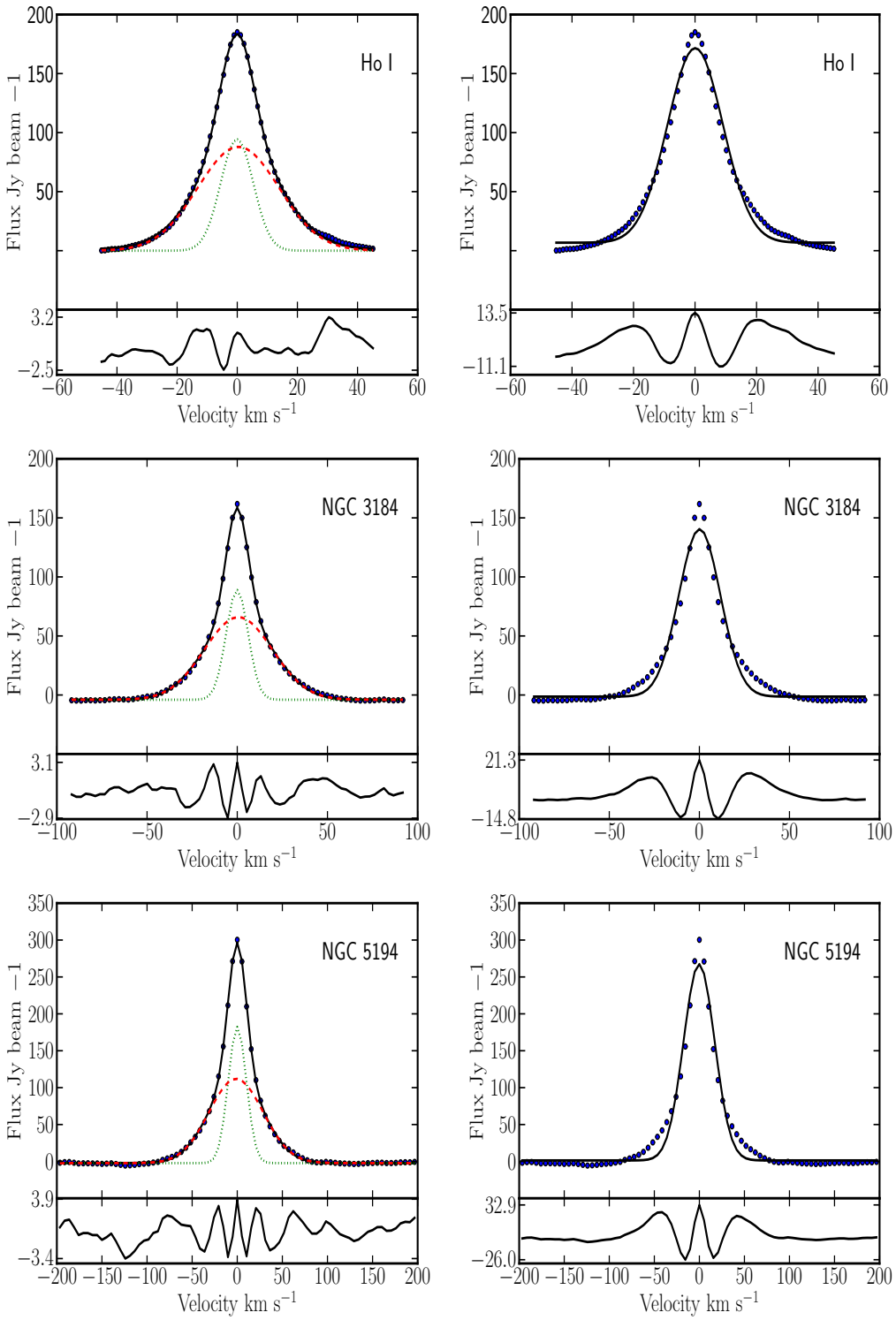

Figure 2.2 (Continued)

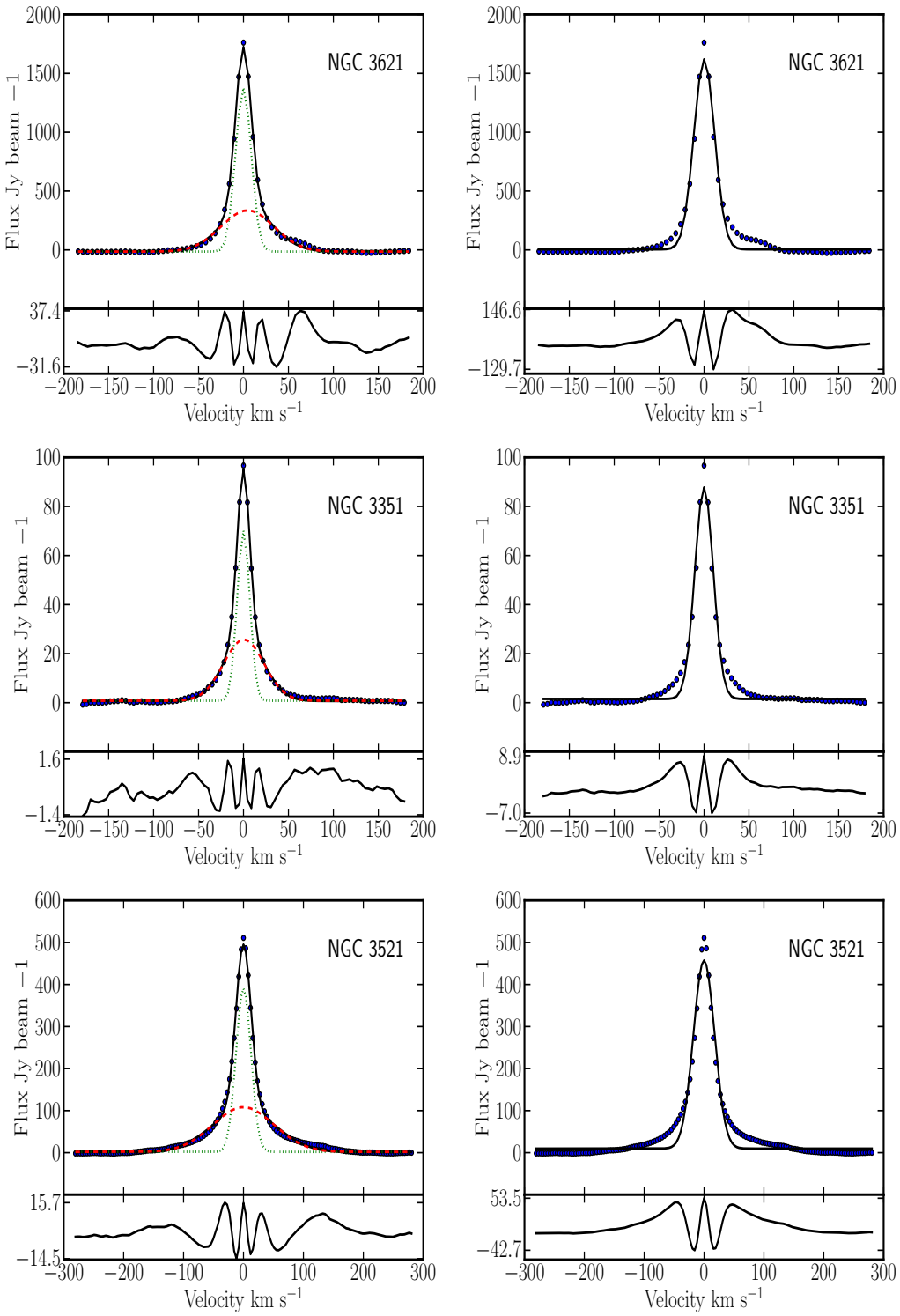

Figure 2.2 (Continued)

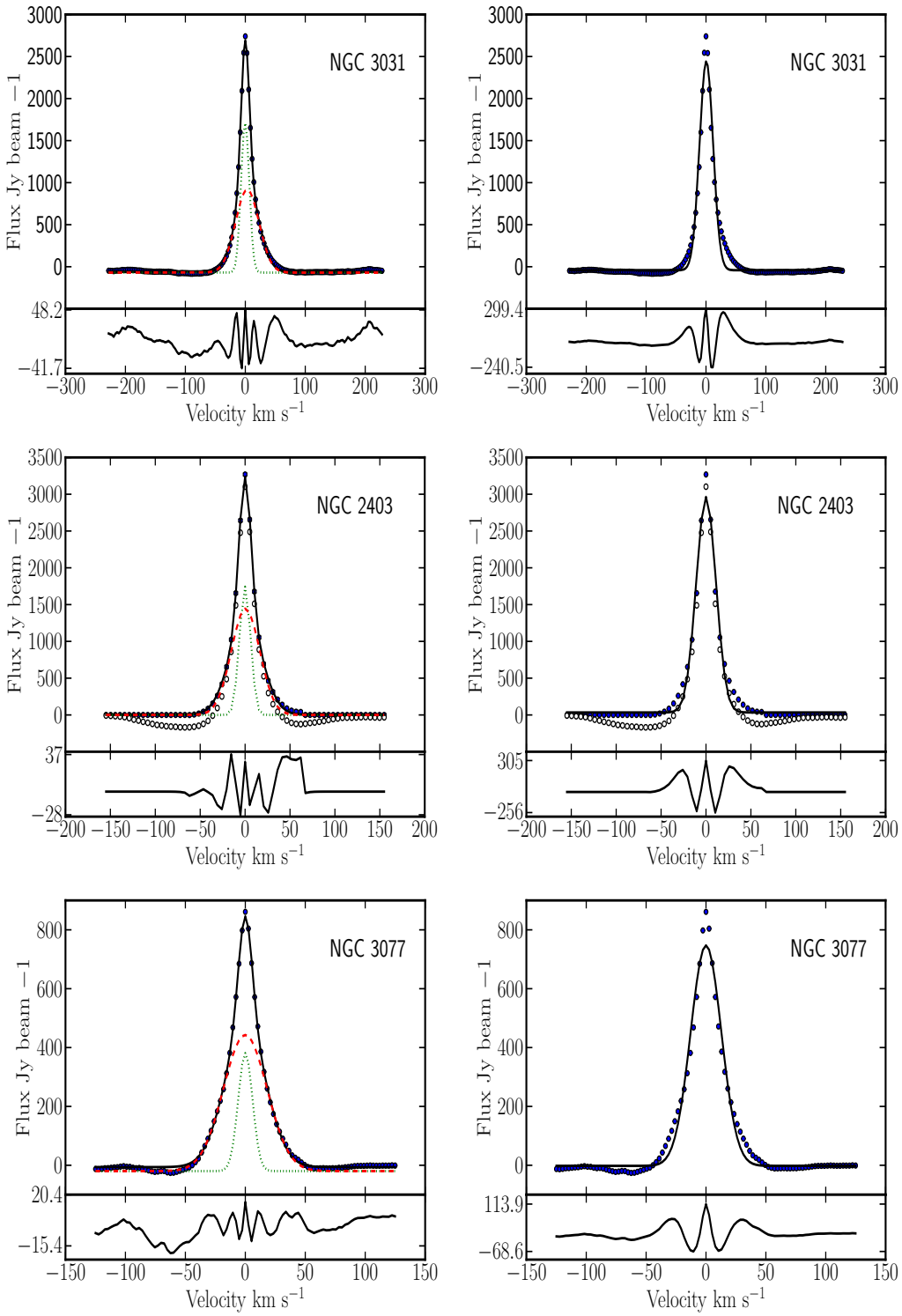

Figure 2.2 (Continued)

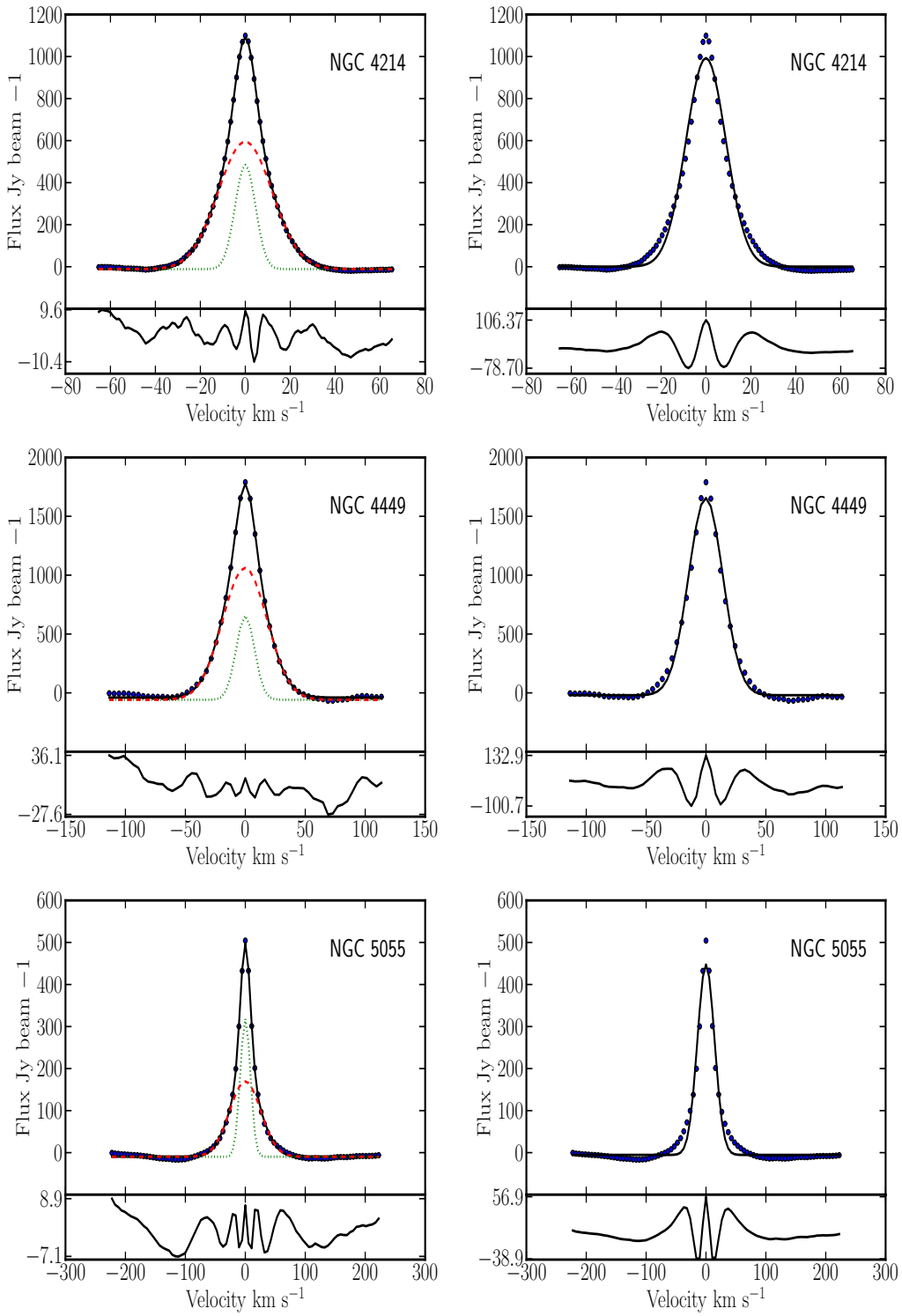

Figure 2.2 (Continued)

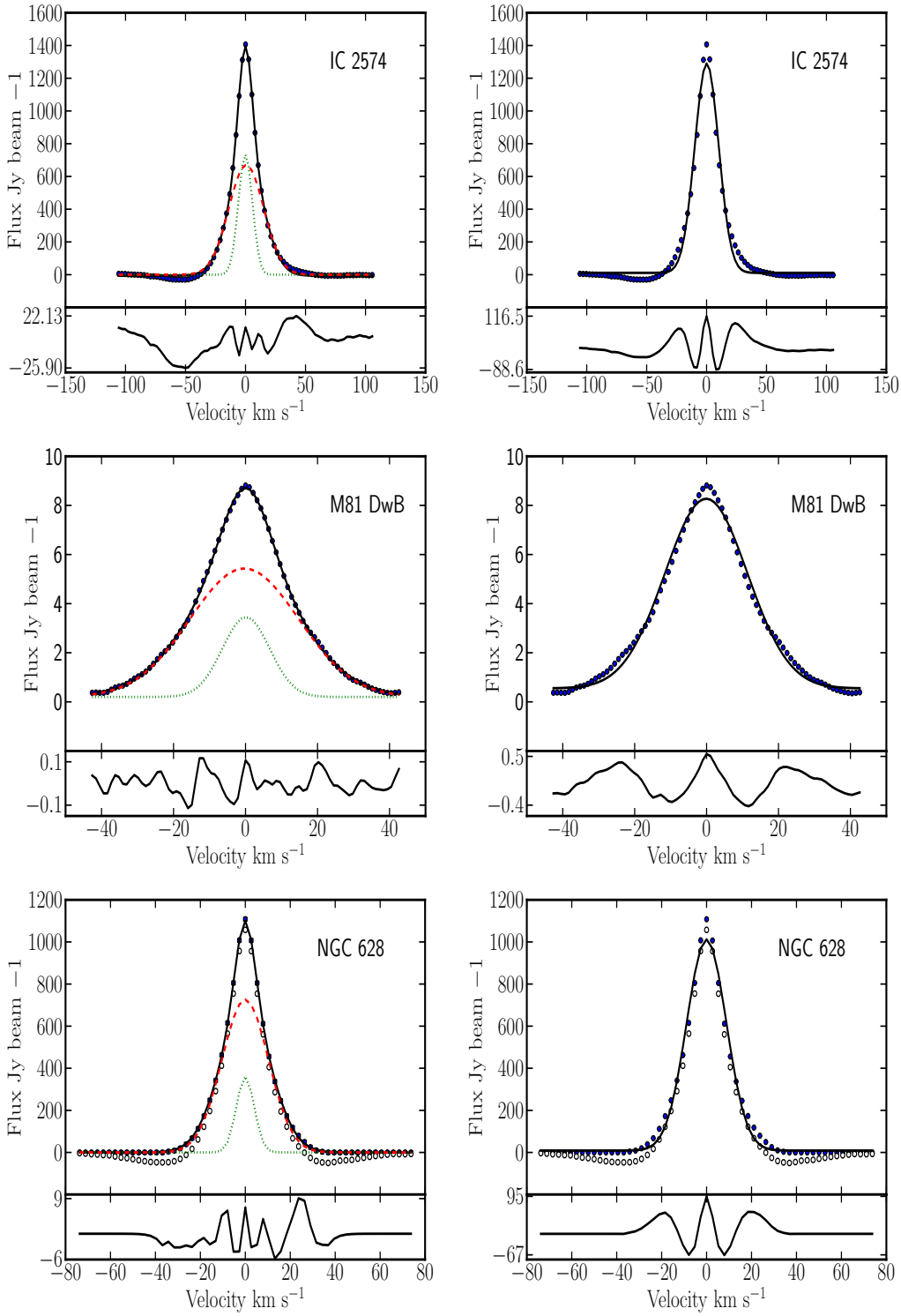

Figure 2.2 (Continued)

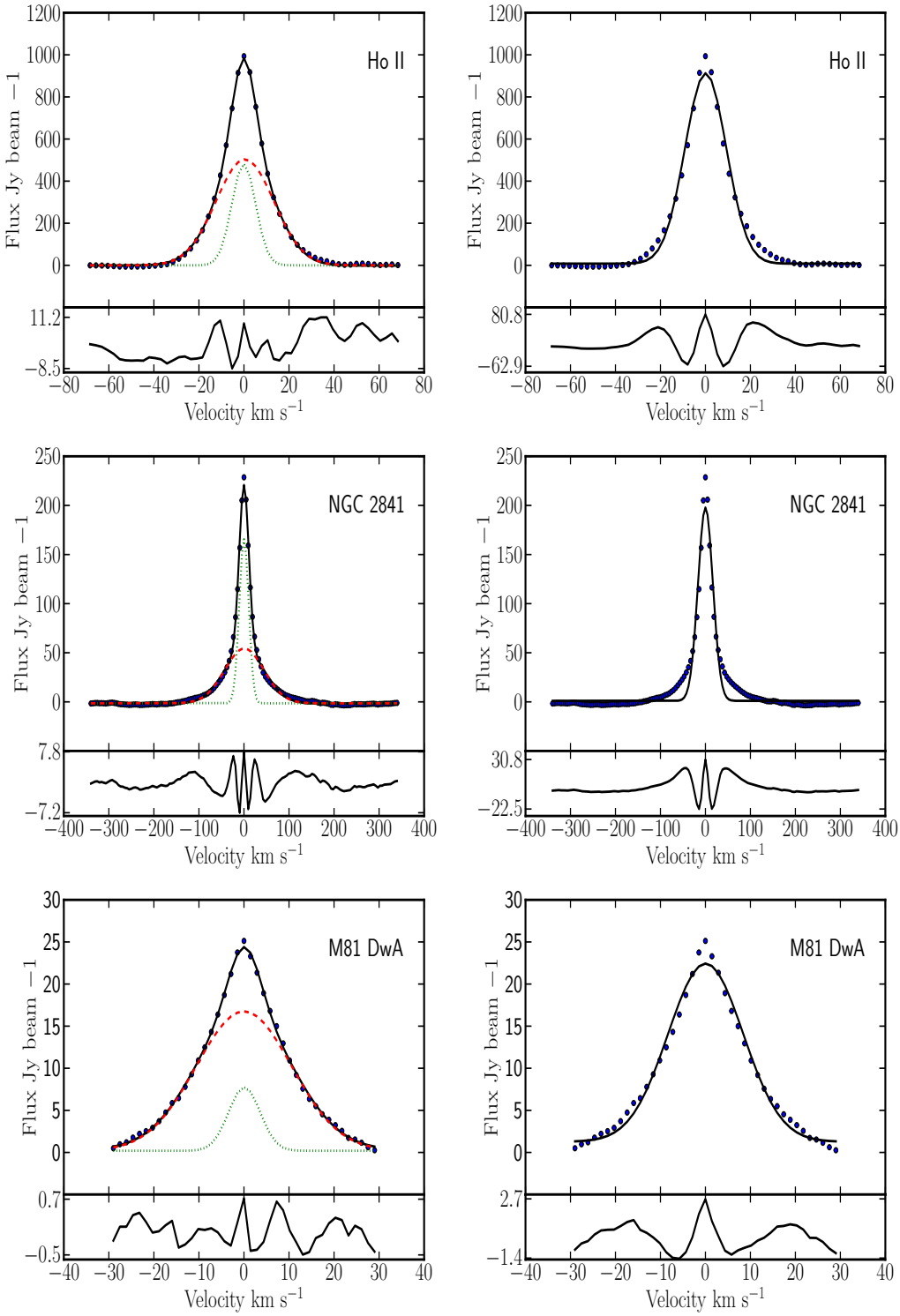

Figure 2.2 (Continued)

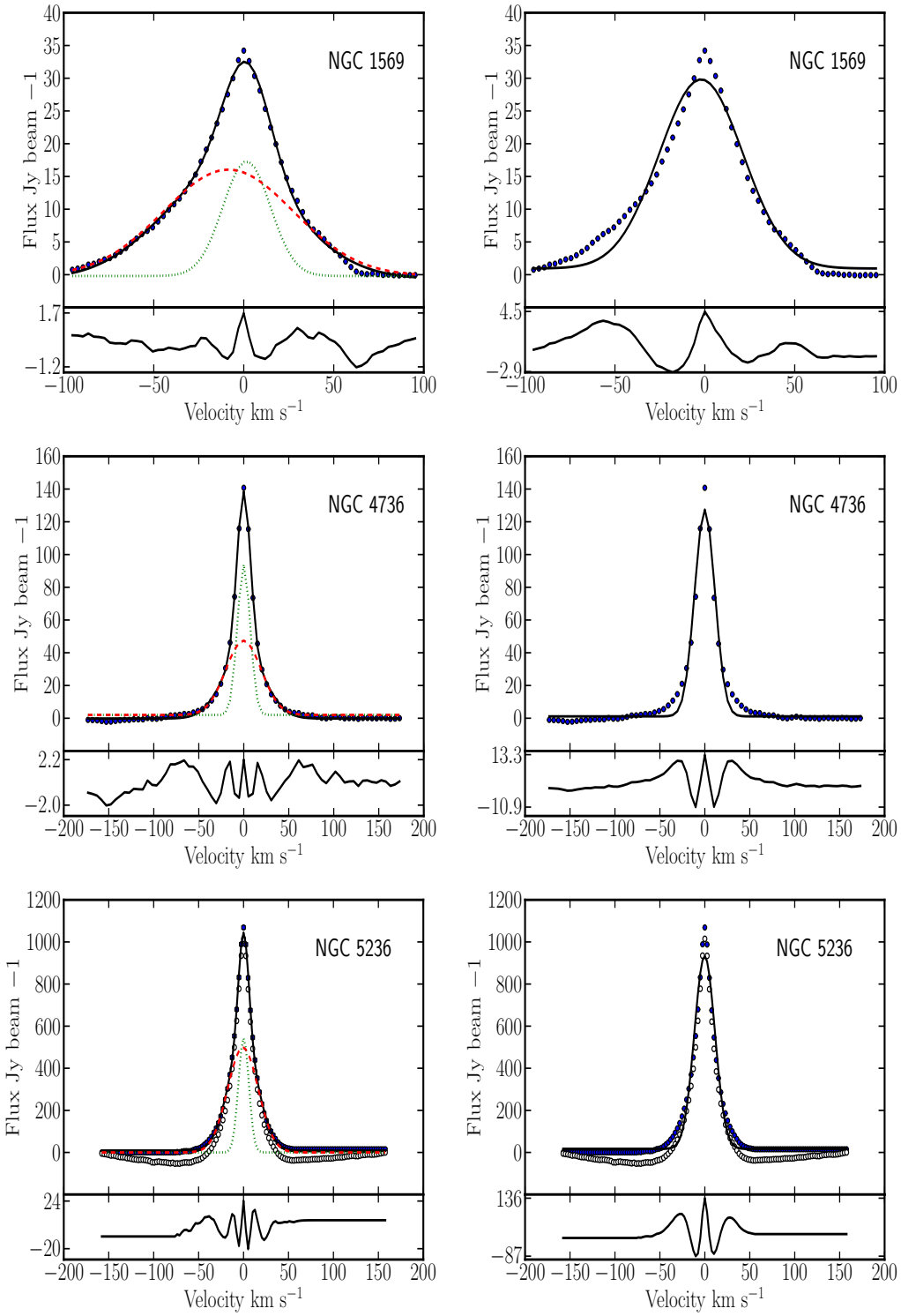

Figure 2.2 (Continued)

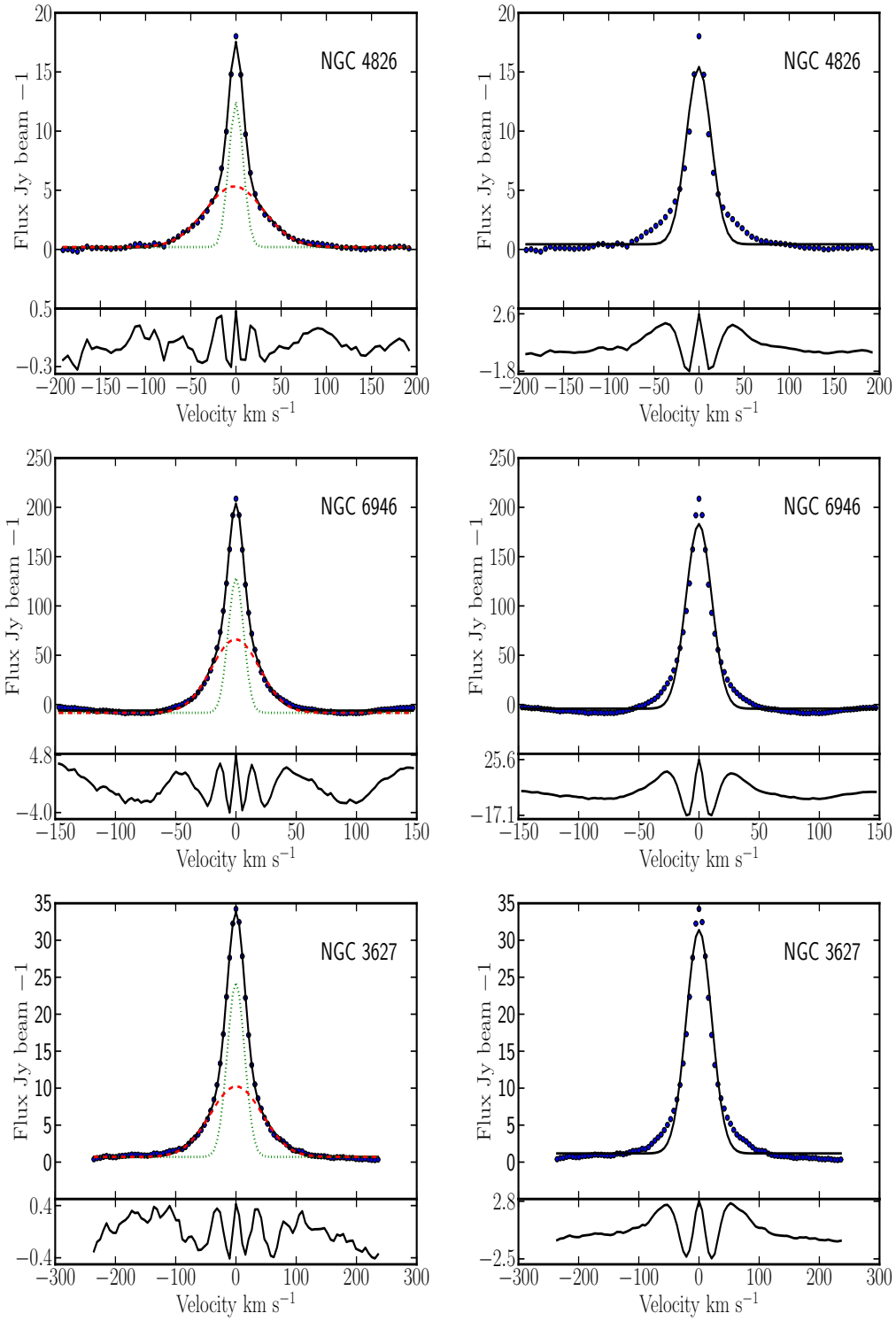

Figure 2.2 (Continued)

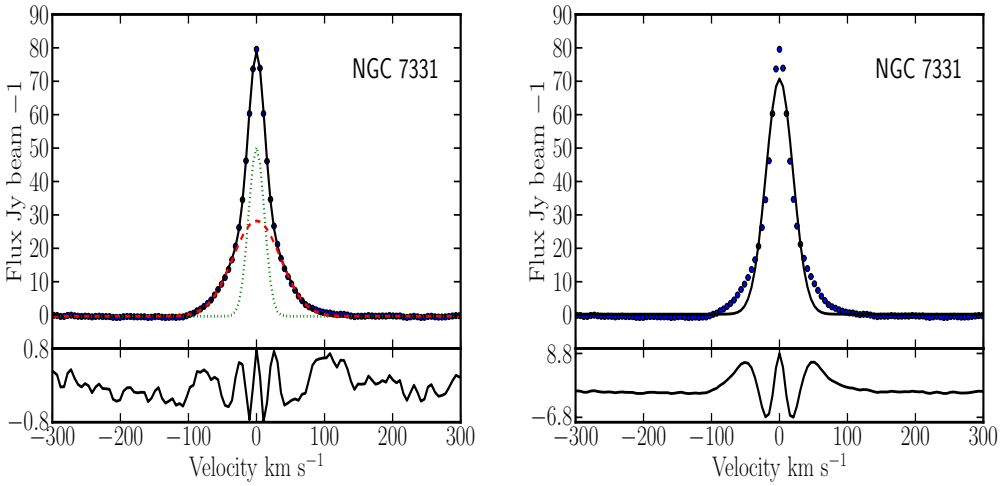

Figure 2.2 (Continued)

ative bowl in some super profiles by fitting and removing a baseline prior to Gaussian fitting. We quantify the quality of the one and two-component fits by comparing their χ^2. A comparison of the χ^2 from the one and the two-component Gaussian fits is shown in Figure 2.3. For illustration, we show in Table 2.1 the ratio between the χ^2 value of the single and double Gaussian fits. This, as well as the amplitude of the residuals in Figure 2.2, convincingly shows that the super profiles are non-Gaussian. All the super profiles are well fitted by two Gaussian components, with one component broader than the other.

The velocity dispersions derived from the single Gaussian fit range from 8.3 km s^{-1} to 23.3 km s^{-1}. The derived velocity dispersions of the narrow component range from 3.5 km s^{-1} to 14.4 km s^{-1} and that of the broad component range from 10.4 km s^{-1} to 54.1 km $^{-1}$. The uncertainties in these values are typically less than 6%.

Figure 2.4 shows histograms of the derived velocity dispersions from both the one Gaussian and two component Gaussian fits. The distribution of the narrow component in Figure 2.4 has a mean of 7.6 $\pm$ 2.6 km s^{-1}, whereas that of the broad component has a mean value of 22.6 $\pm$10.5 km s^{-1}. We summarize in Table 2.1 the fitted parameters of the super profiles of the THINGS galaxies.

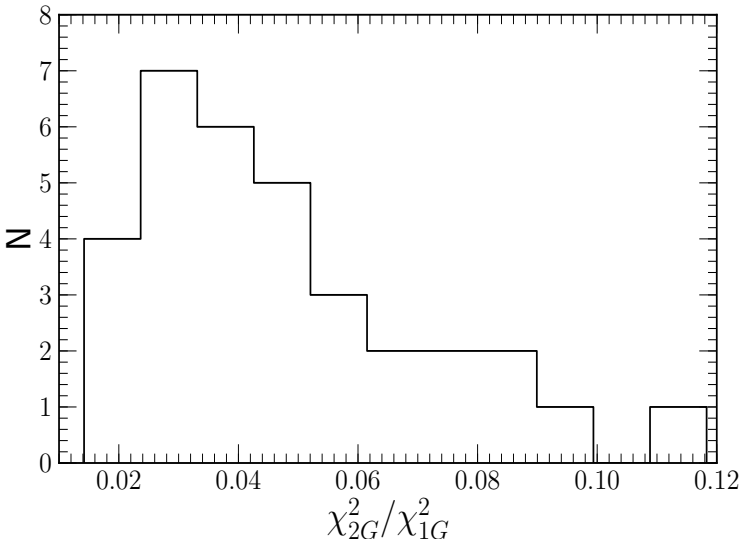

Figure 2.3: Comparison of the reduced χ^2 from the single and double Gaussian fitting. The double Gaussian fitting perform better than the single Gaussian fitting.

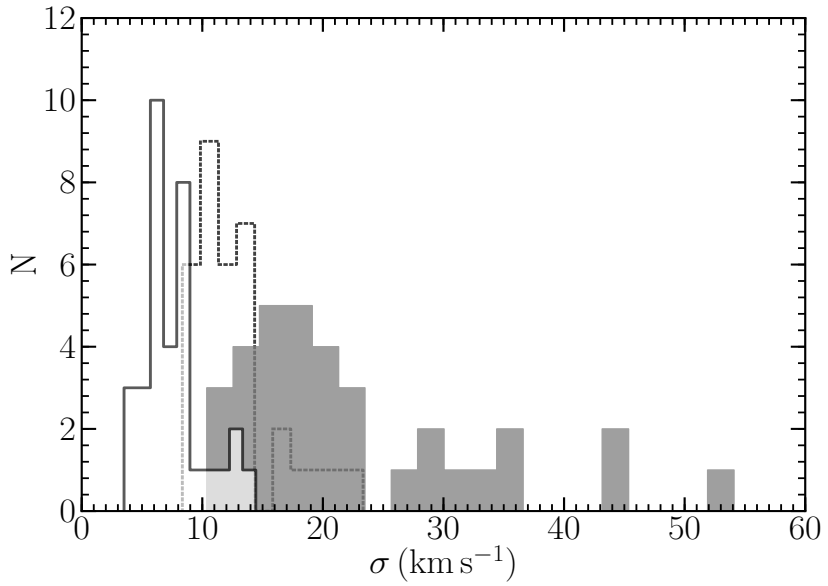

Figure 2.4: Histograms of the derived velocity dispersions from both the one and two-component Gaussian fits. The dotted histogram represents the velocity dispersions derived from the single Gaussian fit. The solid and gray histograms represent the velocity dispersions of the narrow and broad components, respectively.

Table 2.1: Fitted parameters and properties of the THINGS galaxies

Galaxy	σ_{1g}	σ_n	σ_b	deg. asym.	Narr. comp.	Broad comp.	χ^2_{2G}/χ^2_{1G}	N	M_B	SFR	Incl
	[kms^{-1}]	[kms^{-1}]	[kms^{-1}]	[kms^{-1}]	[%]	[%]			[mag]	[M$_\odot$yr^{-1}]	[^{0}]
1	2	3	4	5	6	7	8	9	10	11	12
DDO 53	10.0±0.2	6.2±0.1	15.0±0.2	0.2±0.1	31.6	68.4	0.03	10669	-13.45	0.008	31
DDO 154	9.7±0.1	6.0±0.1	13.0±0.2	0.1±0.1	29.7	70.3	0.04	69359	-14.23	0.004	66
Ho I	9.0±0.2	5.5±0.1	13.5±0.2	0.3±0.1	29.5	70.7	0.04	24825	-14.80	0.006	12
Ho II	9.0±0.2	5.3±0.1	12.8±0.2	0.3±0.1	28.1	71.9	0.04	144794	-16.87	0.070	41
IC 2574	10.0±0.2	5.9±0.2	14.6±0.3	0.5±0.2	32.0	68.0	0.08	223892	-18.11	0.120	53
M81 dwB	11.2±0.2	6.6±0.1	15.1±0.2	0.2±0.1	21.7	78.3	0.04	1865	-14.23	0.005	44
M81 dwA	8.3±0.2	3.5±0.2	10.6±0.3	0.1±0.2	12.2	87.8	0.12	7182	-11.49	0.001[1]	23
NGC 3031	11.3±0.2	6.9±0.1	19.6±0.2	2.9±0.2	39.1	60.9	0.05	485575	-20.73	1.060	59
NGC 628	8.5±0.2	4.0±0.2	10.4±0.2	0.0±0.2	18.8	81.2	0.02	306616	-19.97	1.210	7
NGC 925	12.9±0.2	8.1±0.1	20.7±0.4	0.2±0.2	33.3	66.7	0.03	46305	-20.04	1.090	66
NGC 1569	23.3±0.7	13.1±0.4	36.1±1.0	6.9±0.7	27.9	72.1	0.09	8376	-18.12	0.060	63
NGC 2366	12.3±0.3	7.9±0.1	20.3±0.3	1.0±0.2	37.2	62.8	0.03	96350	-17.17	0.130[2]	64
NGC 2403	10.5±0.3	6.2±0.3	15.8±0.5	0.4±0.3	34.4	65.6	0.06	1039382	-19.43	0.850	63
NGC 2841	16.6±0.4	10.6±0.1	45.1±0.9	0.8±0.7	41.9	58.1	0.06	94392	-21.21	0.200	74
NGC 2903	13.6±0.4	8.9±0.2	30.1±0.8	1.7±0.5	43.7	56.3	0.06	184641	-20.93	2.200	65
NGC 2976	12.0±0.3	8.4±0.1	21.2±0.5	1.7±0.3	45.2	54.8	0.03	10682	-17.78	0.100	65
NGC 3077	12.8±0.3	5.7±0.2	17.1±0.3	0.0±0.2	22.2	77.8	0.04	195432	-17.75	0.090	46
NGC 3184	11.5±0.3	6.1±0.1	19.1±0.2	0.6±0.2	30.0	70.0	0.02	88329	-19.92	1.430	16
NGC 3198	13.2±0.3	8.9±0.1	23.1±0.4	0.1±0.2	43.3	56.7	0.03	123636	-20.75	0.850	72
NGC 3351	10.3±0.3	7.0±0.1	22.9±0.6	0.3±0.4	46.4	53.6	0.06	57006	-19.88	0.710	41
NGC 3521	17.7±0.4	12.7±0.2	54.1±1.2	0.4±0.9	47.3	52.7	0.08	79703	-20.94	3.340	73
NGC 3621	11.5±0.3	8.6±0.1	28.4±1.1	4.1±0.7	54.1	45.9	0.08	270228	-20.05	2.090	65
NGC 3627	21.1±0.5	14.4±0.2	44.2±0.9	0.5±0.5	45.0	55.0	0.04	11330	-20.74	2.440	62
NGC 4214	8.7±0.1	4.5±0.1	12.0±0.1	0.0±0.1	23.6	76.4	0.02	184732	-17.43	0.050	44
NGC 4449	14.3±0.2	7.4±0.2	17.9±0.2	0.4±0.2	20.9	79.1	0.04	302941	-19.14	0.371[3]	60
NGC 4736	11.2±0.3	7.5±0.2	23.0±0.7	0.2±0.4	41.9	58.1	0.03	74840	-19.80	0.430	41
NGC 4826	13.8±0.5	8.0±0.2	33.1±0.8	1.6±0.6	36.9	63.1	0.04	10582	-20.63	0.820	65
NGC 5055	14.3±0.4	8.5±0.2	26.0±0.6	0.1±0.4	37.4	62.6	0.06	188930	-21.12	2.420	59
NGC 5194	17.3±0.4	10.0±0.1	29.8±0.4	1.2±0.2	35.2	64.8	0.02	108986	-21.04	6.050	42
NGC 5236	11.0±0.2	5.3±0.2	15.2±0.4	0.4±0.3	27.1	72.9	0.04	260428	-20.77	2.520	24
NGC 5457	12.7±0.2	6.3±0.1	15.3±0.1	0.0±0.1	12.2	87.8	0.02	1642348	-21.05	2.490	18
NGC 6946	10.6±0.2	6.2±0.1	18.5±0.3	0.3±0.2	37.0	63.0	0.07	85779	-20.61	4.760	33
NGC 7331	19.9±0.4	11.6±0.1	35.5±0.3	0.2±0.2	36.7	63.3	0.01	28340	-21.67	4.200	76
NGC 7793	10.7±0.2	6.7±0.1	18.1±0.2	0.0±0.1	37.7	62.3	0.03	117938	-18.79	0.610	50

Column 1: Name of galaxy; Column 2: Velocity dispersions derived from the one component Gaussian fit; Column 3: Velocity dispersions of the narrow component; Column 4: Velocity dispersions of the broad component; Column 5: Degree of asymmetry of the super profiles defined as the offset between the peak velocity of the narrow and broad components; Column 6: Mass fraction of the narrow component; Column7: Mass fraction of the broad component; Column 8: Ratio of the χ^2 values from the single and double Gaussian fitting; Column 9: Number of individual profiles used to make super profiles. Column 10: Absolute B magnitude (Walter et al. 2008); Column 11: Unless noted, the star formation rate is quoted from Walter et al. 2008; Column 12: Inclination (Walter et al 2008)
Notes: 1: Weisz et al. 2008, 2: Hunter et al. 2001, 3: Leroy et al. 2008.

3

RELIABILITY OF THE SUPER PROFILE SHAPE PARAMETERS

In the previous section, we have derived and analyzed the super profiles without taking into account the various effects and uncertainties that may change the intrinsic shapes of the profiles. We explore some of these effects in this section and investigate whether they affect the shapes of the super profiles. Most importantly, we want to explore whether the non-Gaussianity of the super profiles can be caused by these systematic effects. The following section deals with this issue. In section 3.1, we investigate the effect of resolution on the shapes of the super profiles. In section 3.2, we show the effect of inclination on our measured velocity dispersions. In section 3.3, we test whether the non-Gaussianity of the super profiles is caused by the effect of a few high intensity profiles. In section 3.4, we investigate whether the presence of a thick disk affects the shapes of the super profiles. In section 3.5, we check whether there is a correlation between asymmetry in the HI morphology and asymmetry in the profiles.

3.1 Resolution effects

3.1.1 Beam smearing and rotation gradient

The gradient in rotation velocity across the finite angular size (beam) of a telescope can broaden the HI velocity profile. This effect is called "beam-smearing". Beam smearing may also cause profile asymmetry (e.g. Haynes

et al. 1998). A simple explanation on how beam-smearing affects the width of a profile is given in Petric and Rupen (2007). In summary, for a purely rotating gas disk moving in a circular orbit of velocity V_C, the observed radial velocity for any given position (x,y) can be expressed as,

$$V_z(x, y) = V_z(R, \theta)\cos(i) + V_C(R)\sin(i)\cos(\theta) + V_{los} \tag{3.1}$$

where i is the inclination, θ is the position angle measured in the plane of the gas disk and V_{los} is the line of sight velocity with respect to the observer. If the inclination is small, the quantity $V_C(R)\sin(i)\cos(\theta)$, which measures the gradient in rotation velocity, is small. However for a higher value of the inclination i, the gradient in rotation velocity is also higher and this will broaden the width of the profile. Thus beam-smearing is more pronounced for highly inclined galaxies. In the next section, we investigate whether beam-smearing is a serious problem in our super profile shape analysis.

3.1.2 Quantifying the effect of the resolution on our measurements

Here we quantify the effect of the resolution on the shapes of the super profiles. We do this by constructing a model data cube using the GIPSY task GALMOD. We make a model of NGC 2403 using the same position angle, inclination (60^o) and rotation velocity as the real galaxy itself. We adopt a vertical Gaussian scale height of 100 pc and an intrinsic velocity dispersion of 8 km s^{-1}. In addition, we make a model of NGC 2403 using the above parameters but now at an inclination of 80^o (note that the highest inclination of our sample is 76^o). We simulate observations of the model data cube at different resolutions and create the corresponding super profiles. We fit the super profiles both with one Gaussian and two Gaussian components to see how the dispersion changes with resolution as well as to check whether the latter can create a broad component. Our results are summarized below.

For the 60^o inclination, at 8$''$ resolution (the resolution at which NGC 2403 was observed by THINGS), beam-smearing broadens profiles by $\sim 7\%$. Moreover, the result from the two-component fit shows that only about 2% of the total flux resides in the broad component. Note that in real data, for NGC 2403, the broad component accounts for about 70% of the total flux. For comparison, we show in Figure 3.1 the observed and simulated super

Table 3.1: Effect of the resolution on the shapes of the super profiles

inclination	Resolution	velocity dispersion		
		σ_{1G}	σ_n	σ_b
[°]	[″]	[kms^{-1}]	[kms^{-1}]	[kms^{-1}]
60	8	8.6	8.6	14.8
	20	9.3	9.1	16.3
	60	12.6	10.9	21.1
80	8	10.1	9.4	17.2
	20	11.3	10.1	19.4
	60	16.3	13.0	28.7

σ_{1G}: Velocity dispersions derived from one-component Gaussian fit. σ_n: Velocity dispersions of the narrow component. σ_b: Velocity dispersions of the broad component.

profile of NGC 2403 after smoothing the model data cube to 8″ resolution. At 20″ resolution (about two times the working resolution of the THINGS data), beam-smearing adds ∼16% to the line width. The broadest of the two components required in the two-component fit contains about ∼8% of the total flux. At 60″ resolution, beam-smearing broadens profiles by ∼ 57%. The broad component amounts to ∼32% of the total flux. Thus, at 60° inclination, even after smoothing our model data cube to about 6 times the average working resolution of the THINGS data, we still do not recover the observed shape of the super profiles.

For the 80° inclination, where we expect more rotation within the beam, at 8″ resolution, we find a broadening of ∼ 2 km s^{-1} (26%) from beam-smearing. The broad component contribution to the total flux is ∼18%. At 20″ resolution, about 41% of the observed super profile width is an artifact of the resolution. The broad component has ∼26% of the total flux. Finally, at 60″ resolution, the one component Gaussian fit shows that the broadening from beam-smearing is roughly equal to the intrinsic linewidth and the broad component accounts for about 43% of the total flux. Our fitted parameters are summarized in Table 3.1.

Our conclusion is that, at the THINGS resolution, beam-smearing ac-

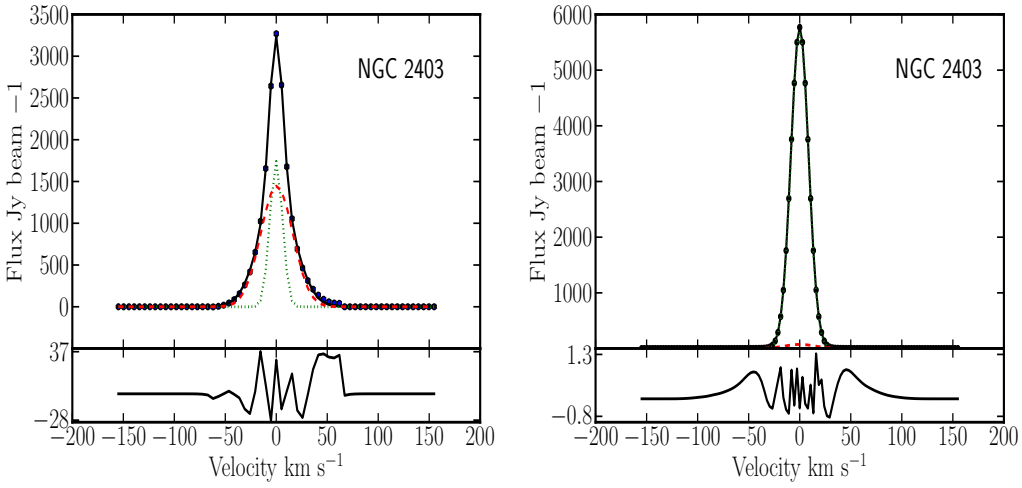

Figure 3.1: Observed (*left panel*) and simulated (*right panel*) super profiles of NGC 2403 at 8″ resolution. The filled circles indicate the data points. The dotted (green) and the dashed (red) lines represent the narrow and broad components required in the double Gaussian fitting. The black solid lines represent the results of the double Gaussian fitting. The bottom panels represent the residuals from the fits.

counts for at most 26% of the observed line width. Note that this fraction was derived from a model galaxy with 80° inclination and is therefore a very strict upper limit, as the highest inclination in our sample is 76°. Moreover, beam-smearing is unable to explain the broad and narrow componentss extracted from the observed super profiles since in real data the broad component accounts for about 70% of the total flux, however, in our models at the THINGS resolution, our artificial broad component contributes at most 18% of the total flux. Again this is a strict upper limit.

3.2 Inclination effect

Projection effects have always been a problem in line profile analysis and are particularly important for low resolution surveys. If a galaxy is seen face-on, then we do not see the rotation of the gas along our line of sight and measure the (vertical) velocity dispersion. However, for an edge-on system, the gradient in rotation velocity within the beam will be maximal and this will broaden the HI profiles. Moreover, for an edge-on galaxy, the contribution of the tangential and radial components of the velocity dispersion

becomes important. Intermediate inclinations will result in smaller broadening. Despite the fact that the THINGS galaxies have been observed at a high resolution, these effects still play a role in our super profile shapes. Projection effects for the THINGS galaxies are also discussed in Leroy et al. (2008) and Tamburro et al. (2009). Figure 3.2 shows a plot of velocity dispersion against inclination. We clearly see that galaxies with higher inclination tend to have broader profiles. The top left panel is for the narrow component. The top right panel is for the broad component and the bottom left panel is for the one Gaussian component. The solid lines are linear least squares fits with slopes of 0.055±0.018 for the one Gaussian component, 0.072±0.016 for the narrow component and 0.11±0.04 for the broad component. Some galaxies do not follow the observed trend between inclination and velocity dispersion. These include NGC 1569, NGC 5194, NGC 2841, NGC 3627, NGC 3521, and NGC 7331. This is most likely because there are strong sources of turbulence or bulk motion in these galaxies that cause their apparently high velocity dispersion as we will show later. These galaxies are marked with different symbols in Figure 3.2. The broad and narrow componentss have the same projection effect and by taking the ratio of their velocity dispersion, the effect of inclination is cancelled. This is illustrated in the bottom right panel of Figure 3.2. The solid line represents a weighted average value with $\sigma_n/\sigma_b \backsimeq 0.37 \pm 0.04$.

3.3 Effect of high intensity profiles

A possible explanation of the non-Gaussianity could be that the shapes of the super profiles are dominated by a few high intensity profiles. The super profiles could be a sum of high intensity narrow HI profiles originating from small regions of high column density and low intensity broad HI profiles originating from much larger low column density regions. Since we are summing individual profiles, this could result in the broad wings and narrow peaks features seen in our super profiles. To test this, we normalize the individual profiles by their peak intensity before summing them. This way, we remove any possible effect of a few bright profiles on the super profiles. The normalized super profiles are similar to the original ones. The velocity dispersions of the broad and narrow components derived from the normalized and unnormalized super profiles are compared in Figure 3.3. It is clear from this Figure that there is no significant difference between the normalized and

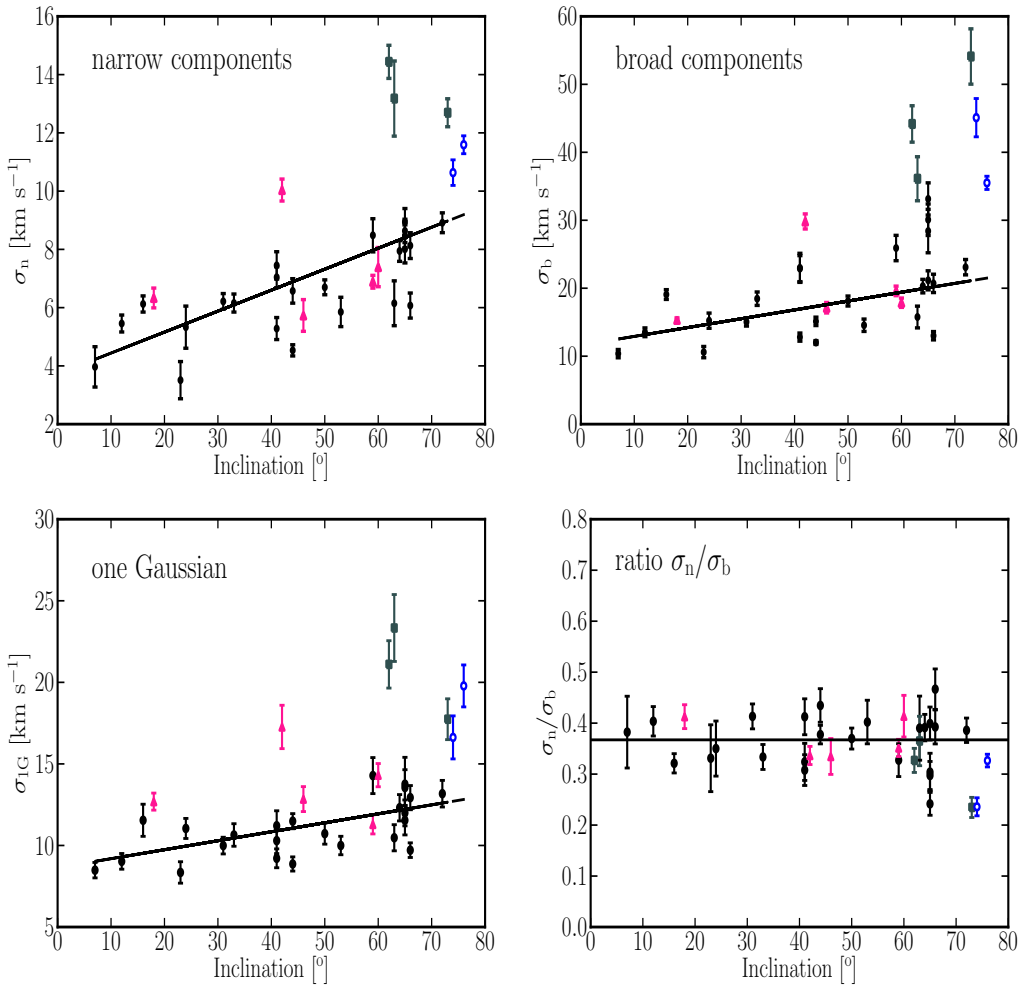

Figure 3.2: Effect of inclination on the measured velocity dispersion. All error bars are 3 σ error bars. The top left panel is for the narrow component. The top right panel is for the broad component and the bottom left panel is for the one Gaussian component. The solid lines are linear least squares fit with slopes of 0.055±0.018 for the one Gaussian component, 0.072±0.016 for the narrow component and 0.11±0.04 for the broad component. The bottom right panel is a plot of the ratio of the velocity dispersion of the narrow component to that of the broad component against inclination. The solid line represents a weighted average value with $\sigma_n/\sigma_b \backsimeq 0.37\pm0.04$. The triangle shaped symbols represent interacting galaxies (those that are tidally interacting with their nearby companion; these are NGC 3031, NGC 4449, NGC 5194, NGC 5457, NGC 3077). The square symbols represent galaxies that are disturbed kinematically due to the effect of e.g., star formation (NGC 1569, NGC 3521, NGC 3627). The open circle symbols indicate non interacting galaxies but having apparently high velocity dispersion (NGC 7331, NGC 2841).

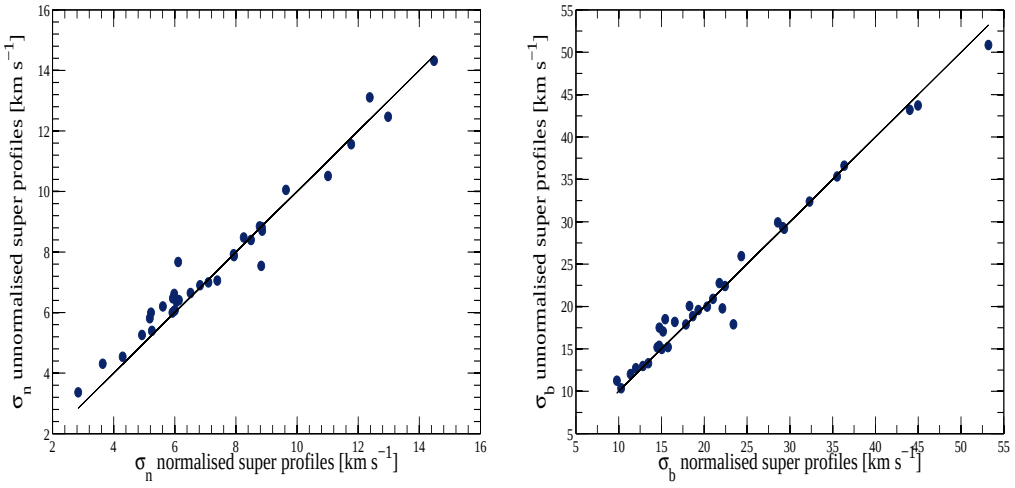

Figure 3.3: Comparison of the derived velocity dispersion from the normalized and unnormalized super profiles. The left panel is for the narrow component and the right panel is for the broad component. The solid lines are lines of equality.

unnormalized super profiles as all the data points closely scatter around the lines of equality. Thus, the shapes of the super profiles are not dominated by a few bright profiles.

3.4 Does the presence of a thick disk affect the shapes of the super profiles?

There is also a possibility that our sample galaxies have a thin disk embedded in a thick HI disk with a lower rotation velocity (Swaters, Sancisi & Van der Hulst 1997). We expect this to asymmetrically broaden profiles. Therefore, if we divide a galaxy into approaching and receding halves and extract super profiles from the approaching and receding sides, we expect the resulting super profiles to be asymmetric and have wings only on one side. Adding the two halves would then result in the observed profiles.

In order to check whether the non-Gaussianity of the super profiles are due to the presence of such a lagging thick disk, we divide each galaxy into approaching and receding halves and study the shapes of the super profiles

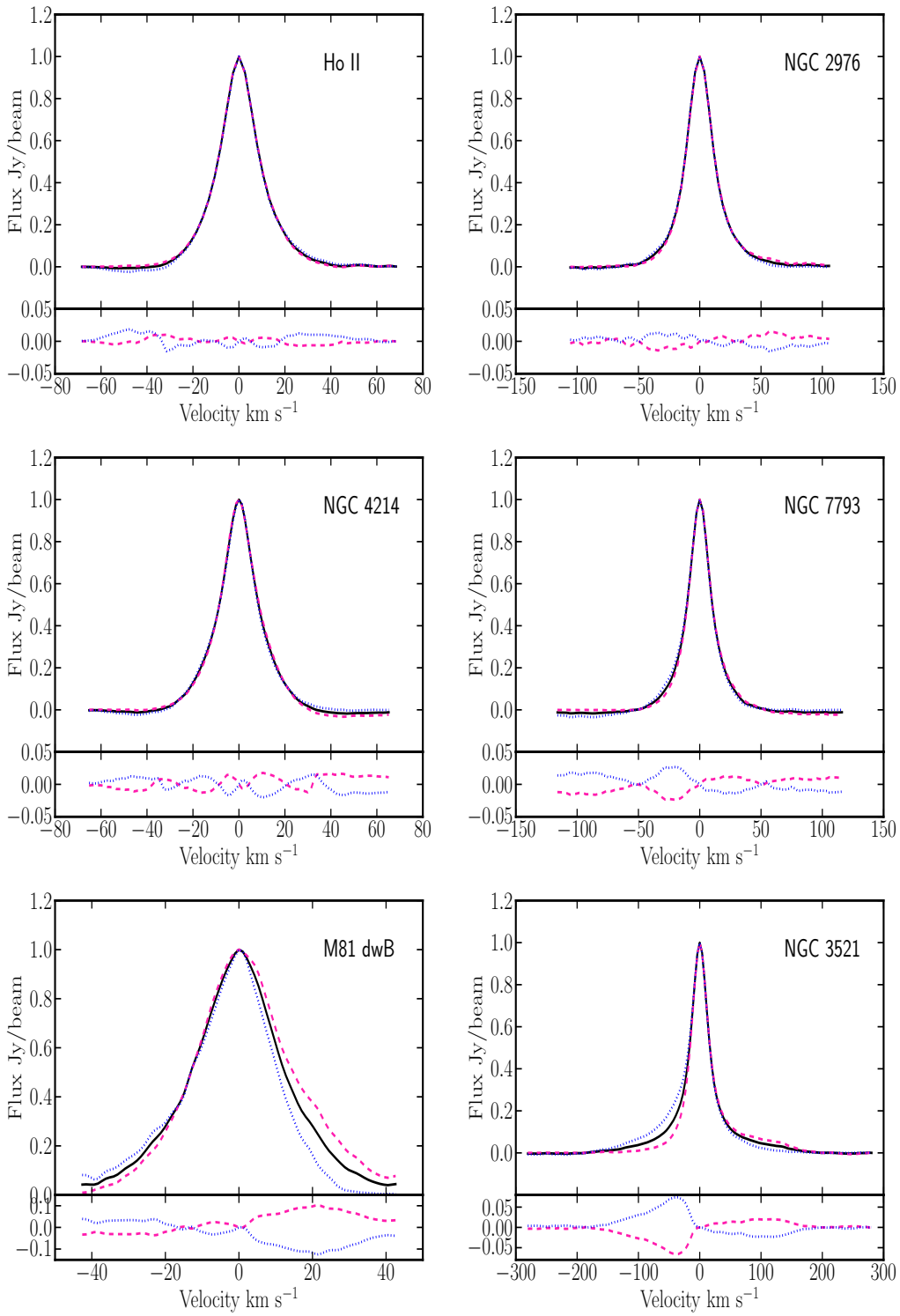

Figure 3.4: Super profiles extracted from the approaching and receding velocity sides of the galaxies represented as dashed and dotted lines plotted on top of the overall super profiles, which are represented by the black lines. The bottom panels represent the difference between the super profiles from the two sides and the total super profiles. The super profiles are normalized to their peak values. The super profiles derived from the receding and approaching sides show no significant one-sided wings.

in the approaching and receding sides. We find no convincing evidence that the presence of a thick disk is able to explain the non-Gaussianity of the super profiles. The super profiles from the two halves show no prominent one-sided wings. The average difference between the normalized super profiles of the two halves and that of the total super profiles is 0.04±0.02. This is not enough to affect our results. Figure 3.4 shows examples of super profiles from the two halves of a few sample galaxies plotted on top of the original ones (the super profiles of the entire disk). Note that in this Figure, the super profiles are normalized to their peak values. Our conclusion is that the effect of a thick disk, if present in our sample, on the shapes of the super profiles is negligible.

3.5 Profile shapes and galaxy asymmetry

Here we check whether there is a correlation between the HI morphology of galaxies and their profile shapes. This is because one might expect galaxies with an asymmetric HI distribution (those with a lopsided HI distribution, see, e.g., Baldwin et al. 1980) to be more likely to be disturbed. This could mean that their gas dynamics can be dominated by bulk motions of the gas which broaden the HI velocity profiles. To check this, we divide each galaxy into approaching and receding halves, extract super profiles from the approaching and receding velocity sides, fit the super profiles with double Gaussian components and then compare the velocity dispersions derived from the two halves of the galaxies. What we expect to find is that for galaxies with a symmetrical HI distribution, the velocity dispersions derived from the approaching and receding sides should be similar, however for those with an asymmetrical HI distribution, the velocity dispersions from the approaching and receding sides could be different. In our sample, eight galaxies show an asymmetric HI distribution. These include NGC 3031, NGC 4449, NGC 5194, NGC 1569, NGC 3198, NGC 2841, NGC 5457, NGC 7331. The rest of our sample has a symmetrical HI distribution (those that show no obvious lopsidedness in their HI distribution).

We compare the velocity dispersions derived from the approaching and receding sides of our sample in Figure 3.5. The largest of the velocity dispersions derived from the two halves of each galaxy are represented by $\sigma_{\rm large}$, whereas the smallest ones are represented by $\sigma_{\rm small}$. If, for example, the ve-

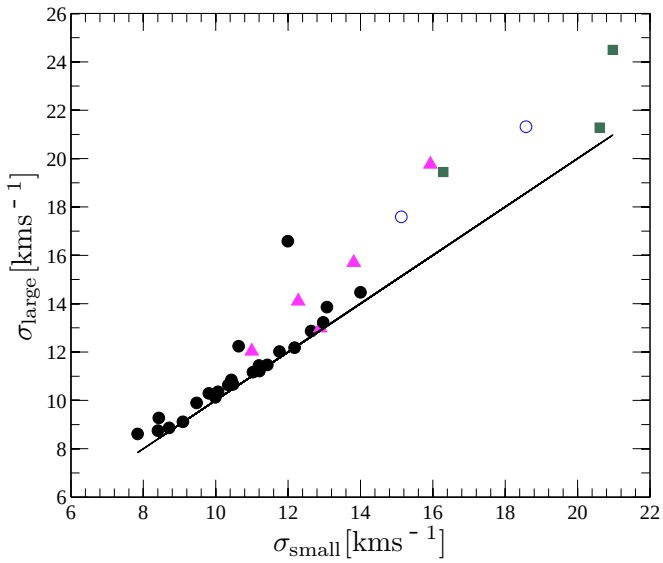

Figure 3.5: Comparison of the width of the super profiles from the approaching and receding sides of the galaxies the broadest and the smallest of which are represented by $\sigma_{\rm large}$ and $\sigma_{\rm small}$, respectively. Filled circles represent non interacting galaxies. Triangle symbols represent interacting galaxies. Square symbols represent kinematically disturbed galaxies. Open circles represent non interacting galaxies but with apparently high velocity dispersions.

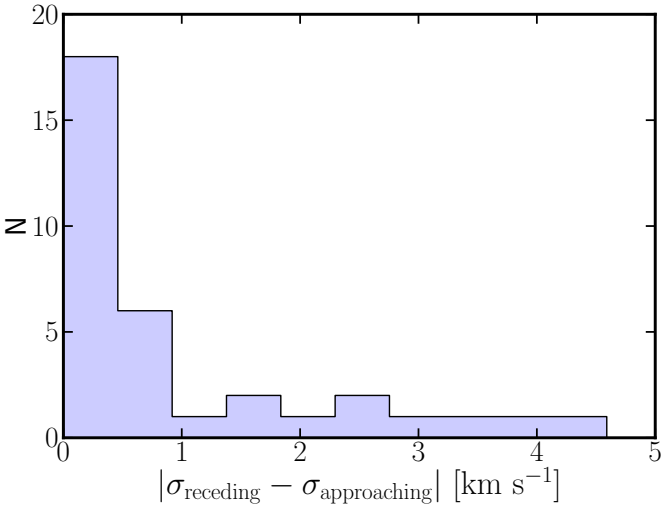

Figure 3.6: Comparison of the velocity dispersions derived from the approaching and receding sides of the galaxies. The difference is below $\sim$ 1 km s^{-1} for most galaxies. Only a small fraction of galaxies have velocity dispersion different by more than 1 km s^{-1} from their approaching and receding sides.

locity dispersions are always larger in one side (approaching or receding), then we would expect all the points in Figure 3.5 to lie well above the line of equality. In the opposite case, if they are similar in the two sides, then all the points will lie close to the line of equality. As Figure 3.5 shows, for most galaxies, the velocity dispersions derived from the approaching and receding sides are similar. Figure 3.6 is a histogram of the difference between the velocity dispersions derived from the approaching and receding sides. For most galaxies, the difference is less than 1 km s^{-1}. Only a small fraction of galaxies have approaching and receding side velocity dispersion different by more than 1 km s^{-1}. These are all, with the exception of NGC 3627, galaxies that did not follow the trend between inclination and velocity dispersion shown in Figure 3.2. By defining interacting galaxies as those that are tidally interacting with their nearby companion (these are NGC 5194, NGC 3031, NGC 5457, NGC 4449, NGC 3077), all but one (NGC 3077) of the interacting galaxies in our sample have velocity dispersions different by more than 1 km s^{-1} between the approaching and receding sides. Most galaxies with asymmetrical HI distribution have velocity dispersions different by more than 1 km s^{-1} between the approaching and receding sides, whereas most of those with symmetrical HI morphology have similar (difference less than 1 km s^{-1}) velocity dispersion in the two sides. Thus there seems to be a correlation between the asymmetry in HI morphology and velocity dispersions.

3.6 Making subsamples

Based on the previous analysis, it is clear that the effects of interaction and inclination are obvious in the super profiles of some galaxies. In order to identify galaxies that are not dominated by these projection effects, interaction or any other systematic effects, we proceed as follows. We divide our sample galaxies into two different subsamples. Sample 1 includes galaxies that closely followed the trend between inclination and velocity dispersion shown in Figure 3.2 and have velocity dispersions in the approaching and receding sides which differed by less than 1 km s^{-1} (see section 3.5). Sample 2 comprises the rest of the galaxies which do not fall under the first sample. Based on this subsample criterion, 23 galaxies fall under the first sample, whereas 11 galaxies make up the second sample. Sample 1 is thus expected to be unaffected by interaction and is not very much dominated by projection effects, whereas sample 2 includes interacting and highly inclined galaxies, as

well as those that are disturbed kinematically due to the effect of, e.g., star formation. We discuss below the global as well as the individual properties of the two subsamples.

3.6.1 Sample 1

Figure 3.7 shows the distribution of velocity dispersions of the narrow and broad components from Sample 1. The narrow component velocity dispersions range from 3.4 km s^{-1} to 8.8 km s^{-1} and have a mean of 6.6 km s^{-1} $\pm$ 1.5 km s^{-1}. The broad component velocity dispersions range from 10.4 to 29.2 km s^{-1} and have a mean of 17.8 km s^{-1} $\pm$ 4.8 km s^{-1}. These values differ slightly from previously derived velocity dispersions for dwarf galaxies. Young and Lo (1996a, 1997) and Young et al. (2003) found narrow component velocity dispersion of 3-5 km s^{-1} and broad component velocity dispersion of 8-12 km s^{-1} in a sample of 5 dwarf galaxies. De Blok and Walter (2006) found a mean velocity dispersion of 8 km s^{-1} for the broad component, and 4 km s^{-1} for the narrow component in NGC 6822, a nearby Local Group dwarf galaxy. Part of the difference might be due to the fact that we have a larger sample with a larger range in properties and therefore much wider range in velocity dispersions. Young and Lo (1996a, 1997), Young et al. (2003), de Blok and Walter (2006) analyzed only dwarf galaxies but here our sample includes spiral galaxies.

3.6.2 Sample 2

Here we describe the individual as well as the global properties of sample 2 to see if we can explain the reason for their higher velocity dispersion values.

Individual properties

NGC 1569 is a magellanic dwarf Irregular galaxy which underwent a strong burst of star formation 5-10 Myr ago (e.g. Vallenari & Bomans 1996, Greggio et al. 1998). Stil and Israel (1998) showed evidence that NGC 1569 is interacting with a nearby massive HI cloud, which they called NGC 1569-HI. The existence of this HI cloud was confirmed by Mühle, Hüttemeister, Klein and Wilcots (2005), where they suggest that it originates from tidal interactions with an intergalactic cloud. They also showed that the velocity field of NGC 1569 is highly disturbed in the central region of this galaxy.

Thus, the aftermath of a burst of star formation together with the interaction with the HI cloud might then be responsible for the very high velocity dispersion of NGC 1569.

NGC 3031 (M81) is an early type spiral galaxy and is in tidal interaction with its companion NGC 3034 (M82) and NGC 3077. The overall velocity dispersion of this galaxy is similar to that of a non-interacting system with similar inclination. However, its velocity dispersions derived from the approaching and receding velocity sides differ by > 1 km s^{-1}. For this galaxy, the approaching side has the largest velocity dispersion which indicates that this side is more disturbed than the receding side.

NGC 3627 belongs to the Leo Triplet and is classified as an SABb type galaxy (Chemin et al. 2003). Its morphology shows evidence of interaction with its nearby companion NGC 3628 (Haynes et al. 1979). Trachternach et al. (2008) made a harmonic decomposition of the velocity field of this galaxy and found that its dynamics are dominated by non-circular motions. Goulding and Alexander (2009) have found AGN signatures in this galaxy. The non-circular motion due to the interaction with the companion might explain its higher velocity dispersion value.

NGC 4449 is an interacting Irregular galaxy with two counter rotating gas components. The presence of this counter rotation was observed by van Woerden et al. (1975) and later confirmed by Bajaja et al. (1994) and Hunter et al. (1998). VLA observations by Hunter et al. (1998) also revealed the presence of streamers in this galaxy. Despite the interaction, the presence of streamers and counter rotation, the overall velocity dispersion is comparable to that of the Sample 1 galaxies. However, the velocity dispersions derived from the approaching and receding sides differ by about 2 km s^{-1}.

NGC 4826 is an early type spiral galaxy classified as Sab. An HI study by Braun et al. (1994) revealed two counter-rotating gas disks in NGC 4826. The inner gas disk has a high column density and rotates in the same direction as the stellar disk, whereas the outer disk has a much lower column density and rotates in the opposite direction to the stellar component. As was shown in Braun et al. (1994), the inner gas disk rotates slightly faster than the outer one. The presence of this counter rotation has been confirmed by an HI kinematic study by de Blok et al. (2008). This counter rotation,

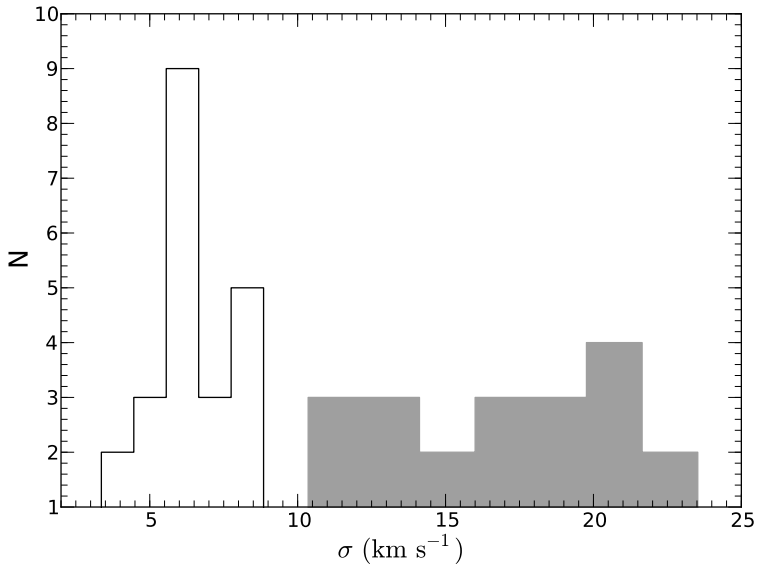

Figure 3.7: Histogram of the derived velocity dispersion from Sample 1. The solid histogram represents the narrow component. The gray histogram represents the broad component.

coupled with the slight difference in the rotation velocity of the two disk components can explain the non-symmetrical characteristics of the super profiles in its two sides. Note that for this galaxy, the velocity dispersions derived from the low and high velocity sides differ by about 4.6 km s^{-1}, which is the largest difference we found in our sample.

NGC 5194 (M 51) is classified as an Sbc galaxy (Sandage and Tammann 1981) with an intermediate inclination of $\sim 42^o$ (Walter et al. 2008). This galaxy is known to be interacting with its nearby companion NGC 5195. AGN signatures have also been found in NGC 5194 (Goulding and Alexander 2009, Goulding et al. 2010). The interaction with NGC 5195 seems to be the origin of the high velocity dispersion value of this galaxy given its intermediate inclination.

NGC 5457 is an Sc galaxy and is tidally interacting with NGC 5474, NGC 5477 and Holmberg IV (Davies et al. 1980). Its HI morphology is asymmetric. The velocity dispersions derived from its two halves differ by about 2 km s^{-1}.

It is not entirely clear what causes the high overall velocity dispersion values of **NGC 2841**, **NGC 3521** and **NGC 7331**. None of them is a starburst system nor do they show clear signs of interaction. Their high velocity dispersion value could just be an inclination effect as they all have inclination higher than the rest of our sample. It is also not clear why their super profiles are quite different for the receding and approaching sides; the same holds true for **M81 DwB**.

Global properties

It is interesting that all but one (NGC 3077) of the interacting galaxies in our sample fall under the second sample classification. Surprisingly, we do not find any obvious effect of interaction on the shape of the super profiles of NGC 3077. Its velocity dispersion is comparable to those of the non-interacting ones. Moreover, the velocity dispersions derived from the approaching and receding sides of this galaxy are very similar, with a difference of only 0.1 km s^{-1}. In addition, the overall super profile of this galaxy is very symmetrical.

Table 3.2 shows the velocity dispersions for Sample 1 and Sample 2. The narrow component velocity dispersions derived from Sample 2 range from 6.4 to 14.3 km s^{-1} with a mean of 9.8 km s^{-1} $\pm$ 2.8 km s^{-1}. The broad component velocity dispersions range from 15.2 to 50.8 km s^{-1} with a mean of 31.0 km s^{-1} $\pm$ 12.4 km s^{-1}. These large linewidths suggest that the ISM in sample 2 galaxies is disturbed. Here the super profiles most likely trace bulk motions of the gas caused by the effect of star formation or interaction. Since we are mainly interested in HI profiles that reflect the intrinsic state of the ISM, we will not consider Sample 2 for further analysis. The rest of the analysis will thus focus on the super profile shapes of Sample 1 (excluding the interacting galaxy 3077), which we define as our Clean Sample. In the next chapter, we do another check on possible systematic effects that may explain the non-Gaussianity of super profiles before doing further analysis of their shapes.

Table 3.2: Velocity dispersions of Sample 1 and Sample 2

	Sample1		
Galaxies	σ_n	σ_b	Incl
	[kms^{-1}]	[kms^{-1}]	[^{0}]
1	2	3	4
DDO 53	6.0 ± 0.1	13.4 ± 0.2	31
DDO 154	6.3 ± 0.1	12.9 ± 0.2	66
Ho I	5.5± 0.1	12.5 ± 0.2	12
Ho II	5.0 ± 0.1	11.8 ± 0.2	41
IC 2574	5.7 ± 0.2	13.6 ± 0.3	53
M81 dwA	3.5± 0.1	10.2 ± 0.2	23
NGC 628	3.7 ± 0.3	9.6 ± 0.2	7
NGC 925	9.1± 0.2	22.1± 0.8	66
NGC 2366	8.2± 0.1	17.8 ± 0.3	64
NGC 2403	6.1± 0.4	14.2 ± 0.7	63
NGC 2903	8.4 ± 0.2	24.9 ± 0.7	65
NGC 2976	8.6 ± 0.1	20.0 ± 0.4	65
NGC 3184	5.9± 0.1	18.1 ± 0.2	16
NGC 3198	8.5± 0.1	19.9± 0.3	72
NGC 3351	7.0± 0.1	21.9 ± 0.7	41
NGC 3621	7.5± 0.2	18.5 ± 0.7	65
NGC 4214	4.2± 0.1	10.9 ± 0.1	44
NGC 4736	7.2± 0.1	20.7 ± 0.7	41
NGC 5055	7.9± 0.1	21.3 ± 0.7	59
NGC 5236	5.1± 0.4	13.8 ± 0.5	24
NGC 6946	6.0± 0.4	18.6 ± 0.1	33
NGC 7793	6.7± 0.1	17.2± 0.2	50
	Sample 2		
M81 dwB	6.6 ± 0.1	15.1 ± 0.2	44
NGC 3031	6.9±0.1	19.6 ± 0.2	59
NGC 1569	13.1 ± 0.4	36.1±0.17	63
NGC 2841	10.6 ±0.1	45.1 ± 0.9	74
NGC 3521	12.7 ±0.2	54.1±1.2	73
NGC 3627	14.4 ± 0.2	44.2 ± 0.9	62
NGC 4449	7.4±0.2	44.2±0.9	60
NGC 4826	8.2±0.2	33.1±0.8	65
NGC 5194	10.0±0.1	29.8±0.4	42
NGC 5194	10.0±0.1	29.8±0.4	42

Column 1: Name of galaxies; Column 2: Velocity dispersions of the narrow component; Column 3: Velocity dispersions of the broad component; Column 4: inclination (Walter et al 2008).

4

SYSTEMATIC UNCERTAINTIES

Now that we have identified a clean sample, which excludes most effects intrinsic to the galaxies themselves, we now quantify possible systematic errors due to the method used and study the shapes of the super profiles of the clean sample in detail. In section 4.1, we check whether our SHUFFLE procedure has been done correctly. We particularly want to understand how small uncertainties in the SHUFFLE velocity value affect the shapes of super profiles and whether the non-Gaussianity of the super profiles can be attributed to these uncertainties. In other words, we want to know whether errors in shuffling create broad components. In section 4.2, we check how individual asymmetric source profiles affect the shapes of the overall super profiles.

4.1 Uncertainties in the SHUFFLE procedure

The choice of velocity to use in a velocity field can lead to uncertainties in the shuffling method. These uncertainties in the shuffle velocity value could artificially broaden super profiles. In order to have an idea of the uncertainties in velocity field values in real data, we show in Figure 4.1 a plot of the fitted amplitude of the individual spectra of NGC 2403 against the uncertainties in the central velocity value of the fitted profiles using a hermite (h_3) function. As Figure 4.1 shows, the fitted velocity values of low amplitude profiles have larger uncertainties than those of high amplitude profiles. This is because low amplitude profiles are more affected by noise than high amplitude profiles. These larger uncertainties in the fitted values of low amplitude

profiles can create an artificial broad component in super profiles. Moreover, even though the uncertainties in the fitted velocity of high amplitude profiles are small, they could still broaden super profiles. We therefore carry out an experiment to quantify the effect of these uncertainties in super profiles. We test the case of all profiles having random offsets as well as the case where the offsets depend on the amplitude of the spectra. To do this, we create artificial data cubes. The data cubes contain only purely single Gaussian profiles, which all have 6 km s^{-1} velocity dispersion but with different amplitudes. We use the observed peak flux distribution of NGC 2403 as input probability distribution for our models. We then randomly pick one thousand amplitudes using this distribution and generate Gaussians using these amplitudes together with a constant velocity dispersion.

We create a data cube using the input spectra described above and derive a velocity field from it, which we refer to as the *true* velocity field. We then add uniform random offsets to the true velocity field and use the modified velocity field to shuffle profiles. Thus, we introduce random uncertainties in the velocities used for shuffling.

For the first case, we give all the input spectra uniform random offsets (between -5 to 5 km s^{-1}, -10 to 10 km s^{-1}, etc.). Here we want to quantify the broadening due to incorrect shuffling.

For the second case, only profiles with amplitudes lower than 25% of the highest amplitude are given uniform random offsets (for the case of NGC 2403, which has a maximum amplitude of 9.2 mJy, this value corresponds to 2.3 mJy). All other higher amplitude profiles are assumed to be perfectly lined up (with zero offsets). Here we want to quantify how much of an offset we need to create an artificial broad component in super profiles. Our results are summarized below.

For the first case, the super profiles get broader as we increase the offsets but the two components retrieved by the double Gaussian fitting are all similar in amplitude and dispersion. In other words, there are *no* broad and narrow components. The results of a single Gaussian fit to the simulated super profiles show that at [-5,5] km s^{-1} offsets, the resulting broadening from shuffling is about 1 km s^{-1}. At [-10, 10] km s^{-1}, the broadening due to shuffling is $\sim$ 3 km s^{-1}. At [-15, 15] offsets, the width of the resulting

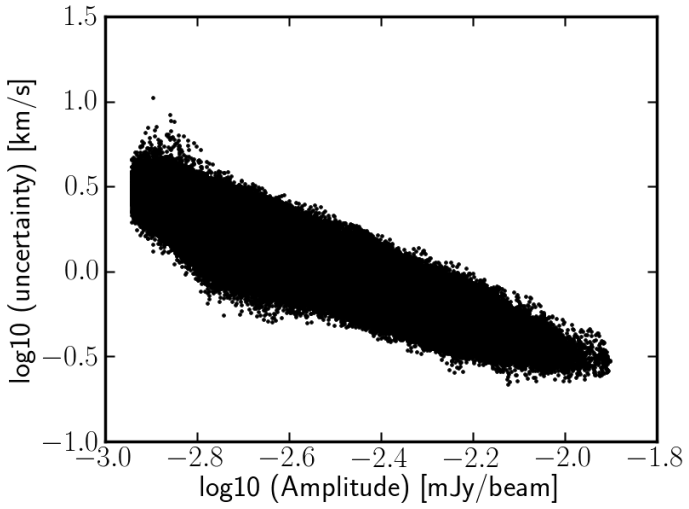

Figure 4.1: A plot of the fitted amplitudes of the individual spectra of NGC 2403 against uncertainties in the central velocity value of the fitted profiles using a Hermite (h_3) function. Lower amplitude profiles tend to have larger uncertainties.

super profiles is twice as large as the width of the input profiles. At [-20, 20] km s^{-1} offsets, the super profiles start to have double peaked features. Figure 4.2 shows examples of simulated super profiles derived by giving all the input spectra uniform random offsets as described above.
For the second case, we start to clearly see the narrow peaks and broad wings features at [-15, 15] km s^{-1} offsets. The wings of the simulated super profiles get more and more pronounced with increasing offsets. Examples of the simulated super profiles using amplitude dependent offsets are shown in Figure 4.3. The dispersions derived from the simulated super profiles are summarized in Table 4.1 for the two cases mentioned earlier for different offsets.

The above results show that we need an offset of at least 15 km s^{-1} to explain the non-Gaussianity of super profiles. As Figure 4.1 shows, leaving out the outliers, the maximum uncertainties in the fitted amplitude is around 5 km s^{-1}. This is three times smaller than the offset required to create a broad component in the artificial data. At [-5, 5] km s^{-1} offsets, which is equal to the maximum uncertainty in the real data, the derived velocity dispersions from either the single or double Gaussian fitting are roughly the same as the velocity dispersion of the input spectra for the two cases mentioned earlier. More specifically, for the second case, the broadest of the two

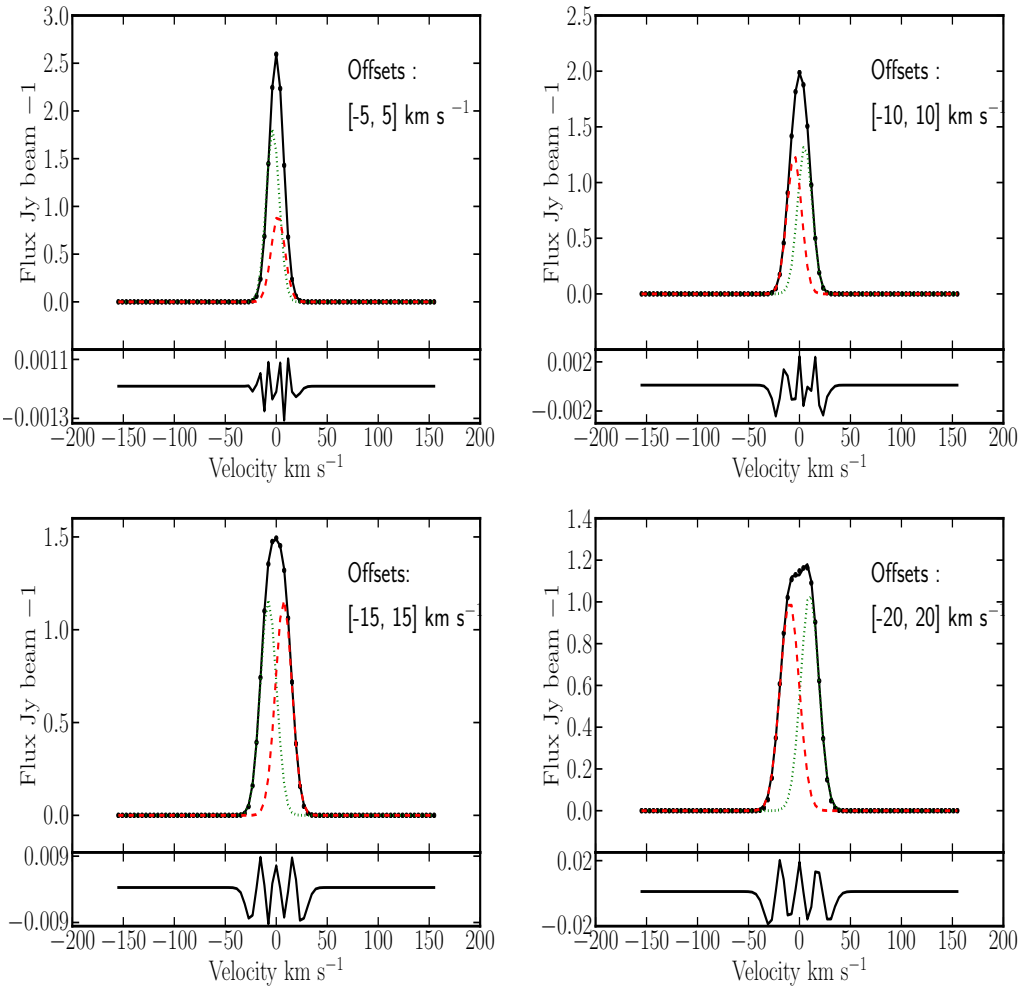

Figure 4.2: Examples of simulated super profiles derived by giving all the input spectra uniform random offsets. The dotted (green) and the dashed (red) lines represent the narrow and broad components required in the double Gaussian fitting. The black solid lines represent the results of the double Gaussian fitting. Bottom panels represent the residuals from the fits.

.

Table 4.1: Velocity dispersions derived from simulated super profiles using different offsets. The input velocity dispersion is 6 km/s.

Offsets (km/s)	Case 1 (km/s)			Case 2 (km/s)		
	σ_{1G}	σ_n	σ_b	σ_{1G}	σ_n	σ_b
-5, 5	7.1	6.5	6.7	6.6	6.1	6.7
-10, 10	9.2	7.1	7.2	6.9	6.2	7.6
-15, 15	11.9	8.0	7.8	7.3	6.1	9.4
-20, 20	15.0	8.8	9.3	7.3	6.1	11.4
-25, 25	.....	.....	.....	7.3	6.2	14.6
-30, 30	.....	.....	.....	7.2	6.2	18.5

Case 1: All profiles are given a random offset (with respect to the *true* velocity field) given in column 1 *Case 2:* All profiles with amplitude lower than 2.3 mJy are given a random offset (with respect to the velocity field) given in column 1 and the higher amplitude profiles are all perfectly lined up (i.e with 0 offset). σ_{1G}: Velocity dispersions derived from a single Gaussian fitting.σ_n: Velocity dispersions of the narrow component. σ_b: Velocity dispersions of the broad component.

components required in the double Gaussian fitting has a velocity dispersion of $\sim$ 6.7 km s^{-1} at these offsets. Thus, we introduce a broadening of only $\sim$11% to the broad component by going from 0 to [-5,5] km s^{-1} offsets.

Our conclusion is that uncertainties in the SHUFFLE procedure are not sufficient to create the broad component that we see in our super profiles, as the offsets required to create a broad component are much larger than inferred for real data. As can be seen in Figure 2.1, a 15 km s^{-1} offset is almost as large as the width of a typical individual profile and it is therefore very unlikely that we make such large errors while doing the SHUFFLE procedure.

4.2 Effects of asymmetric profiles

If the individual profiles that are used in the stacking are themselves asymmetric, this can also lead to non-Gaussianity of super profiles. If, for example, we combine two asymmetric profiles, one negatively skewed and the other one positively skewed, the result will be a profile with broader wings and a narrower peak than a pure Gaussian profile. In the following, we check whether the broad component that we extract from the super profiles are in-

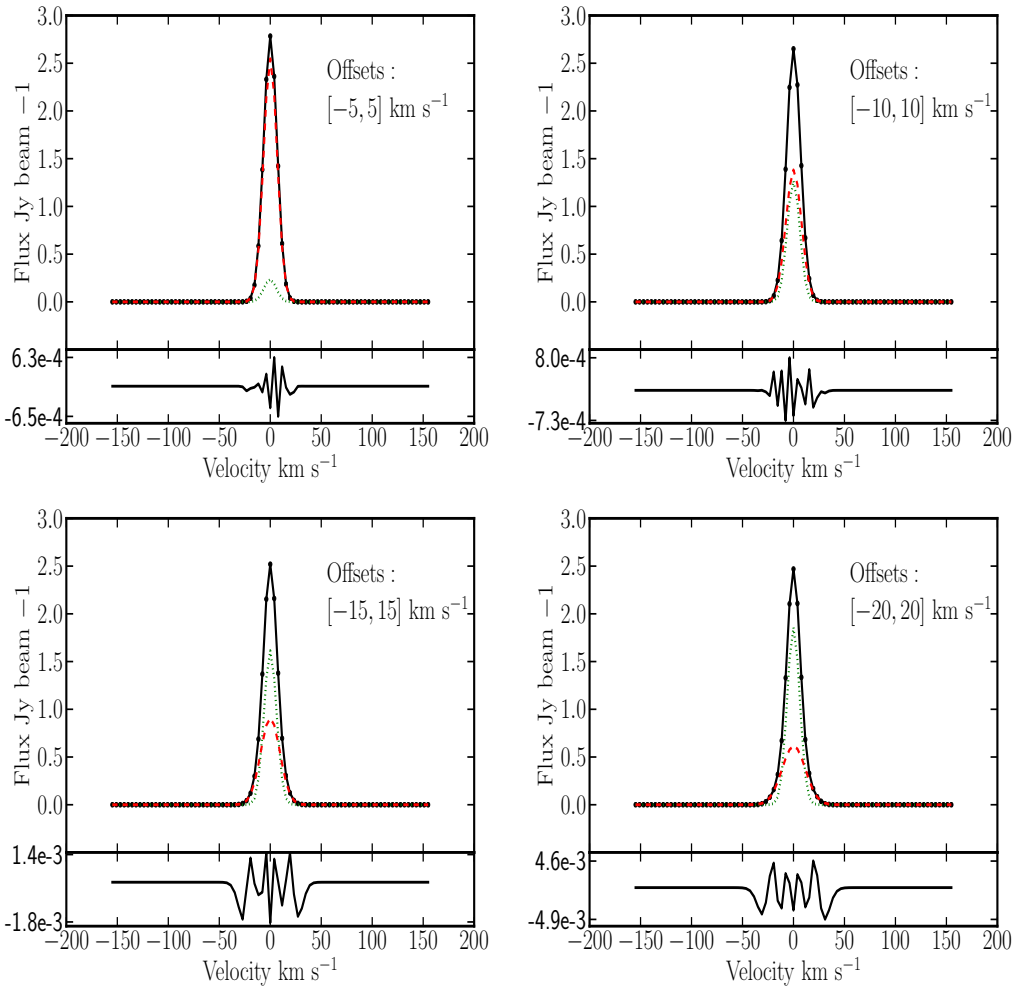

Figure 4.3: Examples of simulated super profiles using amplitude-dependent offsets. The dotted (green) and the dashed (red) lines represent the narrow and broad components required in the double Gaussian fitting. The black solid lines represent the results of the double Gaussian fitting. Bottom panels represent the residuals from the fits.

.

trinsic or artifacts of asymmetric input profiles. We do this by only selecting symmetrical profiles, then create super profiles from those symmetrical input profiles and check if we still have broad and narrow componentss.

To select symmetrical profiles, we create three kinds of masks based on the difference between the hermite-3 (HER3) velocity field values and that of first moment map velocity values (IWM). The idea is that for asymmetric profiles (those with wings on only one side) there will be a difference between the HER3 velocity field values, which tend to be equal to the peak value of the profiles, and the IWM values, which for asymmetric profiles, are skewed towards the wing. For symmetric profiles the difference between HER3 and IWM is small, and by selecting only those profiles, we will have only symmetric input profiles. If we create super profiles from only the symmetric profiles then any broad component that still show up would be intrinsic. We define the three masks as follows:

Mask for symmetric profiles (SP): velocity mask where the difference between HER3 and IWM is between -5 and 5 km s^{-1}.
Mask for left-handed asymmetric profiles (LHAP): velocity mask where the difference between HER3 and IWM is greater than 5 km s^{-1}.
Mask for right-handed asymmetric profiles (RHAP): velocity mask where the difference between HER3 and IWM is smaller than -5 km s^{-1}.
SP should select symmetric profiles whereas the other two masks should only select asymmetrical profiles. We show for all galaxies the location of these symmetric and asymmetric profiles in Figure 4.4. We create super profiles based on the three masks and fit them with both one Gaussian and two Gaussian components. LHAP and RHAP super profiles should only contain asymmetric input profiles whereas those of SP should have only symmetric input profiles. Examples of super profiles created using the three kinds of masks are shown in Figure 4.5. The top left panel is for LHAP super profiles, whereas the top right and bottom panels are for RHAP and SP super profiles, respectively. As can be seen from Figure 4.5, SP super profiles are symmetrical whereas LHAP and RHAP super profiles are more skewed to the left and to the right, respectively.

We compare the dispersions from the original super profiles (i.e. those using all profiles of the entire HI disk as presented in Chapter 2) and from those of SP in Figure 4.6 (top panel). The dispersions of the narrow compo-

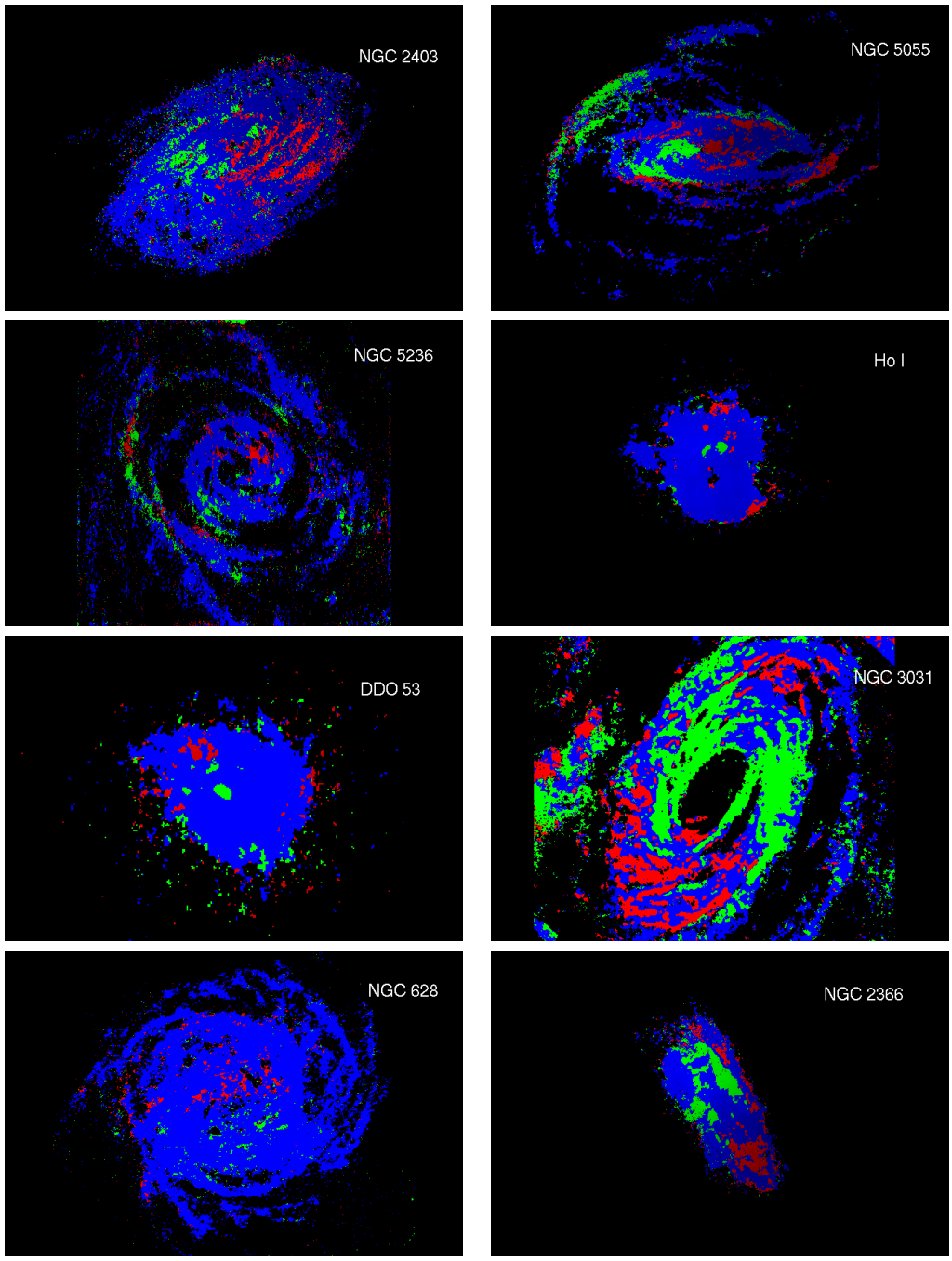

Figure 4.4: Location of symmetric and asymmetric profiles for the THINGS galaxies. Blue pixels represent symmetric profiles (SP). Green and red pixels represent left-handed asymmetric profiles (LHAP) and right-handed asymmetric profiles (RHAP), respectively.

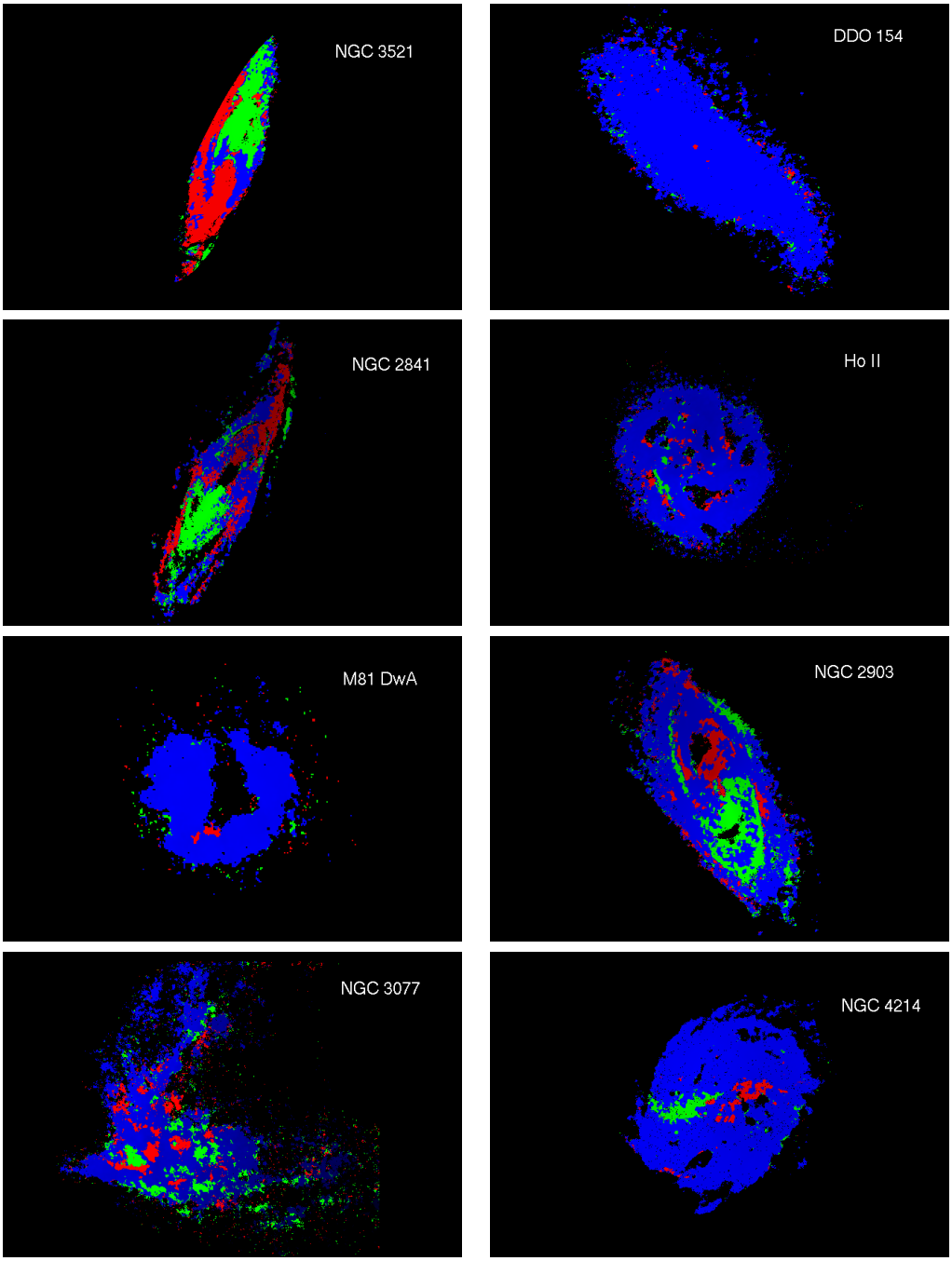

Figure 4.4 (continued).

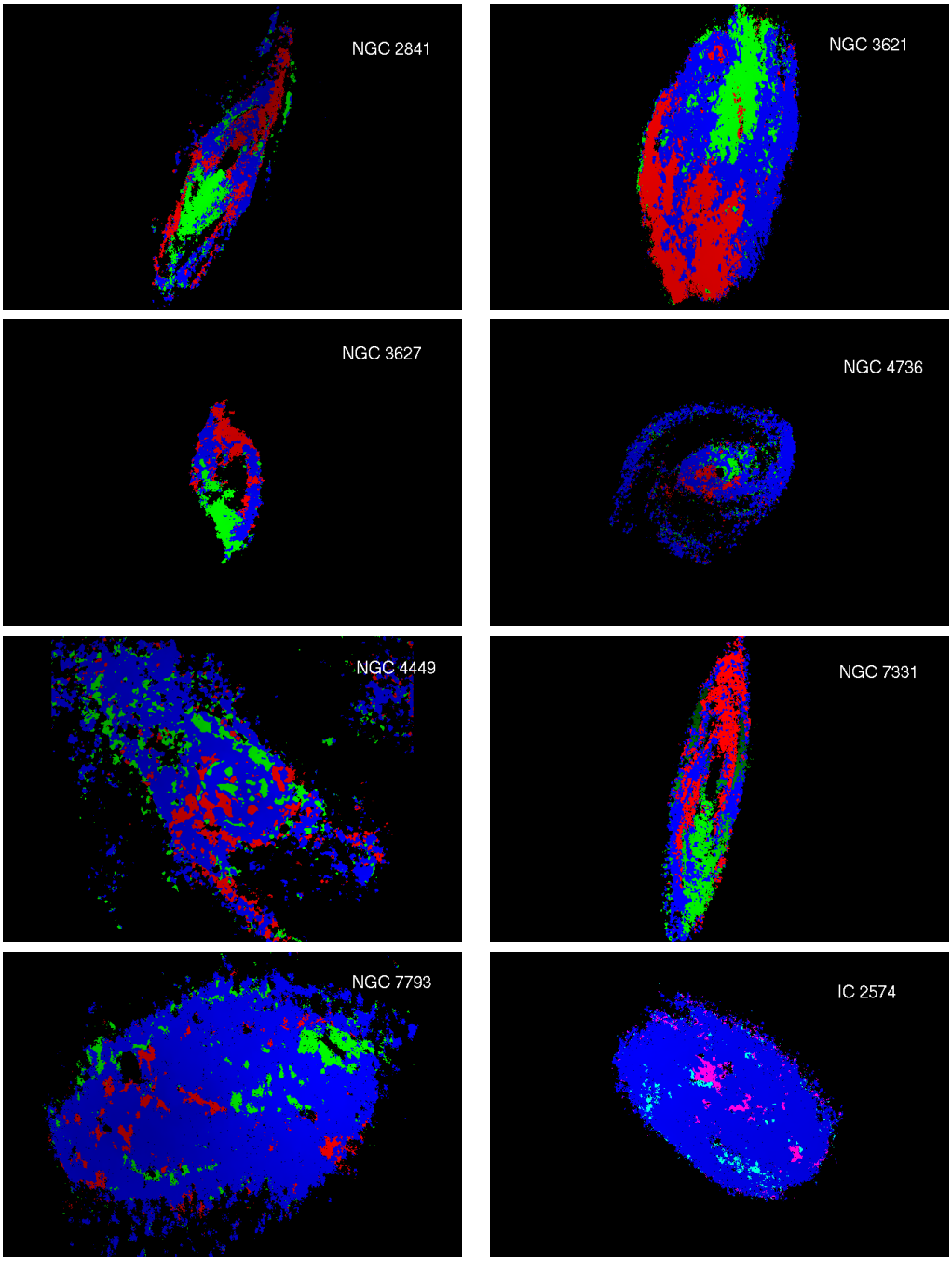

Figure 4.4 (continued).

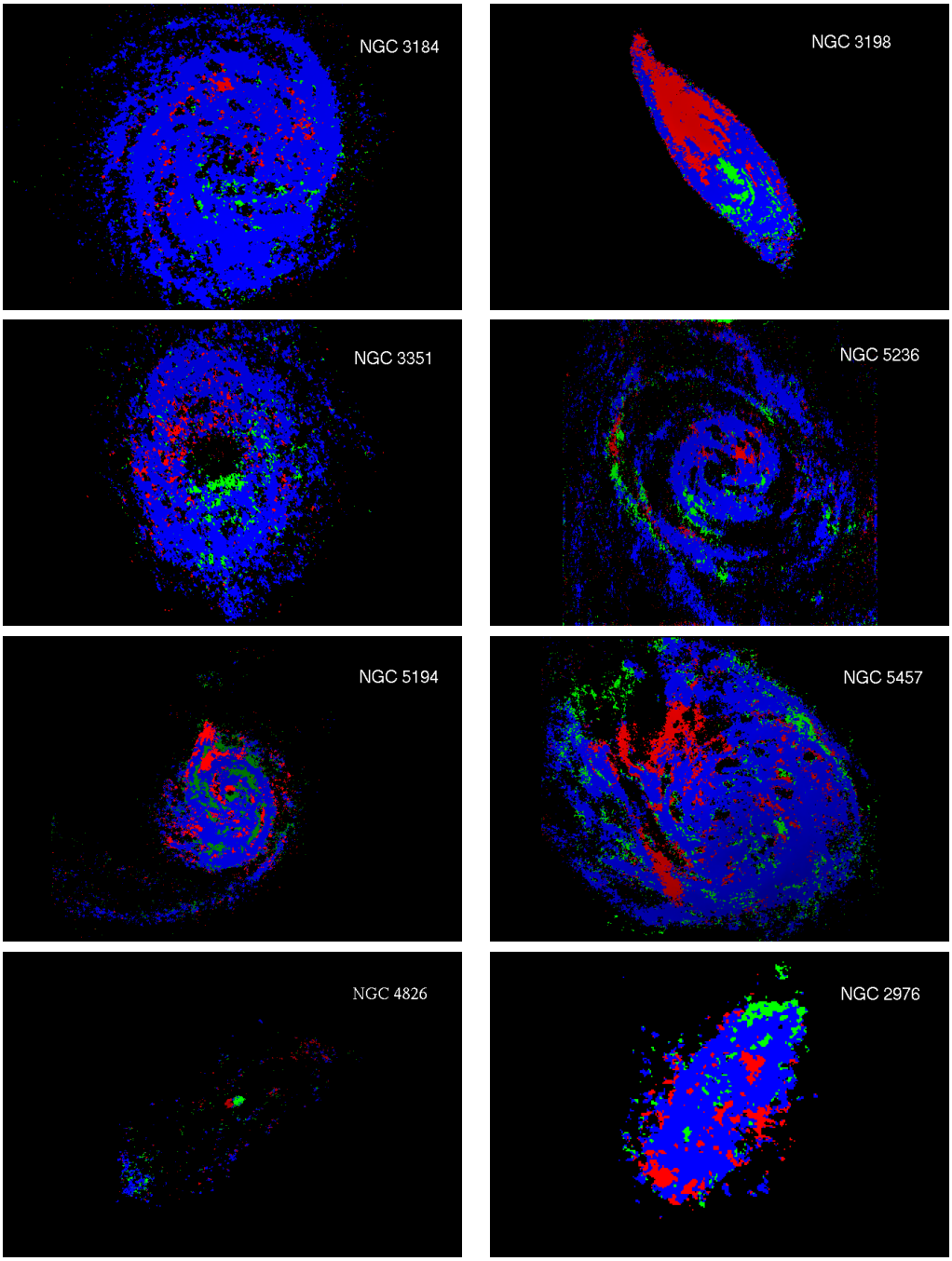

Figure 4.4 (continued).

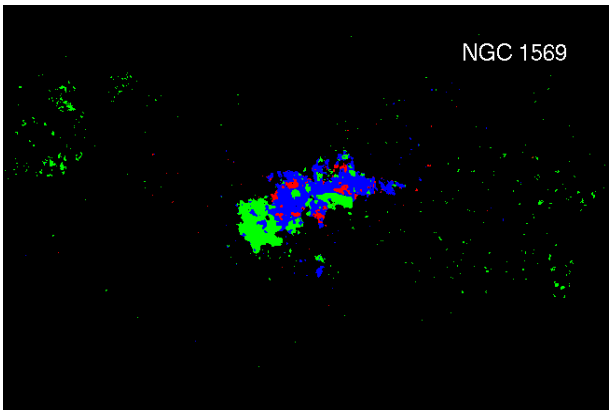

Figure 4.4 (continued).

nent from the original super profiles are similar to those from the SP super profiles. However, the dispersions of the broad component from the original super profiles tend to be greater than those from the SP super profiles. This is what we would expect if the original profiles were broadened by the asymmetry in the input profiles. In other words, asymmetry in the input profiles will lead to an overestimate of the velocity dispersions of the broad component derived from the corresponding super profiles. We can remove this effect by only selecting symmetric profiles.

In order to be sure whether the -5 to 5 km s^{-1} mentioned earlier are good limits to use for the SP, we create another SP where the difference between HER3 and IWM velocity field is between -2 and 2 km s^{-1}. This selects only very symmetrical profiles but at the cost of a reduced number of profiles. Figure 4.6 (bottom panel) compares the velocity dispersions derived from the SP using the 5 km s^{-1} definition and those derived from the SP using the 2 km s^{-1} definition. It is clear that the dispersions derived from SP using the 2 km s^{-1} limit tend to be smaller than those derived from SP using the 5 km s^{-1} limit for the broad component. By going from the 2 to 5 km s^{-1} limit we add a broadening of about 1 km s^{-1} to the broad component. Although we lose about 60 % of the total pixels by going from the 5 to 2 km s^{-1} limit, we still have sufficient S/N to accurately fit the resulting super profiles. As can be seen in Figure 4.6, the error bars associated with the fit parameters of the SP super profiles using the 2 and 5 km s^{-1} limits are similar. We thus use the 2 km s^{-1} limit when the S/N allows us to do so. In the following, we refer to the 2 km s^{-1} limit when we talk about SP, LHAP and RHAP

super profiles. The effect of asymmetry should therefore be minimal in the SP super profiles and if we still see broad and narrow components, that will indicate that they are indeed intrinsic.

As has been done previously for the original super profiles we quantify the quality of the one and two-component Gaussian fits by comparing their χ^2 values. Our results show that the SP super profiles are well fitted by two Gaussian components. This convincingly shows that the narrow and broad components are intrinsic. We also take only the wingless sides of LHAP and RHAP super profiles and fit them both with single and double Gaussian components. Also in this case, the two-component fits are still better than the single ones.

We compare the velocity dispersions from SP super profiles to those from the wingless sides of LHAP and RHAP super profiles in Figure 4.7. To do this, we simply mirror the wingless side of the LHAP and RHAP super profiles and fit the resulting super profiles with double Gaussian components. The broad component velocity dispersions derived from the wingless side of the LHAP and RHAP super profiles tend to be smaller than those derived from the SP super profiles. However, there is no major difference between the narrow component velocity dispersions derived from the wingless side of LHAP and RHAP super profiles and those from SP super profiles; as Figure 4.7 shows, the data points scatter around the line of equality. The measurements of the narrow component velocity dispersion are thus more robust than those of the broad component. The velocity dispersions from SP super profiles are summarized in Table 4.2 for the clean sample defined in section 3.6.2. In the following, we will only analyze the SP super profiles of the clean sample (assuming the -2,2 km s^{-1} definition).

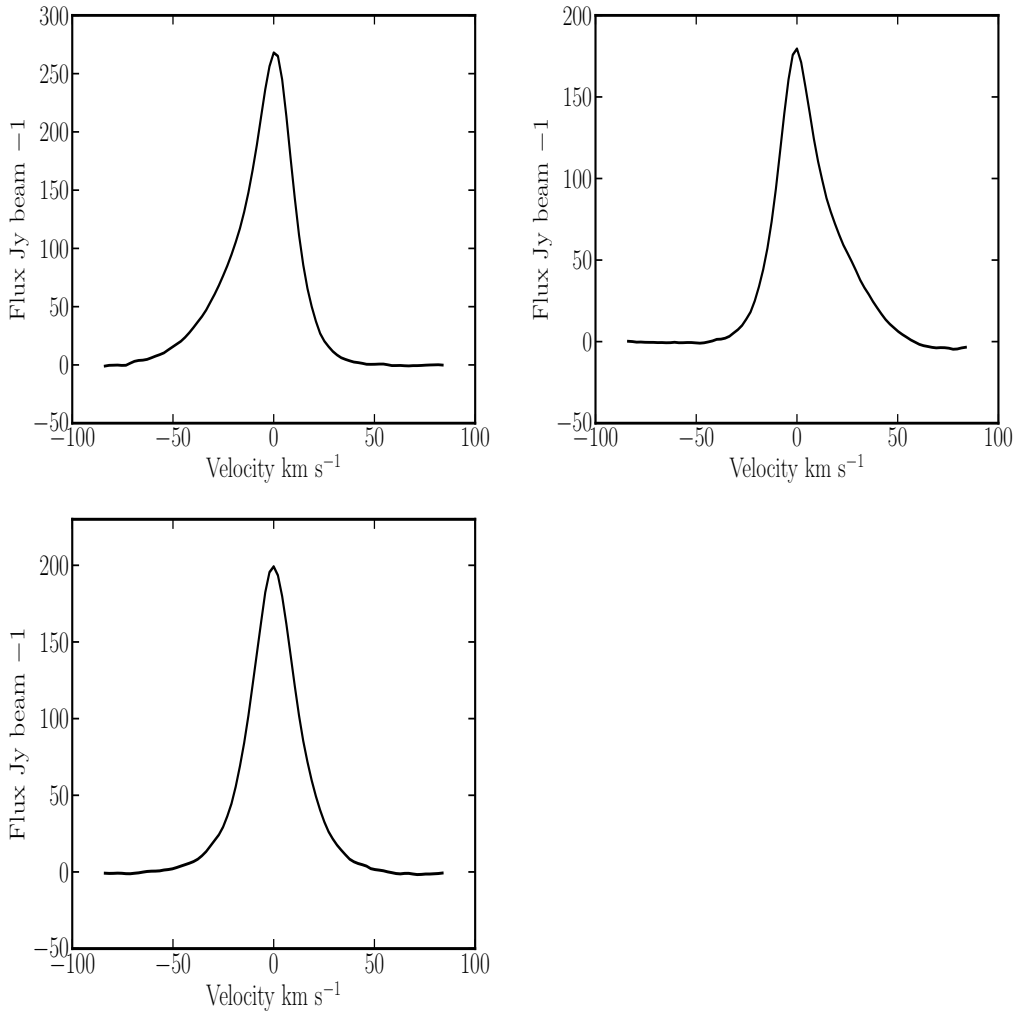

Figure 4.5: Examples of super profiles of NGC 2366 using LHAP (top left panel), RHAP (top right panel) and SP (bottom panel).

Table 4.2: Fitted parameters and properties of the clean sample

Galaxy	σ_{1g} [kms^{-1}]	σ_n [kms^{-1}]	σ_b [kms^{-1}]	χ^2_{2G}/χ^2_{1G} [kms^{-1}]
1	2	3	4	5
DDO 53	9.7 ± 0.1	6.0 ± 0.1	13.4 ± 0.2	0.00
DDO 154	9.6 ± 0.1	6.3 ± 0.1	12.9 ± 0.2	0.00
Ho I	8.9 ± 0.1	5.5± 0.1	12.5 ± 0.2	0.02
Ho II	8.9 ± 0.1	5.0 ± 0.1	11.8 ± 0.2	0.00
IC 2574	9.8 ± 0.2	5.7 ± 0.2	13.6 ± 0.3	0.10
M81 dwA	8.2 ± 0.1	3.5± 0.1	10.2 ± 0.2	0.01
NGC 628	8.1 ± 0.1	3.7 ± 0.3	9.6 ± 0.2	0.03
NGC 925	12.6 ± 0.2	9.1± 0.2	22.1± 0.8	0.02
NGC 2366	12.2 ± 0.2	8.2± 0.1	17.8 ± 0.3	0.00
NGC 2403	10.2 ± 0.2	6.1± 0.4	14.2 ± 0.7	0.30
NGC 2903	12.6 ±0.3	8.4 ± 0.2	24.9 ± 0.7	0.00
NGC 2976	11.9 ±0.2	8.6 ± 0.1	20.0 ± 0.4	0.00
NGC 3184	10.4 ± 0.3	5.9± 0.1	18.1 ± 0.2	0.00
NGC 3198	13.1 ± 0.2	8.5± 0.1	19.9± 0.3	0.07
NGC 3351	9.9 ± 0.2	7.0± 0.1	21.9 ± 0.7	0.02
NGC 3621	11.3 ± 0.2	7.5± 0.2	18.5 ± 0.7	0.16
NGC 4214	8.3± 0.1	4.2± 0.1	10.9 ± 0.1	0.25
NGC 4736	10.0 ±0.2	7.2± 0.1	20.7 ± 0.7	0.03
NGC 5055	13.3± 0.3	7.9± 0.1	21.3 ± 0.7	0.17
NGC 5236	10.5 ± 0.2	5.1± 0.4	13.8 ± 0.5	0.33
NGC 6946	9.7 ±0.5	6.0± 0.4	18.6 ± 0.1	0.36
NGC 7793	10.4 ±0.2	6.7± 0.1	17.2± 0.2	0.21

Column 1: Name of galaxies; Column 2: Velocity dispersions derived from the one component Gaussian fit; Column 3: Velocity dispersions of the narrow component; Column 4: Velocity dispersions of the broad component; Column 5: Ratio of the χ^2 values from the single and double Gaussian fitting.

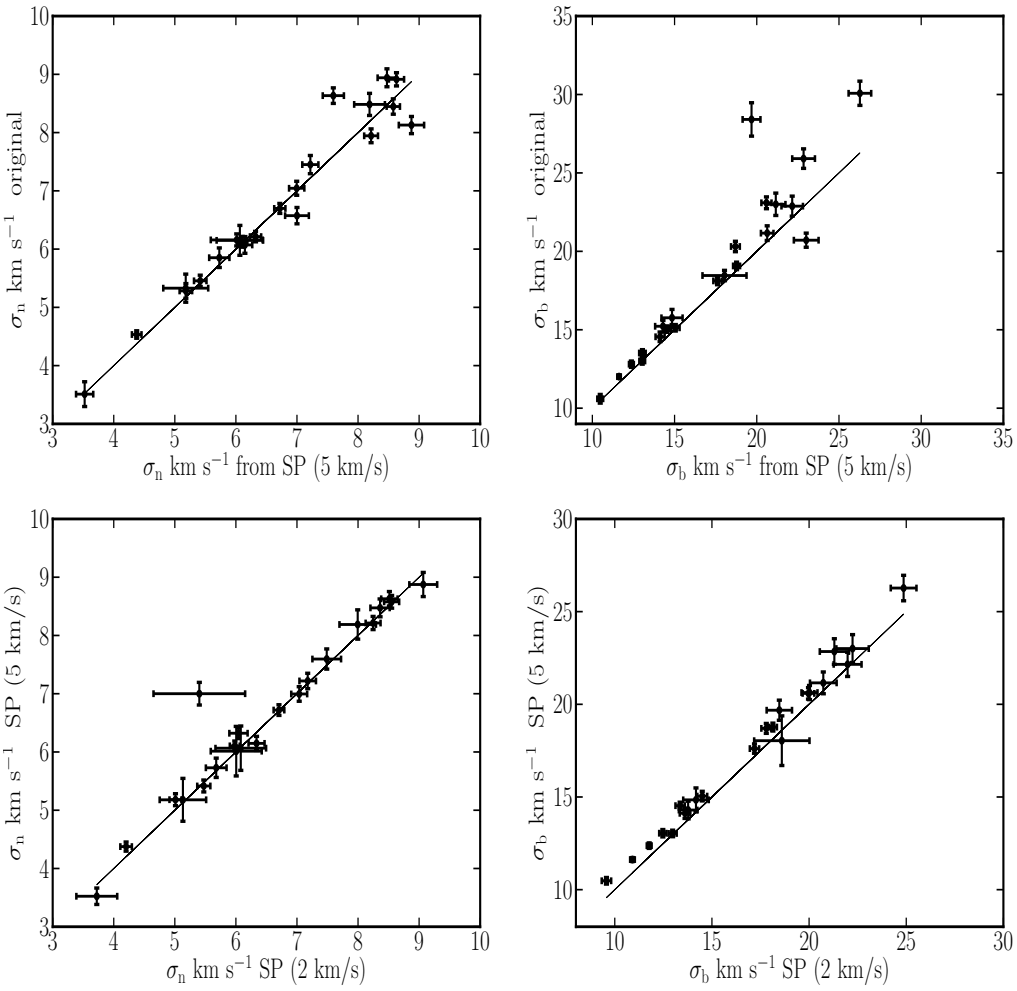

Figure 4.6: *Top panel*: Comparison of the velocity dispersions of the original super profiles (with input asymmetric and symmetric profiles) to the velocity dispersions derived from SP profiles using the -5 to 5 km s^{-1} limit. *Bottom panel*: Comparison of the velocity dispersions derived from SP profiles using the -5 to 5 km s^{-1} limit to those derived from SP profiles using the -2 to 2 km s^{-1} limit. Solid lines are lines of equality.

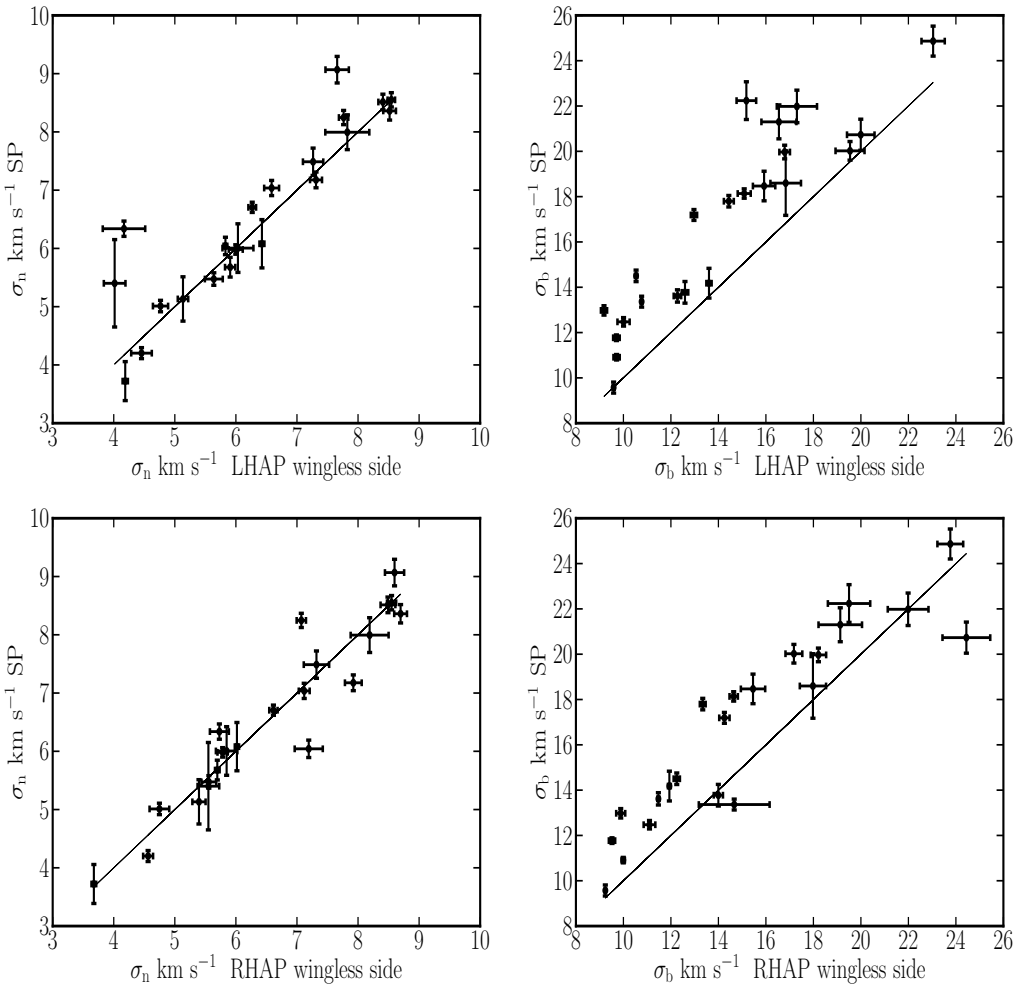

Figure 4.7: Comparison of the velocity dispersions derived from SP profiles to those derived from the wingless sides of LHAP (top panel) and RHAP (bottom panel) profiles. Here we use the -2 to 2 km s^{-1} limit. Solid lines are lines of equality.

5

SUPER PROFILES AND PROPERTIES OF GALAXIES

Since we now have a clean sample with super profiles unaffected by interaction, counter rotation and asymmetry and have checked all the relevant systematic effects which may influence the measurement of the velocity dispersions, we will now explore the shapes of the super profiles of our clean sample in detail and see if we can relate these shapes to various properties of galaxies. We begin by analyzing super profile shapes as a function of their location within the galaxies. For this, we first investigate the properties of the shapes of the profiles inside and outside the optical radius r_{25}. Then we expand our analysis by analyzing super profile shapes within annuli of radius $0<r<0.2\ r_{25}$, $0.2<r<0.4\ r_{25}$, etc. In this way, we create what we call radial super profiles. We also analyze the shapes of the super profiles as a function of the star formation activity of the galaxies. For this, we use the SFR map derived by Leroy et al. (2008) to locate different star formation regions within a galaxy and classify them as low medium and high SFR regions according to their SFR values. We then compare the shapes of the super profiles in these three regions to see if there is any relation between profile shapes and star formation activity of a galaxy.

5.1 Profile shapes and location within the galaxy

5.1.1 Super profiles inside and outside the optical radius r_{25}

Here we investigate whether there is any relation between the shapes of the profiles and their location within the galaxy. We aim to explore the mechanisms that determine the shapes of the profiles. We study the shapes of the super profiles within r_{25}, which is usually a site of active star formation, and outside r_{25}, a region where we do not expect to see much star formation.

We compare in Figure 5.1 (top panel) the velocity dispersions derived from the super profiles of the clean sample inside and outside r_{25}. Here we use the 2 km s^{-1} limit to select symmetrical profiles as we still have sufficient S/N while applying this limit. The left panel is for the narrow component, whereas the right panel is for the broad component. The solid lines are lines of equality. From this Figure, it is clear that super profiles within r_{25} tend to be broader than those outside r_{25}. Figure 5.1 (bottom left panel) compares the ratio of the area under the narrow component profiles to that under the broad component profiles, which represents the mass ratio of the narrow component to that of the broad component, inside and outside r_{25}. We find that the mass ratio of the narrow component to that of the broad component tends to be higher inside than outside r_{25}. For dwarf galaxies, the mean value of the mass ratio is $\sim 0.6\pm0.2$ inside r_{25}. Outside r_{25}, the mass ratio is $\sim 0.4\pm0.2$. For spiral galaxies, the mass ratio has a mean value of $\sim 0.7\pm0.3$ and $\sim 0.6\pm0.4$ inside and outside r_{25}, respectively. Note that here we adopt the definition of spirals and dwarfs by Leroy et al. (2008). They define as dwarf galaxies those with rotation velocities $v_{rot} \lesssim 125$ km s^{-1}, stellar masses $M_* \lesssim 10^{10}$ M$_\odot$, and absolute B magnitude $M_B \gtrsim$ -20 mag; and as spiral galaxies those with $v_{rot} \gtrsim 125$ km s^{-1}, $M_* \gtrsim 10^{10}$ M$_\odot$ and $M_B \lesssim$ -20 mag.

We use the overall super profiles (symmetric + asymmetric profiles) to estimate the degree of asymmetry, which we define as the offset between the peak velocity of the narrow component and the peak velocity of the broad component, of the super profiles inside and outside r_{25}. Here we are interested in where the asymmetric profiles are mostly found. We find that super profiles inside r_{25} tend to be more asymmetric than those outside r_{25}. This is illustrated in the bottom right panel of Figure 5.1. The solid lines are lines

of equality. We present the fitted parameters from the super profiles of the clean sample inside and outside r_{25} in Table 5.1.

5.1.2 Radial super profiles for the clean sample

We derive radial super profiles for the clean sample by dividing the galaxies into series of annuli with 0.2 r_{25} width. We then derive super profiles in each annulus and then decompose them into Gaussian components. For two galaxies (DDO 53 and M81 dwA) we use a spacing of 0.4 r_{25} to increase the S/N. Here we use the SP mask where the difference between the HER3 and the IWM velocity field is between -5 and 5 km s^{-1} instead of the -2 to 2 km s^{-1} definition for a better S/N. We want to investigate whether the fitted parameters (velocity dispersions, area under the broad and narrow components) vary as a function of radius. If we find such variations, we aim to explore whether this variation is related to galaxy properties or morphology.

Velocity dispersions vs radius

Figure 5.2 represents plots of velocity dispersions against radius. Among the 22 derived radial velocity dispersion profiles, 16 ($\sim$ 70 %) show a clear trend with radius. We observe the following characteristics for the radial velocity dispersion profiles:

I. For NGC 628 and NGC 2403, the velocity dispersions decline monotonically from the center to the outermost observed radius. For NGC 628, an almost face on spiral galaxy, the narrow component velocity dispersion goes from 6.8 km s^{-1} down to 2.5 km s^{-1}. Its broad component velocity dispersion goes from 22.2 km s^{-1} down to 6.9 km s^{-1}. For NGC 2403, an SABc galaxy, the velocity dispersion goes from 9.5 to 3.7 km s^{-1}, and from 26.3 km s^{-1} down to 8.8 km s^{-1} for the narrow and broad components, respectively.

II. For NGC 3621, NGC 4736, NGC 5055, NGC 2903 and NGC 3198, the velocity dispersions show a radial decline up to $\sim r_{25}$ and then tend to flatten. For NGC 3198, the velocity dispersions tend to decrease toward the center.

III. For NGC 925, NGC 7793, IC 2574 and NGC 5236, the velocity dispersions decrease from the center up to a certain radius, then increase and

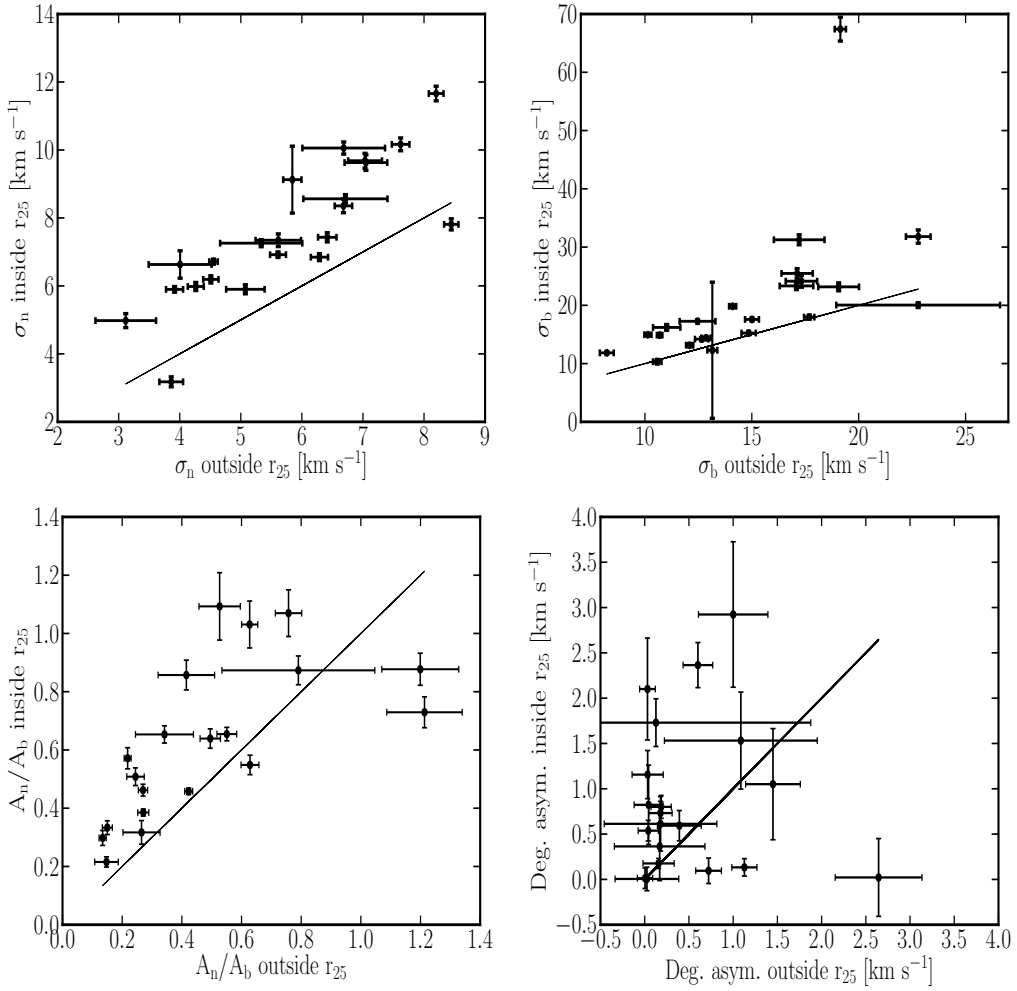

Figure 5.1: *Top panel*: Comparison of the derived velocity dispersions inside and outside r_{25}. The left panel is for the narrow component, whereas the right panel is for the broad component. *Bottom panel*: Comparison of the mass ratio of the narrow to that of the broad component inside and outside r_{25} (left panel). The right panel compares the degree of asymmetry (defined as the offset between the peak velocity of the narrow component and the peak velocity of the broad component) of the super profiles inside and outside r_{25}. The solid lines are lines of equality.

Table 5.1: Fitted parameters from the super profiles inside and outside r_{25}

	Fitted parameters							
	inside r_{25}				outside r_{25}			
GALAXY	σ_n	σ_b	deg. asym.	A_n/A_b	σ_n	σ_b	deg. asym.	A_n/A_b
	[kms^{-1}]	[kms^{-1}]	[kms^{-1}]		[kms^{-1}]	[kms^{-1}]	[kms^{-1}]	
1	2	3	4	5	6	7	8	9
DDO 53	9.1±1.0	12.3±11.7	2.1±0.6	4.23±9.15	5.8±0.1	13.2±0.2	0.0±0.1	0.39±0.03
DDO 154	6.8±0.1	14.4±0.2	0.5±0.1	0.64±0.03	6.3±0.1	12.9±0.2	0.0±0.1	0.50±0.03
Ho I	6.0±0.1	13.2±0.3	0.1±0.1	0.57±0.04	4.3±0.1	12.1±0.2	1.1±0.1	0.22±0.01
Ho II	6.2±0.1	14.9±0.2	0.7±0.1	0.46±0.02	4.5±0.1	10.7±0.1	0.2±0.1	0.27±0.02
IC 2574	5.9±0.1	14.2±0.3	0.6±0.2	0.51±0.03	5.1±0.3	12.7±0.3	0.4±0.2	0.24±0.03
M81 DwA	3.2±0.2	10.3±0.4	1.2±0.3	0.30±0.03	3.9±0.2	10.6±0.2	0.0±0.2	0.13±0.01
NGC 628	5.0±0.2	11.8±0.2	0.0±0.1	0.22±0.02	3.1±0.5	8.2±0.3	0.0±0.4	0.15±0.04
NGC 925	9.6±0.2	24.1±1.0	0.0±0.4	1.09±0.12	7.0±0.3	17.3±0.7	2.6±0.5	0.53±0.07
NGC 2366	7.8±0.6	18.0±0.3	2.4±0.2	0.55±0.03	8.4±0.1	17.7±0.2	0.6±0.2	0.63±0.03
NGC 2403	7.3±0.1	17.3±0.3	0.6±0.3	0.65±0.03	5.3±0.7	12.5±0.8	0.2±0.6	0.34±0.10
NGC 2903	10.2±0.2	31.8±1.1	2.9±0.8	1.07±0.08	7.6±0.1	22.8±0.6	1.0±0.4	0.76±0.04
NGC 2976	8.6±0.1	20.0±0.4	1.7±0.3	0.87±0.05	6.7±0.7	22.8±0.4	0.1±1.8	0.79±0.26
NGC 3184	6.7±0.1	19.8±0.2	0.8±0.1	0.46±0.01	4.6±0.1	14.1±0.2	0.2±0.1	0.42±0.01
NGC 3198	11.7±0.2	67.4±2.0	0.8±0.4	1.03±0.08	8.2±0.1	19.1±0.3	0.0±0.2	0.63±0.03
NGC 3351	7.4±0.1	23.2±0.7	0.4±0.4	0.88±0.06	6.4±0.2	19.1±1.0	0.2±0.5	1.20±0.13
NGC 3621	9.7±0.2	23.3±0.6	1.7±0.6	0.75±0.06	7.0±0.3	17.1±0.8	5.9±1.0	0.73±0.10
NGC 4214	5.9±0.1	14.9±0.1	0.0±0.1	0.39±0.01	3.9±0.1	10.1±0.2	0.0±0.1	0.27±0.02
NGC 4736	8.4±0.2	25.5±0.8	1.1±0.6	0.73±0.05	6.7±0.1	17.1±0.7	1.5±0.3	1.21±0.13
NGC 5055	10.1±0.2	31.3±0.9	1.5±0.5	0.86±0.05	6.7±0.7	17.2±1.2	1.1±0.9	0.42±0.10
NGC 5236	6.6±0.4	16.2±0.5	0.2±0.1	0.32±0.04	4.0±0.5	11.0±0.6	0.2±0.2	0.26±0.06
NGC 7793	6.9±0.1	17.6±0.2	0.1±0.1	0.65±0.02	5.6±0.1	15.0±0.3	0.7±0.1	0.55±0.03

1: Name of galaxies; 2: Narrow components velocity dispersions derived from the super profiles inside r_{25}; 3: Broad components velocity dispersions derived from the super profiles inside r_{25}; 4: Degree of asymmetry of the super profiles inside r_{25}; 5: Ratio of the area of the narrow component to that of the broad component inside r_{25}; 6: Narrow components velocity dispersions derived from the super profiles outside r_{25}; 7: Broad components velocity dispersions derived from the from the super profiles outside r_{25}; 8: Degree of asymmetry of the super profiles outside r_{25}; 9: Ratio of the area of the narrow component to that of the broad component outside r_{25}.

continuously decline up to the outermost detectable radius. Note that for NGC 5236, there is a tendency for the velocity dispersions to decline toward the center.

IV. For NGC 3184, NGC 3351, NGC 4214 and Ho II, the velocity dispersions increase from the center up to a certain radius and then decrease up to the outermost observed radius. Note that NGC 3184 and NGC 3351 have HI holes in their center which may explain their decrease in velocity dispersions toward their center.

V. For HoI, DDO53, NGC 2366, M81 DwA, NGC 2976, M81 DwB, there is no obvious trend between velocity dispersions and radius. Note that for HoI, even though the trend is less prominent, the radial profile tends to decrease with radius. Similarly for DDO53, there is a slight tendency of the radial velocity dispersion profile to rise up to roughly the optical radius and then decreases with increasing radius.

VI. For DDO 154, a particular case is observed where the velocity dispersion hardly changes up to about $6r_{25}$ and then declines.

Mass ratio of the narrow and broad components vs radius

Here we investigate the radial dependence of the mass ratio of the narrow component to that of the broad component as a function of radius. Here we also use the SP super profiles using the [-5,5] km s^{-1} limit. The mass ratio is defined as the ratio between the area under the narrow and broad components curve extracted from the super profiles in each annulus. Figure 5.3 is a plot of the mass ratio as a function of radius with dwarfs and spirals plotted separately. Here, like in the previous section, we also adopt the definition of dwarfs and spirals by Leroy et al. (2008). In general, the mass ratio tends to be lower for dwarfs than for spirals. Some galaxies show a radial decline in the mass ratio whereas others do not. For NGC 2403, the mass ratio stays almost constant up to $\sim r_{25}$, then a sudden decrease in the ratio occurs just beyond the optical radius; the ratio then stays relatively constant out to the outermost radius. The mass ratio of NGC 4214 and NGC 2903 show similar trends with radius. For these galaxies, except in their innermost part, the mass ratio decreases approximately linearly with increasing radius. For illustration, we show, in the middle and bottom panel

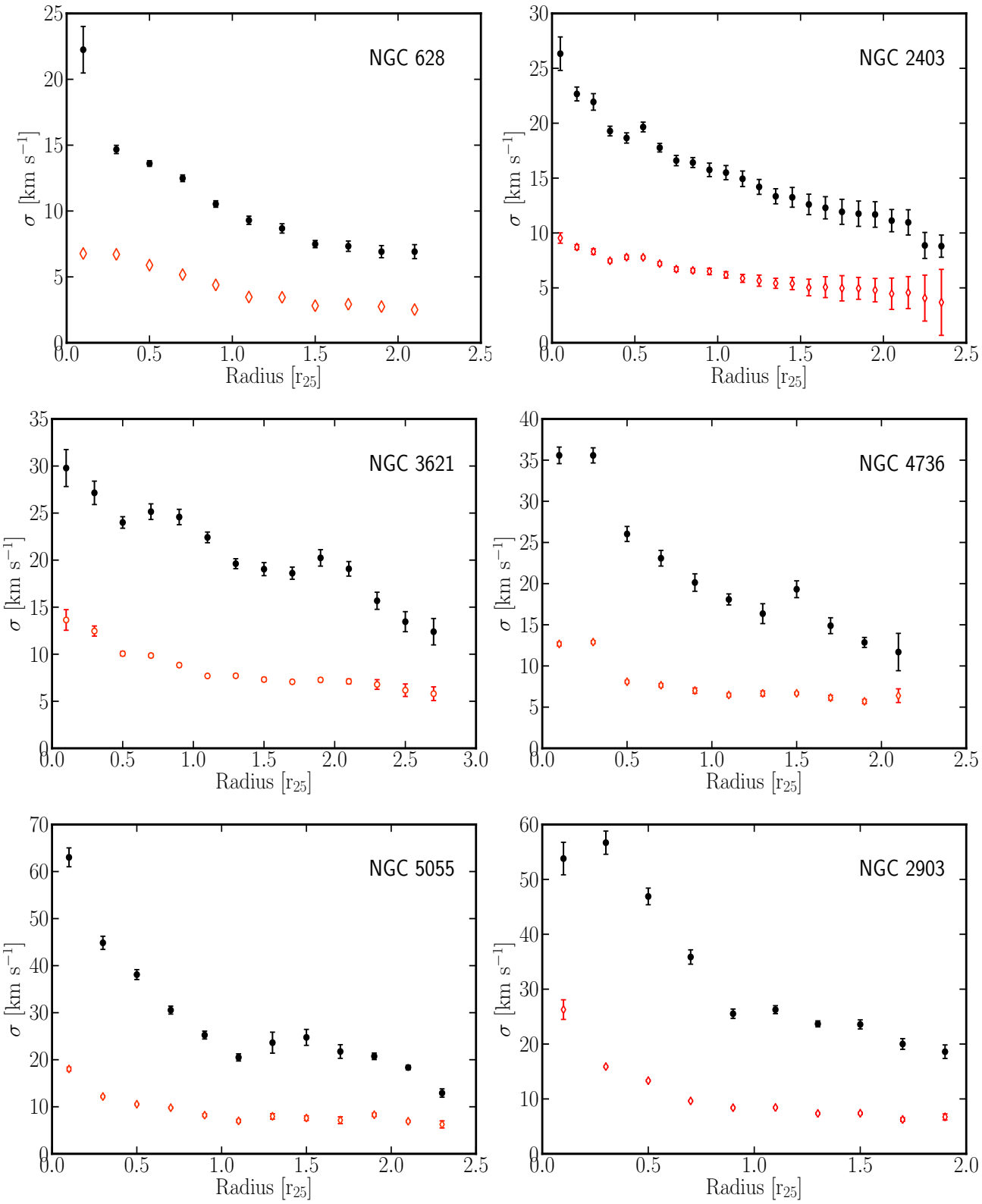

Figure 5.2: Radial velocity dispersion profiles of the Clean sample. Filled black symbols represent the broad component. Red open symbols represent the narrow component. The radius is in units of r_{25}.

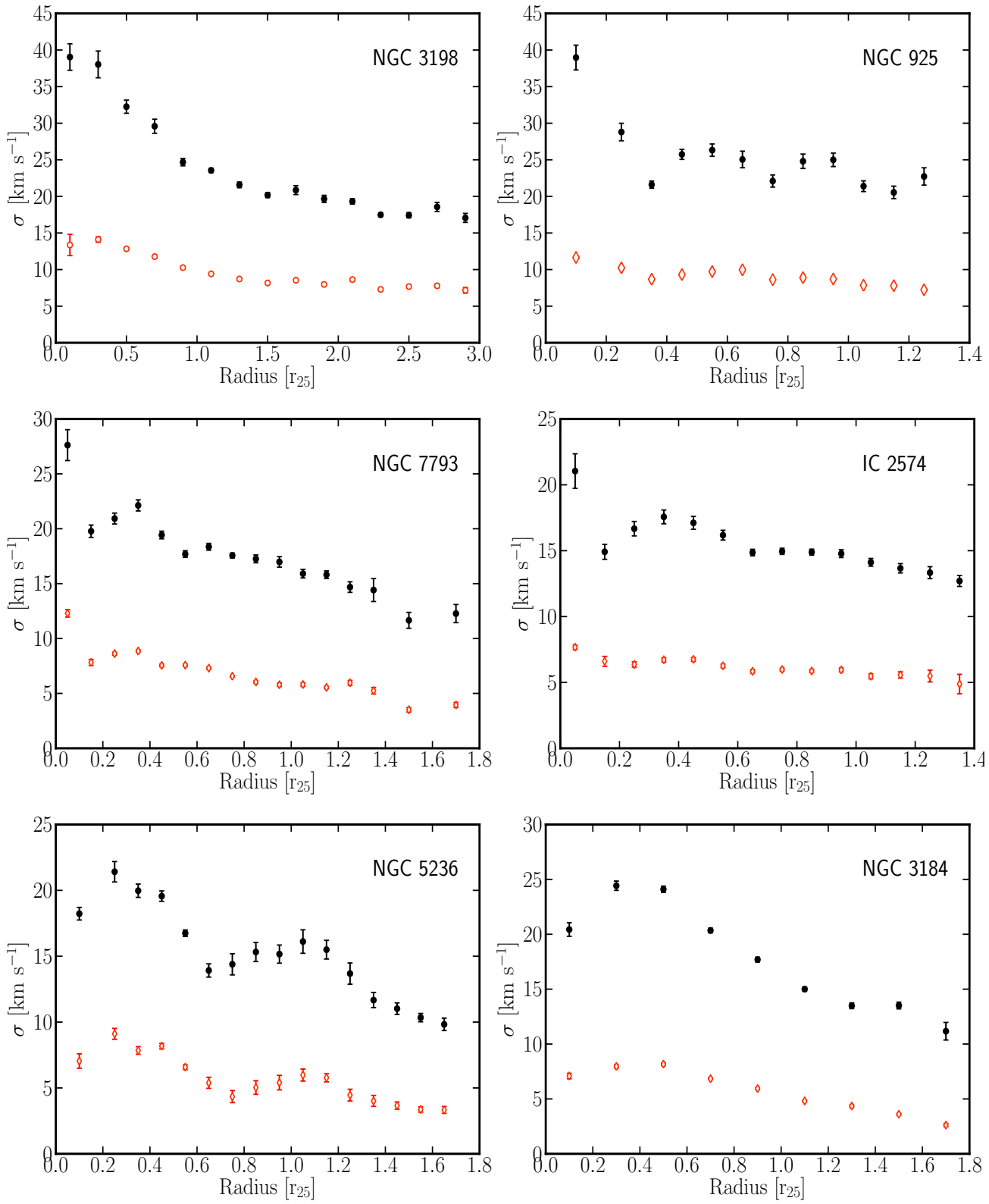

Figure 5.2 (continued).

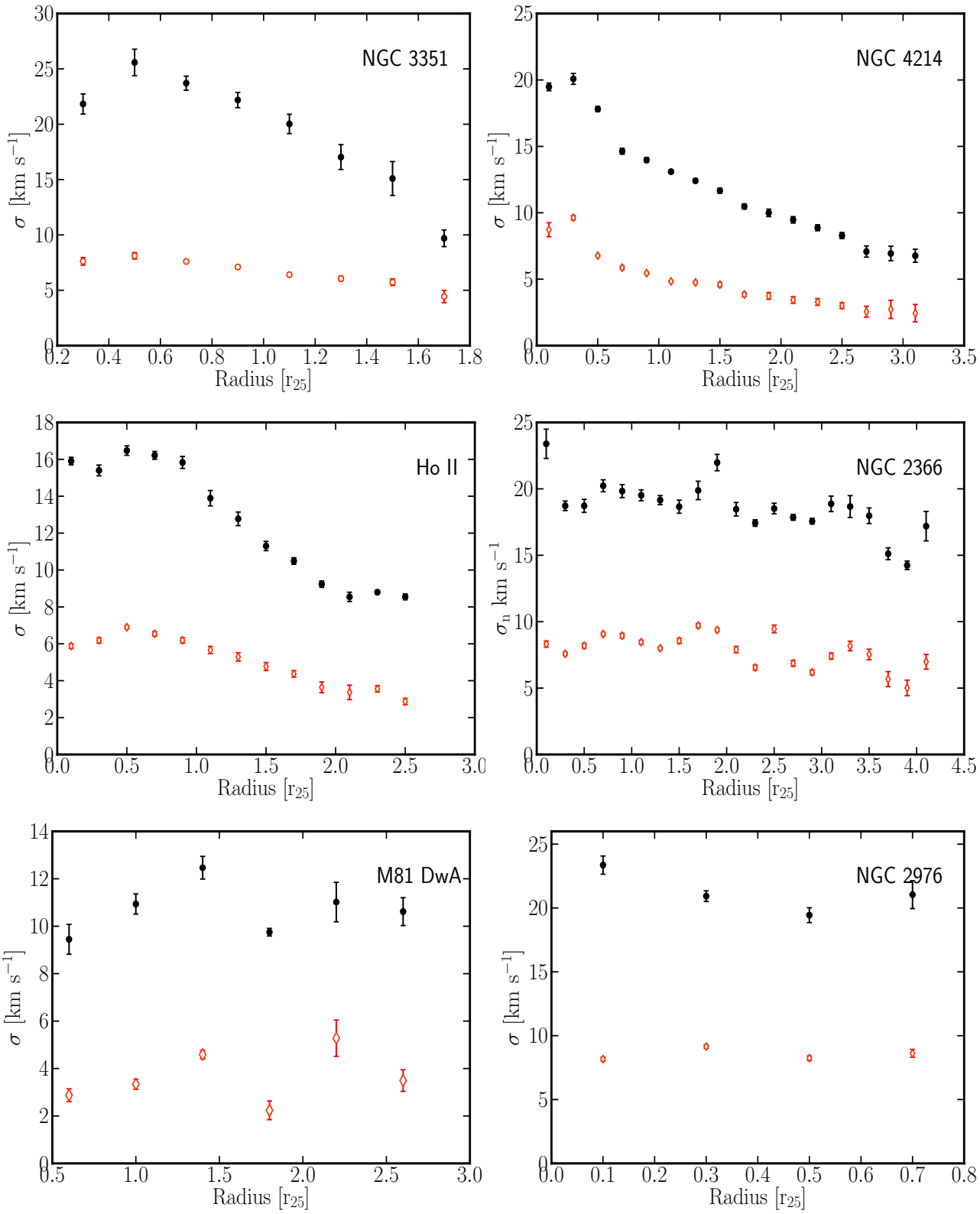

Figure 5.2 (continued).

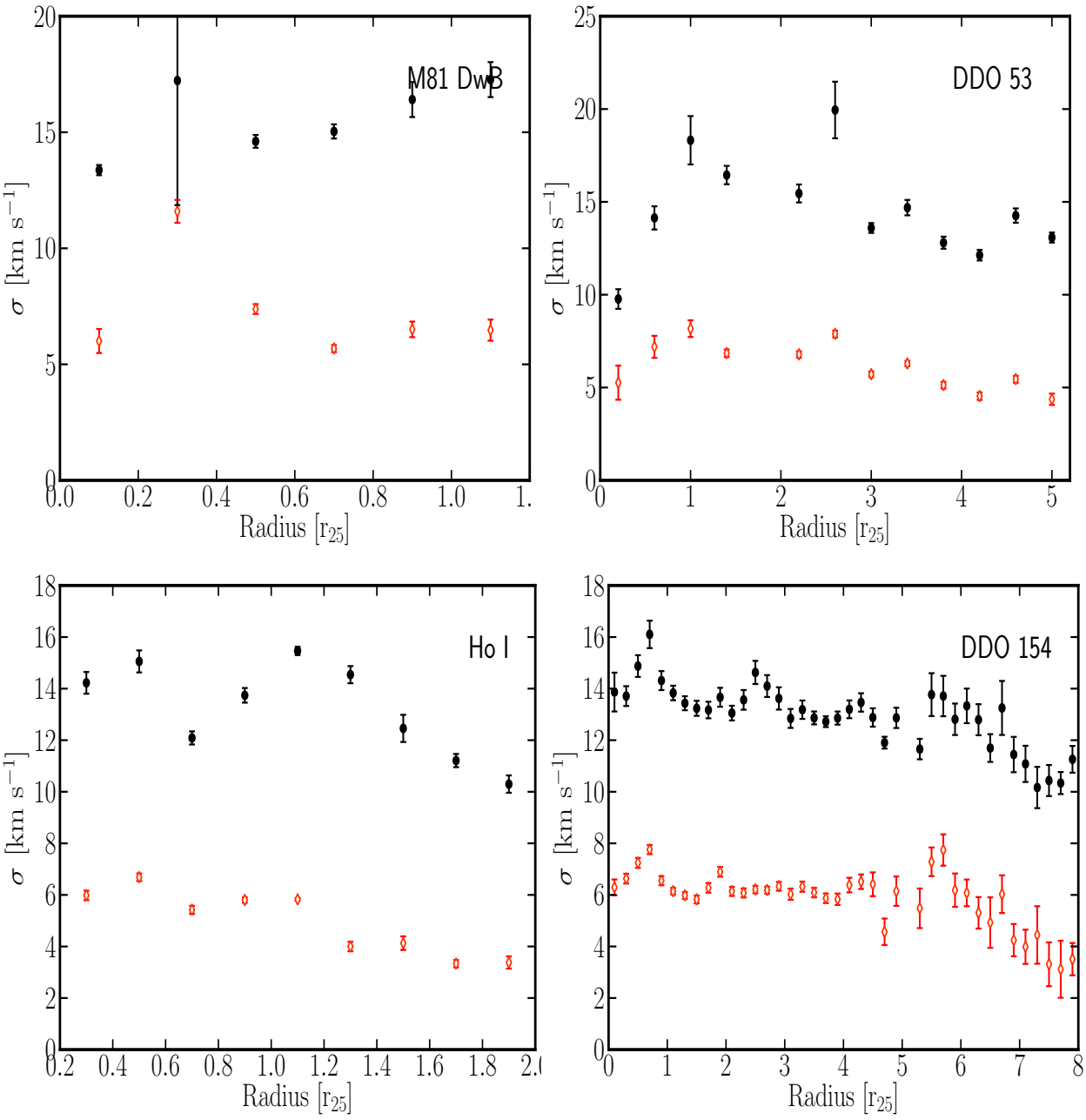

Figure 5.2 (continued).

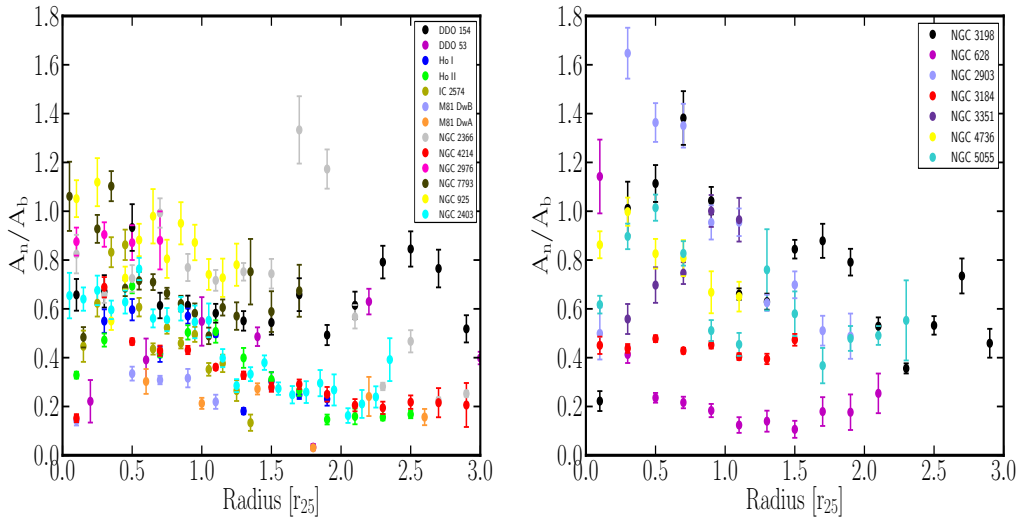

Figure 5.3: Mass ratio of the narrow component to that of the broad component as a function of radius. The radius is in units of r_{25}. The left panel is for dwarf galaxies according to Leroy et al.'s (2008) definition. The right panel is for spiral galaxies adopting the definition from Leroy et al. (2008).

of Figure 5.3, the mass ratio of the narrow to that of the broad component as a function of radius for these three galaxies.

5.2 Profile shapes and star formation activity of galaxies

We use the star formation rate surface density Σ_{SFR} maps derived by Leroy et al. (2008) to locate the sites of low, moderate and high star formation rates within our sample. We study the behaviour of the super profiles in these different regions to check whether there is any relationship between profile shapes and star formation activity of galaxies. We derive super profiles in the three regions mentioned above (with only symmetrical input profiles selected by the SP mask using the [-5,5] km s^{-1} limits), fit them with double gaussian components and compare the fitted parameters (velocity dispersions, mass ratio of the narrow and broad components, degree of asymmetry) to check whether these parameters vary as a function of the Σ_{SFR} value of galaxies.

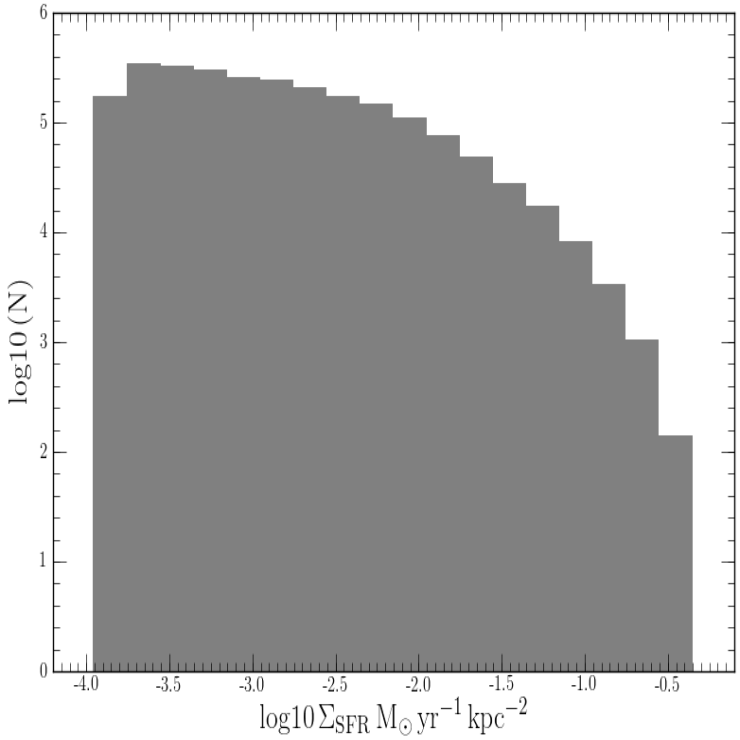

Figure 5.4: Histogram of all the pixel values from the star formation surface density maps of the THINGS galaxies as derived by Leroy et al. (2009). Only those pixels above the limiting sensitivity value $\log\Sigma_{SFR} = 10^{-4}$ $M_\odot$ yr^{-1} kpc^{-2} are plotted here. We classify as low SFR regions, those with $\log\Sigma_{SFR} = 10^{-4}$ to 10^{-3} $M_\odot$ yr^{-1} kpc^{-2} and as moderate SFR regions, those with $\log\Sigma_{SFR} = 10^{-3}$ to 10^{-2} $M_\odot$ yr^{-1} kpc^{-2}. Regions having $\log\Sigma_{SFR}$ value higher than 10^{-2} are classified as high SFR regions.

Figure 5.4 is a histogram of all the pixel values from each star formation maps of the 34 THINGS sample galaxies. Note that the Σ_{SFR} maps have a limiting sensitivity of about 10^{-4} $M_\odot$ yr^{-1} kpc^{-2} and therefore we only retain Σ_{SFR} higher than this value. From this histogram, regions having Σ_{SFR} values between 10^{-4} and 10^{-3} , $10^{-3}$and 10^{-2}, 10^{-2} and higher, all in units of $M_\odot$ yr^{-1} kpc^{-2}, are classified as low, medium and high SFR regions, respectively. We study the shapes of the super profiles in these three regions and we find similar results as found from the analysis of the shapes of the super profiles inside and outside r_{25}.
By comparing the panels in Figure 5.5, one can see that both the broad and narrow components tend to be broader in the high SFR regions than in the

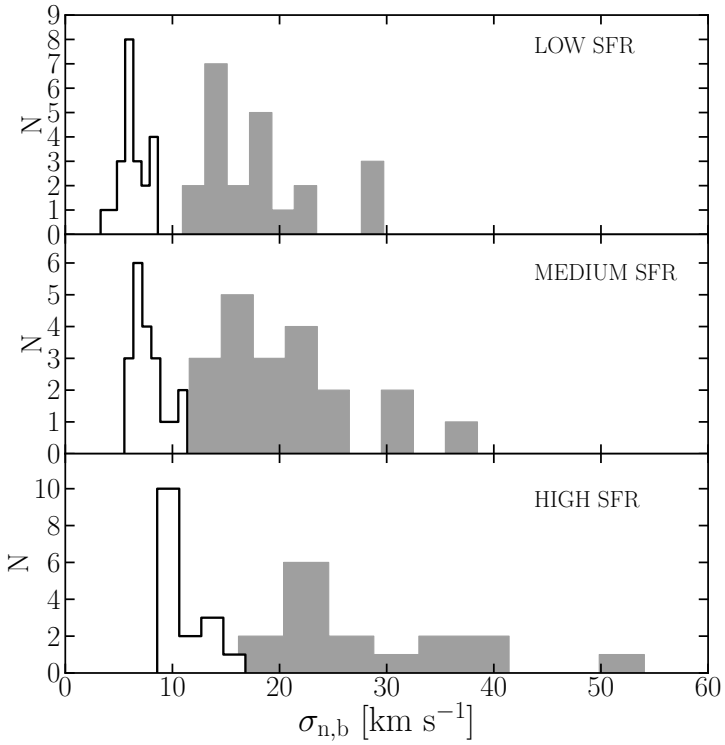

Figure 5.5: Histograms of the velocity dispersion of the narrow (solid histograms) and broad (gray histograms) components derived in low, medium and high SFR regions. The velocity dispersions tend to be higher in high SFR regions.

medium and low SFR regions. Moreover, the first three panels of Figure 5.6 show that super profiles in the high SFR regions tend to be more asymmetric than those in the medium and low SFR regions. Finally, as can be seen from the last three panels of Figure 5.6, the mass ratio of the narrow component to that of the broad component is higher in the high SFR regions than in the medium and low SFR regions. Thus, there seems to be a correlation between the shapes of the super profiles and the star formation activity of galaxies.

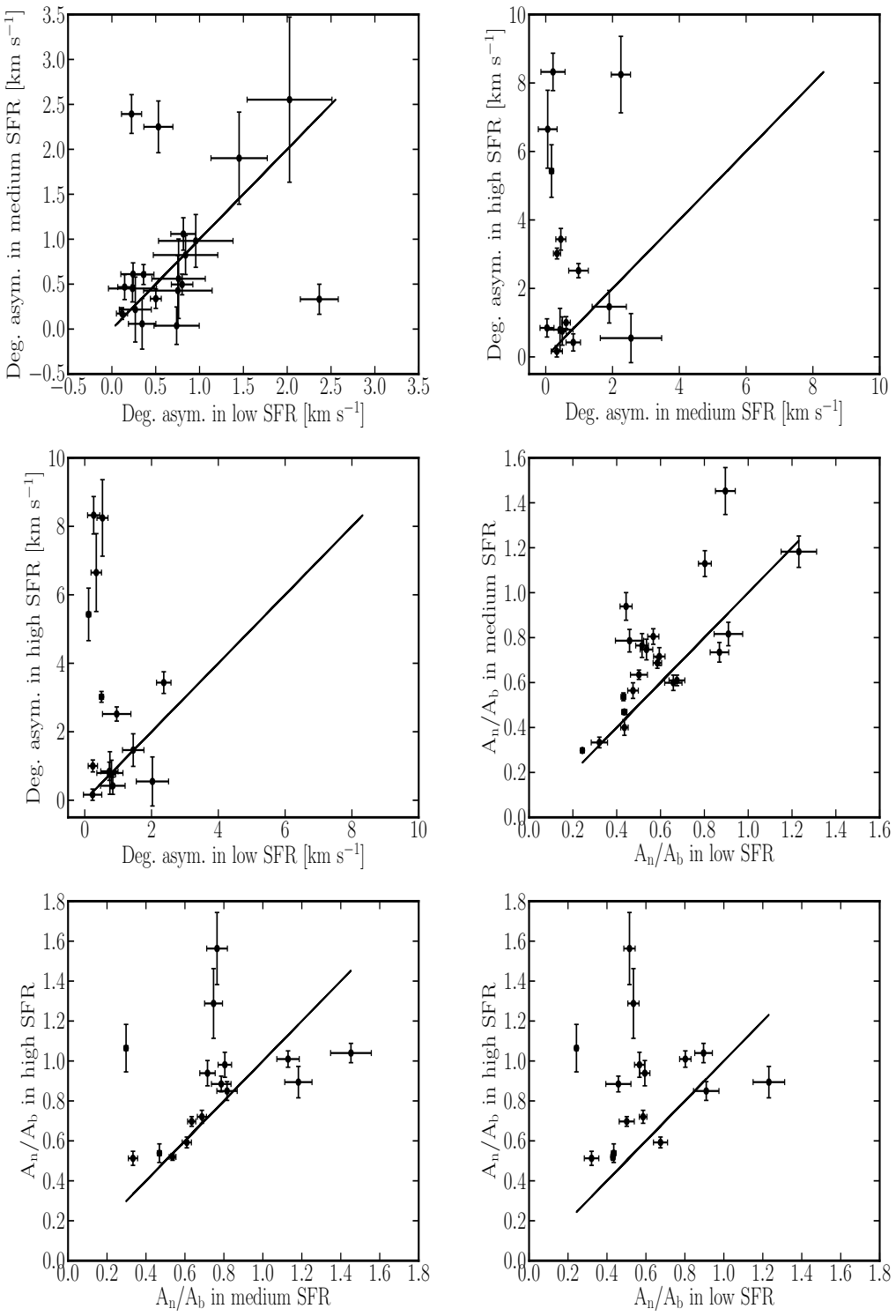

Figure 5.6: Comparison of the degree of asymmetry (offset between the peak velocity of the narrow and broad components) of the super profiles as well as the mass ratio of the narrow component to that of the broad component (labelled as A_n/A_b) in low, medium and high SFR regions. The degree of asymmetry and the mass ratio tend to be higher in high SFR regions. The solid lines are lines of equality.

6 DISCUSSION

6.1 Super profiles and the energy sources of the ISM

Our analysis of super profile shapes suggest that star formation is an important energy source of the ISM. This is supported by two facts: (1) The width of the super profiles tends to be larger inside r_{25} and in the high SFR regions defined earlier. (2) The super profiles tend to be more asymmetric inside r_{25} and in the high SFR regions mentioned earlier. Thus, stellar related energy sources must be the dominant mechanisms that sustain the width of a profile in active star formation regions. This confirms the conclusion drawn by Tamburro et al. (2009) who investigated the most plausible dominant mechanisms that broaden line widths based on second-moment map analyses of the THINGS galaxies. Among the various stellar feedback mechanisms, which include stellar winds, ionizing radiation from young massive stars, expanding HII regions and Supernova explosions (SNe), the latter are known to be the most important contributor to the energy budget of the ISM (Spitzer, 1978; Norman and Ferrara, 1996; Mac Low and Klessen, 2004; Melioli and de Gouveia Dal Pino, 2004). All of these various mechanisms are believed to drive turbulence in the ISM (e.g. Dickey and Lockman, 1990; Elmegreen and Scalo, 2004). This can explain the high velocity dispersion values that we see inside r_{25} and in the high SFR regions mentioned earlier. As discussed in Tamburro et al. (2009), a velocity dispersion higher than ~ 8 km s^{-1} cannot be explained by thermal motions of hydrogen atoms only. In fact, the temperature of the WNM ranges from about 4000 K to

8000 K (Walterbos and Braun, 1996), which gives a velocity dispersion ranging from about 6 to 8 km s^{-1}. Therefore, a velocity dispersion higher than $\sim$ 8 km s^{-1} is not entirely thermal but must also have a turbulent origin. The temperature expected from the CNM is somewhere between 40 to 200K (Walterbos and Braun, 1996), which gives a thermal velocity dispersion of $\sim$ 0.6 to 1.3 km s^{-1}. Our measured velocity dispersions are slightly higher than these expected values from the CNM and WNM even in the very outskirts of galaxies where stellar feedback is no longer expected to play a role in broadening profiles. Tamburro (2009) demonstrated that extragalactic radiation or Magneto Rotational Instability (MRI) are the dominant mechanisms that broaden the width of a profile in regions of inactive star formation.

6.2 CNM and star formation

Following Young and Lo (1996) and de Blok and Walter (2006), we associate the narrow component extracted from the super profiles with the CNM and the broad component with the WNM. The observed increase in the mass ratio of the narrow component to that of the broad component when going from inactive to active star formation areas shows the need for the presence of cold gas to initiate star formation. The mass ratio tends to be lower for dwarfs than for spirals. This may be consistent with the fact that dwarf galaxies have low star formation rates. The CNM thus tends to be associated with star formation. Theoretical models which take the phase structure of the ISM into account show that there is a critical density above which the WNM gas must cool; this will promote gravitational instability and trigger star formation (Schaye, 2004; de Blok and Walter, 2006). The observed increase in the mass ratio of the CNM to WNM from inactive to active star formation that we found supports this idea. Young and Lo (1996, 1997), Young et al. (2003), de Blok and Walter (2006) found that the CNM tends to be located near star forming regions. This also seems to be the case in our sample. We, however, still find narrow component in low SFR regions and in regions where we expect to see no star formation at all (i.e regions well beyond r_{25}). This is similar to previous findings by Young et al. (2003). The latter authors found ample amounts of CNM in regions of little or no star formation. Young et al. (2003) suggested that there might be a time delay between the formation of a cold phase and star formation.

6.3 Velocity dispersion: comparison with previous works

We have found a much wider range in velocity dispersions than was previously found for dwarf galaxies. Young and Lo (1996a, 1997), Young et al. (2003) found narrow component velocities ranging from about 3 to 5 km s^{-1} and broad component velocity dispersions of 8 to 12 km s^{-1} in a sample of five dwarf galaxies. de Blok and Walter (2006) found narrow component with a mean velocity dispersion of $\sim$ 4 km s^{-1} and broad component with a mean velocity dispersion of $\sim$ 8 km s^{-1} for NGC 628, a dwarf galaxy of the Local Group. In our clean sample, if we exclude spiral galaxies, the velocity dispersion of the narrow component range from $\sim$ 3 to 8 km s^{-1}, whereas that of the broad component range from 10 to 18 km s^{-1}. This difference could be attributed to the fact that we have a much larger range in galaxy properties and thus much wider range in velocity dispersion.

Based on a second moment map analysis, Tamburro et al. (2009) derived radial velocity dispersions in some of the THINGS galaxies. They found a characteristic velocity dispersion value of 10$\pm$2 km s^{-1} at the optical radius r_{25} for all their analyzed galaxies. We also retrieve similar conclusions as Tamburro et al. (2009) from our super profile analysis. We find that at 1.0 $r_{25} < r < 1.2\ r_{25}$, the narrow and broad components velocity dispersions seem to converge to a fixed value. This value is 6.5$\pm$1.4 and 17.4$\pm$4.2 km s^{-1} for the narrow and broad components, respectively (see Figure 6.1). The value found by Tamburro et al. (2009) seems to be the average of the characteristic values that we find for the broad and narrow components at 1.0 $r_{25} < r < 1.2\ r_{25}$ within the uncertainty.

The value found by Tamburro is thus the average contribution of the CNM and the WNM velocity dispersions. For example, for NGC 628, a face-on spiral galaxy (the projection effect is insignificant for this galaxy given its low inclination of only $\sim 7^{o}$), we find a velocity dispersion of $\sim$ 2.5 km s^{-1} for the narrow component and 6.9 km s^{-1} for the broad component in the outermost radius. Tamburro (2009) found a velocity dispersion of $\sim$5 km s^{-1} in the outermost radius of NGC 628 based on a second moment map from THINGS. This value is the average value of the narrow and broad components velocity dispersion that we find in the outermost radius of NGC 628.

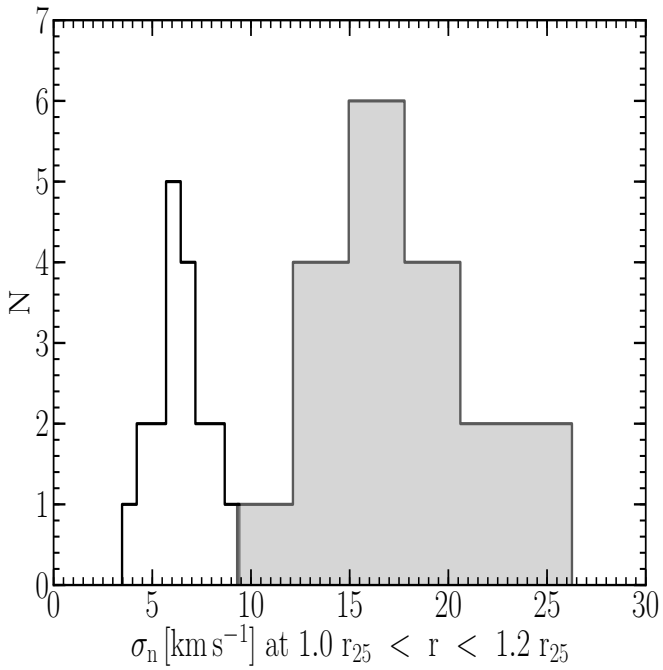

Figure 6.1: Distribution of the velocity dispersions of the narrow (*left panel*) and broad (*right panel*) components derived at $r_{25} < r < 1.2\ r_{25}$. The narrow component distribution has a mean of 6.5±1.4. The broad component distribution has a mean of 17.4±4.2.

Thus a velocity dispersion derived from a second moment map is the average contribution of the velocity dispersion of the CNM and the WNM.

7 CONCLUSION and FUTURE WORK

7.1 Conclusion

In this thesis, we have presented a method similar to the stacking method used in high redshift HI observations to construct high S/N profiles, which we call "super profiles". This is done by summing each individual profile in a data cube after shifting them to a common central velocity. We have used data from The HI Nearby Galaxy Survey (THINGS), a large HI survey of 34 nearby dwarf and spiral galaxies using the NRAO VLA telescope, to derive super profiles of all the THINGS galaxies. We have checked various systematic and non-systematic effects that may change the intrinsic shapes of the super profiles. Moreover, to avoid misleading interpretation of the shapes of the super profiles, we have identified a clean sample that is unaffected by interaction, counter rotation or other systematic effects that may change the intrinsic shapes of the HI velocity profiles.

We have analyzed the shapes of the super profiles of the clean sample in different regions (as defined by location within the galaxies and star formation rate surface density $\Sigma_{\rm SFR}$ value) of the galaxies. By decomposing the super profiles into Gaussian components, we have found broad and narrow components which are evidence of the Warm Neutral Medium (WNM) and Cold Neutral Medium (CNM) phases of the ISM. We have found some correspondence between the shapes of the profiles and their location within the galaxies. The super profiles tend to be broader and more asymmetric inside the optical radius r_{25}. Moreover, the narrow component, which represent

the CNM, tend to dominate inside r_{25}. We have also derived radial super profiles of some of the THINGS galaxies and we have found a radial decline in both the narrow and broad components velocity dispersions for most of the THINGS galaxies.

In order to check whether there is any correlation between the shapes of the profiles and the star formation activity of a galaxy, we have used the star formation rate surface density Σ_{SFR} maps derived by Leroy et al. (2008) to locate different star formation regions within a galaxy and to classify them as low, medium and high SFR regions according to their Σ_{SFR} values. We have analyzed the shapes of the super profiles of the clean sample in these three regions and we found some correspondence between profile shapes and star formation. We have found similar results as found from the analysis of the shapes of the super profiles inside and outside r_{25}. The super profiles in the high SFR regions tend to be broader and more asymmetric than those in the medium and low SFR regions. Moreover, the narrow component tend to dominate in the high SFR regions.

7.2 Future work

This thesis has provided valuable information regarding the phase structure of the ISM and its relation to galaxy properties. However, many interesting studies can still be done regarding the properties of the CNM and WNM that we have identified in our sample galaxies. One such study may involve investigating whether the CNM is associated with molecular gas in these galaxies. It will also be interesting to check whether the CNM and WNM phases of these galaxies are in pressure equilibrium. Another interesting study that can be done is to use the narrow component velocity dispersions that we have derived in the outskirts of galaxies to predict the location favorable for star formation in a galaxy. The dominant mechanisms that can explain the observed width of the super profiles are also worth investigating. This will shed light on our knowledge of the interstellar turbulence.

Bibliography

[1] Bakes, E. L. O.; Tielens, A. G. G. M. 1994, 427, 822

[2] Bajaja, E.; Huchtmeier, W. K.; Klein, U. 1994, A&A, 285, 385

[3] Baldwin, J. E., Lynden-Bell, D., Sancisi,R. 1980, MNRAS, 193, 313

[4] Bigiel, F.; Leroy, A.; Walter, F.; Brinks, E.; de Blok, W. J. G.; Madore, B.; Thornley, M. D. 2008, AJ, 136, 2846

[5] Braun, R. 1997, ApJ, 484, 637

[6] Braun, R.; Walterbos, R. A. M.; Kennicutt, R. C.; Tacconi, L. J. 1994, ApJ, 420, 558

[7] Calzetti, D., et al. 2007, ApJ, 666, 870

[8] Chemin, L.; Cayatte, V.; Balkowski, C.; Marcelin, M.; Amram, P.; van Driel, W.; Flores, H. 2003, A&A, 405, 89

[9] Clark, B. G. 1965, ApJ, 142, 1398

[10] Cox, D. P. 2005, Annu. Rev. Astron. Astrophys. 43, 337-385

[11] Cox, D.P; Smith, B.W. 1974, ApJ, 1989, 105

[12] de Blok, W. J. G.; Walter, F. 2006, AJ, 131, 363

[13] de Blok, W. J. G.; Walter, F.; Brinks, E.; Trachternach, C.; Oh, S.-H.; Kennicutt, R. C. 2008, AJ, 136, 2648

[14] Davies, R. D.; Davidson, G. P.; Johnson, S. C. 1980, MNRAS, 191, 253

[15] Dickey, J. M.; Lockman, F. J. 1990, ARA&A, 28, 215

[16] Dickey, J. M.; Brinks, E. 1993, ApJ, 405, 153

[17] Draine, B. T. 1978, ApJ, 36, 595

[18] Elmegreen, B. G., Scalo, J. 2004, in *Interstellar Turbulence I: Observations and Processes*. Annu Rev Astron Astrophys 42, 211273

[19] Field, G. B. 1959, ApJ, 129, 536

[20] Field, G. B.; Goldsmith, D. W.; Habing, H. J. 1969, ApJ, 155L, 149

[21] Goss, W. M.; Radhakrishnan, V.; Brooks, J. W.; Murray, J. D. 1972, ApJS, 24, 123

[22] Goulding, A. D.; Alexander, D. M. 2009, MNRAS, 398, 1165

[23] Goulding, A. D.; Alexander, D. M.; Lehmer, B. D.; Mullaney, J. R. 2010, MNRAS, 406, 597

[24] Greggio, L.; Tosi, M.; Clampin, M.; de Marchi, G.; Leitherer, C.; Nota, A.; Sirianni, M., 1998, ApJ, 504, 725

[25] Haynes, M. P.; Giovanelli, R.; Roberts, M. S. 1979, ApJ, 229, 83

[26] Haynes, M. P., Hogg, D. E., Maddalena, R. J., Roberts, M. S., van Zee, L. 1998, AJ, 115, 62

[27] Hunter, D. A., Wilcots, E. M., van Woerden, H., Gallagher, J. S., Kohle, S. 1998, ApJL, 495, 47

[28] Hunter, D. A.; Elmegreen, B. G.; van Woerden, H. 2001, ApJ, 556, 773

[29] Jenkins, E. B. 1978a, ApJ, 219, 845

[30] Jenkins, E. B. 1978b, ApJ, 220, 107

[31] Kennicutt, R. C. 1989, ApJ, 344, 685

[32] Kennicutt, R. C. 1998a, ApJ, 498, 541

[33] Kim, W. -T., Ostriker, E. C., Stone, J. M. 2003, ApJ, 599, 1157

[34] Larson, R. B. 2003, in *Reports on Progress in Physics*, 66, 1651

[35] Leroy, A. K.; Walter, F.; Brinks, E.; Bigiel, F.; de Blok, W. J. G.; Madore, B.; Thornley, M. D. 2008, AJ, 136, 2782

[36] Leroy, A. K.; Walter, F.; Bigiel, F.; Usero, A.; Weiss, A.; Brinks, E.; de Blok, W. J. G.; Kennicutt, R. C.; Schuster, K. -F.; Kramer, C.; Wiesemeyer, H. W.; Roussel, H. 2009, 137, 4670

[37] Mac Low M.-M. & Klessen R.S. 2004, RvMP, 76, 125

[38] Martin, C. L., & Kennicutt, R.C., Jr. 2001, ApJ, 555, 301

[39] Mathis, J. S. 1990, ARA&A, 28, 37

[40] McKee, C. F; Ostriker, J. P 1977, ApJ, 218, 148

[41] Melioli, C.; de Gouveia Dal Pino, E. M. 2004, A&A, 424, 817

[42] Munch, G.; Zirin, H. 1961, ApJ, 133, 11

[43] Mühle, S.; Klein, U.; Wilcots, E. M.; Hüttemeister, S. 2005, AJ, 130, 524

[44] Norman, C. A.; Ferrara, A., 1996, ApJ, 467, 280

[45] Palla, F., Zinnecker, H. 1999, in *Physics of star formation in galaxies*

[46] Petric, A. O.; Rupen, M. P. 2007, AJ, 134, 1952

[47] Purcell, E., M., and Field , G.B. 1956, 124, 542

[48] Radhakrishnan, V.; Brooks, J. W.; Goss, W. M.; Murray, J. D.; Schwarz, U. J 1972, 24, 1

[49] Radhakrishnan, V.; Murray, J. D.; Lockhart, Peggy; Whittle, R. P. J. 1972, ApJS, 24, 15

[50] Radhakrishnan, V.; Goss, W. M.; Murray, J. D.; Brooks, J. W. 1972, ApJS, 24, 49

[51] Radhakrishnan, V.; Goss, W. M. 1972, 24, 161

[52] Rogerson, J. B.; Spitzer, L.; Drake, J. F.; Dressler, K.; Jenkins, E. B.; Morton, D. C.; York, D. G 1973, ApJ, 181, 97

[53] Ryan Joung, M. K. & Mac Low M., -M. 2006, ApJ, 653, 1266

[54] Sandage, A., Tammann, G.A. 1981, in *The Revised Shapley-Ames Catalog*, (Washington: Carnegie Institution)

[55] Salim, S., et al. 2007, ApJS, 173, 267

[56] Safronov, V.S. 1960, Ann. d' Aptrophys., 23, 979

[57] Savage, B. D., Mathis, J. S. 1979, Annu. Rev. Astron. Astrophys., 17, 73

[58] Schaye, J. 2004, ApJ, 609, 667

[59] Schmidt, M. 1959, ApJ, 129, 243

[60] Sellwood, J. A.; Balbus, S. A. 1999, ApJ, 511, 660

[61] Silk, J. ; Werner, M. W. 1969 ApJ, 158, 185

[62] Spitzer, L. 1956, ApJ, 124, 20

[63] Spitzer, L. 1978, in *Physical Processes in the Interstellar Medium*, (New York: John Wiley & Sons)

[64] Spitzer, L. 1982, ApJ, 262, 315

[65] Stil, J. M.; Israel, F. P. 1998, A&A, 337, 64

[66] Swaters, R. A.; Sancisi, R.; van der Hulst, J. M. 1997, ApJ, 491, 140

[67] Tamburro, D.; Rix, H.-W.; Leroy, A. K.; Mac Low, M.-M.; Walter, F.; Kennicutt, R. C.; Brinks, E.; de Blok, W. J. G. 2009, AJ, 137, 4424

[68] Tielens, A. G. M. 2005, in *The Physics and Chemistry of the Interstellat Medium*, (Cambridge, UK: Cambridge University Press)

[69] Toomre, A. 1964, ApJ, 139, 1217

[70] Trachternach C., de Blok, W. J. G., Walter, F., Brinks, E., Kennicutt, R. C. 2008, AJ, 136, 2720

[71] Trumpler, R. 1930, PASP, 42, 214

[72] van der Hulst, J. M.; Skillman, E. D.; Smith, T. R.; Bothun, G. D.; McGaugh, S. S.; de Blok, W. J. G. 1993, AJ, 106, 548

[73] van Woerden, H., Bosma, A., & Mebold, U. 1975, in *La Dynamique des Galaxies Spirales*, ed. L. Weliachew (Paris: Ed. du Cent. Natl. de la Rech. Sci.)

[74] Vallenari, A., Bomans, D.J. 1996, A&A, 313, 713

[75] Walter, F.; Brinks, E.; de Blok, W. J. G.; Bigiel, F.; Kennicutt, R. C.; Thornley, M. D.; Leroy, A. 2008, AJ, 136, 2563

[76] Walter, F.; Weiss, A.; Martin, C.; Scoville, N. 2002, AJ, 123, 225

[77] Walterbos, R. A. M.; Braun, R. 1996, ASPC, 106, 1

[78] Watson, W. D. 1972, ApJ, 176, 103

[79] Weingartner, J. C.; Draine, B. T. 2001, ApJ, 134, 263

[80] Wolfire, M. G.; McKee, C. F.; Hollembach, D., Tielens, A. G. G. M. 2003, ApJ, 587, 278

[81] York, D. G. 1977, ApJ, 213, 43

[82] Young, L. M.; Lo, K. Y. 1997, ApJ, 490, 710

[83] Young, L. M.; Lo, K. Y. 1997, ApJ, 476, 127

[84] Young, L. M.; Lo, K. Y. 1996, ApJ, 462, 203

[85] Young, L. M et al. 2003, ApJ, 592, 111

[86] York, D. G. 1977, ApJ, 213, 43